

NUCLEATION, TRANSFORMATION, AND IMPACTS OF ATMOSPHERIC
AEROSOLS

A Dissertation

by

MISTI ELIZABETH LEVY ZAMORA

Submitted to the Office of Graduate and Professional Studies of
Texas A&M University
in partial fulfillment of the requirements for the degree of

DOCTOR OF PHILOSOPHY

Chair of Committee,	Renyi Zhang
Committee Members,	Don Collins
	Qi Ying
	Guoyao Wu
	Sasha Madronich
Head of Department,	Ping Yang

December 2015

Major Subject: Atmospheric Sciences

Copyright 2015 Misti Elizabeth Levy Zamora

ABSTRACT

Atmospheric aerosols are a key contributor to pollution, adversely affect human health, and can alter global climate. Several questions concerning atmospheric aerosols persist, including: ‘Which atmospheric species are integral for aerosol formation in the atmosphere?’, ‘What happens to aerosols after emission into or formation in the atmosphere?’, ‘Does maternal exposure to aerosols during pregnancy fundamentally alter her offspring?’, and ‘Can we utilize gas phase chemistry models to further our understanding of atmospheric aerosols?’. A series of chamber, observational, and computational studies have been conducted to investigate these scientific questions.

Globally, new particle formation (NPF) events account for more than 50% of the aerosols in the troposphere, but the chemical species and mechanisms responsible for NPF have yet to be fully understood. To explicate the role of organic compounds in NPF, laboratory experiments have been conducted to investigate aerosol nucleation and growth from the photochemical oxidation of biogenic and anthropogenic volatile organic compounds (VOCs). Here we show that the NPF is dependent on the VOC species and that the global pattern of NPF is likely governed by the available VOCs.

A suite of instruments was deployed in Beijing to measure a comprehensive set of aerosol properties in order to elucidate the aerosol formation mechanisms and the evolution of aerosol properties. NPF consistently occurred on clean, windy days, and the high aerosol mass observed during haze events is attributable to the continuous growth from the nucleation-mode particles over multiple days to produce a high concentration

of larger particles. Our results reveal that the severe haze in Beijing is likely due to the concentrated aerosol precursor gases and the large-scale meteorological conditions.

Model simulations indicate that the persistent high concentrations of NO₂ in Beijing and the frequent periods of high aerosol loading leads to elevated HONO levels and sustained oxidizing capacity.

To determine the mechanism through which aerosols influence human health, a series of animal exposure studies have been conducted to investigate the transgenerational effects. In each experiment, Sprague-Dawley rats were continuously exposed between days 0 and 18 of gestation to controlled conditions to represent either clean ($\sim 5 \mu\text{g m}^{-3}$) or polluted ($\sim 150 \mu\text{g m}^{-3}$) environments. The gestation length, litter size, birth weight, and sex ratio were assessed throughout the animal exposure studies. The preliminary results indicate the development of several organs and the birth weight may be influenced by prenatal exposure to pollutants and the degree of response may also be sex dependent.

DEDICATION

I dedicate this dissertation to my boys. First and foremost to my husband, whom I love dearly. Secondly, to my brothers, who I hope will one day follow in my foot steps and pursue higher education.

ACKNOWLEDGEMENTS

I would like to thank my advisor, Dr. Renyi Zhang, for his guidance, support, and the many wonderful opportunities that have been presented to me during my graduate studies. His dedication and hard work were exemplary, and I gained valuable knowledge and experience as a member of his research group.

I would like to acknowledge my other committee members, Drs. Donald Collins, Qi Ying, Guoyao Wu, and Sasha Madronich, for their support and time. I especially appreciate the time Dr. Madronich spent teaching me how to use the Master Mechanism and for the insights he provided about my Beijing data. Also, I would like to thank Dr. Collins for lending me his instrument, without which I would not have been able to finish my project.

I want to recognize Jacob Brown, a graduate student in the animal science department. We spent many hours together trying to maintain our project, and I know he spent many more days and holidays in the lab keeping our rats alive.

I thank my officemates, past and present, who have made work both beneficial and enjoyable. Special thanks to Mario and Jeremiah who were always willing to help me out be it by finding a part in the lab, moving heavy items, or teaching me something. Also, my thanks go to Song Guo who collected some of the data and assisted in writing several manuscripts.

I would like to thank my friends and family for all of the prayers, support, love, and hugs. Specifically, I want to thank Katelyn and April who kept me grounded and

wouldn't let me escape to my hermit cave. My deepest thanks go to my husband, Ryan, who offered daily support and love as a husband, friend, classmate, and colleague, which made my journey possible. Here's to the next step in our adventure. Finally, thanks to my mother and father for their encouragement and love.

NOMENCLATURE

AERONET	Aerosol Robotic Network
AMS	Aerosol Mass Spectrometer
AOD	Aerosol Optical Depth
APM	Aerosol Particle Mass Analyzer
AQI	Air Quality Index
CCN	Cloud Condensation Nuclei
Coarse Particles	Particulate Matter smaller than 10.0 μm in diameter
CPC	Condensation Particle Counter
DMA	Differential Mobility Analyzer
EPA	Environmental Protection Agency
Fine Particles	Particulate Matter smaller than 2.5 μm in diameter
Gecko-A Model	Generator Of Explicit Chemistry And Kinetics Of Organics In The Atmosphere
HGF	Hygroscopic Growth Factors
HO _x	OH + HO ₂
HOA	Hydrocarbon-Like Organic Aerosol
HR-TOF-AMS	High-Resolution Time-Of-Flight Aerosol Mass Spectrometer
HTDMA	Hygroscopic Tandem Differential Mobility Analyzer
HYSPLIT	Hybrid Single-Particle Lagrangian Integrated Trajectory Model
IE	Ionization Efficiency

LPM	Liters Per Minute
LV-OOA	Low Volatility Oxygenated Organic Aerosol
MEIC	Multi-resolution Emission Inventory for China
MM	Master Mechanism
NAAQS	National Ambient Air Quality Standards
NCAR	The U.S. National Center For Atmospheric Research
NDMA	Nano Differential Mobility Analyzer
NOAA	National Oceanic And Atmospheric Administration
NO _x	NO + NO ₂
NPF	New Particle Formation
OA	Organic Aerosols
O _x	O ₃ + NO ₂ , Odd-Oxygen
O/C	Oxygen/Carbon Ratio
PBL	Planetary Boundary Layer
PKU	Peking University
PM	Particulate Matter
PM ₁	Particulate Matter smaller than 1.0 μm in diameter
PM ₁₀	Particulate Matter smaller than 10.0 μm in diameter
PM _{2.5}	Particulate Matter smaller than 2.5 μm in diameter
POA	Primary Organic Aerosol
PPB	Parts Per Billion
PPM	Parts Per Million

PPT	Parts Per Trillion
PSL	Polystyrene Latex Spheres
PSM	Particle Size Magnifier
PSS	Photostationary State
PTR-MS	Proton Transfer Reaction – Mass Spectrometer
SIM	Selected Ion Monitoring
SMPS	Scanning Mobility Particle Sizer
SOA	Secondary Organic Aerosol
SV-OOA	Semi-Volatile Oxygenated Organic Aerosol
TD-ID-CIMS	Thermal Desorption – Ion Drift – Chemical Ionization Mass Spectrometer
TEOM	Tapered Element Oscillating Microbalance
TSP	Total Suspended Particles
TUV	Tropospheric Ultraviolet Visible Model
Ultrafine Particles	Particulate Matter smaller than 1.0 μm in diameter
VOC	Volatile Organic Compound
WHO	The World Health Organization

TABLE OF CONTENTS

	Page
ABSTRACT	ii
DEDICATION.....	iv
ACKNOWLEDGEMENTS.....	v
NOMENCLATURE	vii
TABLE OF CONTENTS	x
LIST OF FIGURES.....	xii
LIST OF TABLES.....	xviii
CHAPTER I INTRODUCTION AND LITERATURE REVIEW.....	1
i) Climate Effects.....	5
ii) Alteration of Global Weather Patterns.....	6
iii) Visibility	8
iv) Air Quality Standards.....	9
CHAPTER II WHICH ATMOSPHERIC SPECIES ARE INTEGRAL FOR AEROSOL FORMATION IN THE ATMOSPHERE? INVESTIGATION INTO THE ROLE OF ORGANICS IN ATMOSPHERIC NEW PARTICLE FORMATION.....	14
i) Introduction.....	14
ii) Methodology.....	21
iii) Results and Discussion	27
CHAPTER III WHAT HAPPENS TO AEROSOLS AFTER EMISSION INTO OR FORMATION IN THE ATMOSPHERE? FIELD MEASUREMENTS IN BEIJING OF PARTICULATE MATTER PROPERTIES.....	37
i) Introduction.....	37
ii) Methodology.....	40
iii) Results and Discussion	46
a) Beijing 2013	46
b) Beijing 2015	62
c) Comparisons of Beijing Aerosol Properties from Fall 2013 and Winter 2015 ...	72

CHAPTER IV DOES MATERNAL EXPOSURE DURING PREGNANCY FUNDAMENTALLY ALTER HER OFFSPRING? ANIMAL PROXY STUDIES OF EXPOSURE TO POLLUTANTS UNDER ATMOSPHERICALLY RELEVANT CONDITIONS.....	77
i) Introduction.....	77
ii) Developing the Animal Exposure System.....	84
a) The Chamber.....	84
b) Producing and Maintaining High Aerosol Loading.....	88
c) Methodology for Animal Experiments.....	91
iii) Results and Discussion.....	93
CHAPTER V CAN WE UTILIZE GAS PHASE CHEMISTRY MODELS TO FURTHER OUR UNDERSTANDING OF ATMOSPHERIC AEROSOLS? ELUCIDATION OF THE GAS PHASE CHEMISTRY IN BEIJING, CHINA.....	94
i) Introduction.....	94
ii) The NCAR Master Mechanism Model.....	96
iii) Adaptation of the Model to Beijing, China.....	98
a) Emission and Meteorological Profiles.....	98
b) Emission Inventory.....	101
c) The Necessity of Nitrous Acid Chemistry in Beijing.....	105
iv) Results and Discussion.....	114
a) Sensitivity Study of the Relationship between NO _x and VOC.....	114
b) Model Results.....	118
CHAPTER VI CONCLUDING REMARKS AND FUTURE WORK.....	121
i) The Role of Volatile Organic Compounds in New Particle Formation.....	121
ii) Beijing Haze Formation.....	122
iii) Development of an Animal Exposure System.....	125
iv) Gas Phase Chemistry Model of Beijing Radical Chemistry.....	126
REFERENCES.....	128

LIST OF FIGURES

	Page
Figure 1. An example of light scattering caused by aerosols resulting in a dimming effect. These photographs were taken on the campus of Peking University in Beijing at the same time of day. The photo on the left was taken on a clean day, and the photo on the right was taken on a polluted day.....	6
Figure 2. Historic trends in A) SO ₂ and NO _x concentrations, the number of vehicles, and the gross domestic product in China, and B) the visibility in Beijing, Xi'an, Nanjing, and Guangzhou.	9
Figure 3. A) The iconic ‘banana curve’ that indicates new particle formation. B) The subsequent changes in the total number (black dots) and mass concentration (red dots) during and after new particle formation.	18
Figure 4. Schematic of instruments operated in new particle formation experiments. ...	22
Figure 5. The A) concentration of isoprene (red) and α -pinene (blue) measured by the PTR-MS and B) size distributions of particles with a diameter between 1.5 and 40 nm.....	24
Figure 6. An example of the two methodologies utilized for collecting new particle formation data: the condensation particle counter, which determine the total concentration (shown in green dots) and scanning mobility particle sizing, which determines the particle size distribution (hours 2-9). The decrease in concentration between hours 2 and 6 is due to particles being collected by the TD-ID-CIMS to determine the chemical composition.....	25
Figure 7. Background concentration of particles and VOCs in the chamber as a function of time.....	26
Figure 8. The concentration of particles formed from the photochemical oxidation of A) α -pinene with an initial concentration of 5 (red), 10 (black), 20 (blue), 50 (green), and 100 ppb (pink); B) m-xylene with an initial concentration of 20 (red), 50 (black), 100 (blue), and 200 ppb (green); and C) toluene with an initial concentration of 100 (red), 200 (black), and 400 ppb (blue) as a function of time. D) The new particle formation rates (J , $s^{-1} cm^{-3}$) for α -pinene (blue circles), m-xylene (black triangles), and toluene (red squares) at various initial concentrations	27
Figure 9. A comparison of the number concentration (cm^{-3}) produced from the photochemical oxidation of α -pinene (red), m-xylene (black), and toluene (blue) at various initial concentrations.....	28

- Figure 10. A-C) The protonated monomers of the oxidation products of α -pinene, m-xylene, and toluene shown in the mass-to-charge ratio (m/z) determined by TD-ID-CIMS analysis of the particle composition in positive ion mode. D-F) The protonated dimers of the corresponding oxidation products..... 30
- Figure 11. The concentration of particles (cm^{-3}) formed from the photochemical oxidation of A) 20 ppb of α -pinene mixed with increasing concentration of isoprene, B) 200 ppb of m-xylene mixed with increasing concentration of isoprene, C) 400 ppb of toluene mixed with increasing concentration of isoprene, D) 50 ppb of α -pinene mixed with 50 ppb of m-xylene and toluene, and E) 200 ppb of m-xylene, 400 ppb of toluene, and their mixture. F) Comparison new particle formation rates ($\text{J}, \text{s}^{-1} \text{cm}^{-3}$) from the photooxidation of α -pinene (blue circles), m-xylene (black triangles), and toluene (red squares) with increasing isoprene concentrations..... 33
- Figure 12. A) The particle size distributions of the new particle formation from α -pinene (black), m-xylene (green), toluene (blue), and isoprene (red) with an initial concentration of 100 ppb, and B) the initial (black) and succeeding particle size distribution measured hourly for seven hours (red, orange, yellow, green, blue, indigo, and violet) of α -pinene with an initial concentration of 50 ppb..... 35
- Figure 13. Temporal evolutions of A) $\text{PM}_{2.5}$ mass concentration, B) number size distribution, C) mean diameter, and D) total number concentration during the period of 25 September to 13 November 2013. The colors in A, C, and D represents the air mass originating from the south (black), northwest (blue and red), and northeast (yellow). Reprinted with permission of the National Academy of Sciences from Guo, et al., (2014). Elucidating severe urban haze formation in China. Proceedings of the National Academy of Sciences, 111(49), 17373-17378. Copyright 2014 National Academy of Sciences, USA..... 47
- Figure 14. A) Temporal evolutions of particle number size distribution and mean diameter (white dashed curve) and B) $\text{PM}_{2.5}$ mass concentration (black solid line), mean diameter (purple dashed line), and PM_1 (particulate matter smaller than $1.0 \mu\text{m}$) chemical composition between 25-28 September 2013. Reprinted with permission of the National Academy of Sciences from Guo, et al., (2014). Elucidating severe urban haze formation in China. Proceedings of the National Academy of Sciences, 111(49), 17373-17378. Copyright 2014 National Academy of Sciences, USA..... 48
- Figure 15. A-C) Chemical composition for 80, 100, and 240 nm particles from the corresponding particle mean diameter during the clean ($12 \mu\text{g m}^{-3}$), transition ($167 \mu\text{g m}^{-3}$), and polluted periods ($288 \mu\text{g m}^{-3}$), respectively.

Reprinted with permission of the National Academy of Sciences from Guo, et al., (2014). Elucidating severe urban haze formation in China. Proceedings of the National Academy of Sciences, 111(49), 17373-17378. Copyright 2014 National Academy of Sciences, USA.	50
Figure 16. The weighted average effective density of 81 (blue), 97 (green), 151 (black), and 240 nm (red) particles during the 2013 Beijing field campaign. .	51
Figure 17. The hygroscopic distributions of A) 46, B) 81, C) 97, and D) 151 nm particles determined by a HTDMA. The intensity of the colors correlate to the concentration of particles: the more red, the higher the relative concentration. E) A comparison of the weighted hygroscopic growth factor (black) and kappa (red) between 25 and 29 September.	53
Figure 18. A) Map demonstrating the location of the sampling site and back-trajectories using the NOAA–HYSPLIT model to illustrate the frequency of synoptic flow patterns observed during the field campaign. B) The predominant wind direction throughout a haze event. Reprinted with permission of the National Academy of Sciences from Guo, et al., (2014). Elucidating severe urban haze formation in China. Proceedings of the National Academy of Sciences, 111(49), 17373-17378. Copyright 2014 National Academy of Sciences, USA.	55
Figure 19. Concentrations (ppb) of A) aromatic VOCs, B) biogenic VOCs, and C) SO ₂ measured between 16 October and 31 November (i.e. the period when these instruments were online) and of D) ozone, E) biogenic VOCs, and F) PM _{2.5} mass concentration (µg m ⁻³) measured between 25 September and 10 November 2013.	57
Figure 20. A) The mass concentrations of PM _{2.5} (blue), secondary organic aerosols (red), and primary organic aerosols (green), and the aerosols optical depth (black). B-D) Scatterplots of odd-oxygen (O ₃ + NO ₂ , O _x) and secondary organic aerosols during the clean, transition, and polluted phases.	59
Figure 21. Comparisons of the winter PM _{2.5} concentration between 2010 and 2015 in Beijing, China measured at the U.S. Embassy [<i>U.S. Department of State</i> , 2013].	62
Figure 22. The PM _{2.5} mass concentration and the corresponding air quality index between 21 January and 5 February 2015.	63
Figure 23. Temporal evolutions of the A) number size distribution, B) PM _{2.5} mass concentration, chemical composition, C) total number concentration, and D) mean diameter between 21 and 27 January 2015.	65

Figure 24. A) The mass concentration ($\mu\text{g m}^{-3}$) and B) mass fraction from 12 p.m. on 23 January to 12 p.m. 24 January.....	66
Figure 25. Comparison of the chemical composition between the clean and polluted periods.....	67
Figure 26. A) The hygroscopicity determined on the basis of chemical composition (i.e. kappa) of the aerosols. B) Temporal evolutions of the effective density of particles with a diameter of 81 (blue), 97 (green), 151 (red), 240 nm (orange), and the weighted average of the four particle sizes between 21 and 29 January 2015.	68
Figure 27. A) The diurnal cycle of the effective density (g cm^{-3}) of the four particle sizes from the full observational period. B) The effective density (g cm^{-3}) diurnal cycle of the 81 (blue circles) and 240 (black squares) nm particles during the clean (dashed, lighter colors) and polluted periods (solid, darker colors).....	70
Figure 28. Typical synoptic conditions observed during A) polluted and B) clean days. The forward trajectories and mixing depths were determined by the HYSPLIT model.	72
Figure 29. A comparison of the A) mass concentration, B) total number concentration, C) average diameter, and D) hygroscopicity between the fall 2013 and winter 2015 field campaigns.	73
Figure 30. A comparison of the chemical composition during the clean and polluted period from both campaigns.	74
Figure 31. A comparison of the mixing layer depth (m) determined by the HYSPLIT model and the mass concentration ($\mu\text{g m}^{-3}$) in A) Fall 2013 and B) Winter 2015.....	75
Figure 32. Schematic of the animal exposure chamber. The top panel depicts the underside of the lid, the middle panel is the bottom of the chamber, and the bottom panel illustrates the airflow within the chamber. The u-shaped inflow lines, attached to the underside of the lid, have evenly distributed holes over each of the compartments to produce even flow and exposure in each individual space. The outflow line, attached to the bottom, also has evenly distributed holes under each of the compartment to facilitate uniform removal of the chamber air.	85
Figure 33. Diagram of the animal exposure chambers and instruments. Pure ambient air is pumped into the clean chamber, and doped ambient air is pumped into the polluted chamber. The polluted and clean systems are independent of	

each other. The system flow rate is 55 LPM or 67 chamber turnovers per hour. The polluted chamber aerosols are sampled at a rate of 1 LPM by the DMA and CPC.....	86
Figure 34. The chambers constructed for the animal exposure experiments.	87
Figure 35. The number concentration distributions and the calculated total mass ($\mu\text{g m}^{-3}$) of ammonium sulfate measured by a Differential Mobility Analyzer A-B) in the chamber and C-D) in the ambient room air. The scans were measured on various days throughout the experiment. The red points indicate the times when daily animal care was performed, and the blue dots indicate the time when machine maintenance or calibration was typically conducted.	89
Figure 36. An overview of the NCAR Master Mechanism box model.....	97
Figure 37. A-E) The temperature, H ₂ O (i.e. relative humidity), wind speed (used to estimate horizontal dilution), PBL height, and cloud factor profiles for the three days modeled. F-G). Concentration profiles of biogenic (i.e. isoprene) and anthropogenic (i.e. NO) sources. H) Seasonal emission profile for NO _x . 99	99
Figure 38. The model-generated peak values determined as a function of NO _x and VOC emissions for 27 September, where NO _x = 1 and VOCs = 1 is the concentrations suggested values by the <i>MEIC</i> [2015] (3.34×10^{17} molecules day ⁻¹ cm ⁻²) and <i>Wang et al.</i> [2014c] (5.38×10^{17} molecules day ⁻¹ cm ⁻²) emissions inventories, respectively, The plus signs indicate regions where the model-generated peak values reasonably matched the measured values. 105	105
Figure 39. A) Source optimization of the various HONO sources in the MM Model. Days 0 - 2 correspond to 26 - 28 September 2013, respectively. The ‘base’ case utilized only the standard HONO chemistry provided in the model (1 - 5). The ‘chemistry’ case included only Reactions 1 - 8. The ‘aerosol’ run utilized the additional ‘chemistry’ reactions and HONO created by reactions on the surface of aerosols (1 - 8, 10). The ‘HNO ₃ photolysis’ case included the additional ‘chemistry’ reactions and HONO produced through the photolysis of HNO ₃ on surfaces (1 - 9). B) The total concentration produced through the three pathways. C) The simulation incorporating all reactions is compared to HONO measurements that were obtained in 2006 [<i>Yang et al.</i> , 2014] and 2007 [<i>Spataro et al.</i> , 2013] in the Beijing province.	111
Figure 40. The temporal variations of various gas phase species when the expanded HONO chemistry is included (shown in blue) or excluded (shown in red) determined by the NCAR Master mechanism. Days 0-2 correspond to 26-28 September 2013, respectively.	113

Figure 41. The model-generated peak values of ozone (ppb) determined as a function of NO_x and VOC emissions for 27 September. The circle indicates the base ratio of VOC and NO_x , and the dashed and solid lines indicate a 50% reduction of VOC and NO_x , respectively. 115

Figure 42. The temporal variations of various gas phase species (shown in red) determined by the NCAR Master mechanism compared to field measurements (black, purple, or aqua). A solid black line indicates that the measurements were collected at the PKU site. A purple line indicates that the values were reported from by previous publications [*Lu et al.*, 2013; *Yang et al.*, 2014]. A dashed line indicates that the measurements were not obtained during the model period. The aqua line is the peroxy radical concentration determined by the deviation from the photostationary state calculation. In the VOC panel, the darker lines indicate toluene and the lighter shades indicate benzene. Days 0 - 2 correspond to 26 - 28 September 2013, respectively. 119

LIST OF TABLES

	Page
Table 1. Air pollution standards established by the United States, China, and The World Health Organization. The concentrations have been listed in $\mu\text{g m}^{-3}$ unless otherwise indicated.	11
Table 2. Comparison of the air quality index for $\text{PM}_{2.5}$ in the United States, China, and Europe.	13
Table 3. Properties of the four VOCs utilized in the new particle formation experiments.	21
Table 4. Emission inventory used in the Master Mechanism. The black carbon, carbon monoxide, nitrogen oxides, organic carbon, PM_{10} , $\text{PM}_{2.5}$, and sulfur dioxide data were acquired through the MEIC website [MEIC, 2015], and the speciated VOC data were obtained from Wang <i>et al.</i> [2014c]. The second column indicates the naming system used by the Master Mechanism box model.	102
Table 5. Detailed emission inventory of the non-methane hydrocarbons from Wang <i>et al.</i> [2014c]. The second column indicates the naming system used by the Master Mechanism. Similar compounds were aggregated (shown in red) to reduce the number of species.	103
Table 6. Comparison of the VOC/ NO_x ratios	116

CHAPTER I

INTRODUCTION AND LITERATURE REVIEW

Atmospheric aerosols, solid particles or liquid droplets suspended in a gas, have a broad range of impacts on the environment, including modulating photochemistry [Horvath, 1993; Haywood and Boucher, 2000; Li *et al.*, 2005; Lohmann and Feichter, 2005], enhancing multiphase chemistry [Li *et al.*, 2005], modifying cloud formation [Twomey, 1977; Fan *et al.*, 2007; 2008], altering large scale meteorological systems [Albrecht, 1989; Zhang *et al.*, 2007; Levin and Cotton, 2009; Wang *et al.*, 2014a, b], and degrading local, regional, and global air quality [Jacobson, 2001; Ramanathan *et al.*, 2001]. Measurements of atmospheric aerosols largely focus on quantifying the particle number, size, and composition because these properties most influence human health, climate, and cloud microphysics [Zhang *et al.*, 2015b]. Aerosols vary significantly depending on the location of study due to the numerous potential sources, and the overall impact of aerosols is dependent on the size, concentration, and chemical composition of the particles within an air mass [Jimenez *et al.*, 2009; Zhang *et al.*, 2015b]. Once emitted into the atmosphere, aerosols undergo chemical and physical transformations and are subjected to regional and long-range.

Atmospheric pollution is comprised of a complex combination of primary and secondary aerosols, also known as particulate matter (PM), and gaseous pollutants, such as ozone (O₃), NO₂, benzene, toluene, ethylbenzene, xylenes, and SO₂. Gas phase pollutants also have significant impacts on air quality and the health of humans and the

ecosystem [WHO, 2005; He *et al.*, 2014]. Aerosols are broadly classified by three systems: 1) primary (e.g. directly emitted into the atmosphere) or secondary (e.g. formed in situ through gas-to-particle conversion processes); 2) natural (e.g. forest fires, volcanoes, and biogenic emissions) or anthropogenic (e.g. vehicle exhaust, industrial sources, and biomass burning); and 3) fine (particles with a diameter less than 2.5 microns) or coarse (particles with a diameter less than 10 microns). Fine aerosols are dominantly produced by fossil fuel combustion and gas-to-particle conversion and are mainly composed of sulfates, nitrates, ammonium, trace metals, and organic compounds [Zhang *et al.*, 2015b]. The atmospheric lifetime of fine aerosols is typically a few days to weeks [Seinfeld and Pandis, 2006]; therefore, fine aerosols can be transported over several thousand kilometers [Zhang *et al.*, 2015b]. Fine particles are sometime further decomposed into ultra fine particles (diameter less than 1.0 micron) due to the notable health implication of these small particles. Coarse aerosols are largely attributable to road dust, soils, pollen, construction, demolition, industrial fugitive emissions, and tire or brake wear. The lifetime of coarse mode particles is on the order of hours to days due to gravitational settling, so the dispersion is limited to several hundred kilometers from the source region [Seinfeld and Pandis, 2006].

Globally, air pollution is increasing in severity and is affecting more people than ever before. For the first time in history, more people live in urban centers than in rural areas [UN, 2014]. Between 1950 and 2010, the percentage of the population living in urban regions increased by over 25%. In the past, the world's largest urban centers were in developed countries, which have stricter environmental regulations; however, today's

fastest growing cities are in found in developing country in Asia and Africa. Presently in North America, Latin America, and Europe, 82, 80, and 73% of the populations reside in urban areas; however, Asia is home to 53% of the world's urban population [UN, 2014]. China, in particular, is urbanizing at an astounding rate. In only 35 years, the country added more than 500 million people to its urban regions, a population rivaling the entire North American population. This economic development has resulted in the rapid expansion of large urban centers that did not exist 40 years ago. According to the Organisation for Economic Co-operation and Development, there are currently 15 megacities (i.e. cities with more than 10 million inhabitants) and 221 cities with more than 1 million residents in China [OECD, 2015]. For comparison there were 83 cities with populations exceeding one million globally in 1950. This global urbanization trend is expected to continue. By 2030, the world is projected to have 41 megacities, and the urban population in China alone is expected to surpass one billion [OECD, 2015]. By 2050, 70% of the population will be living in urban centers, an additional 2.5 billion people [UN, 2014].

Concurrently, unprecedentedly high aerosol concentrations are being measured in these urban areas in developing countries. The particulate matter (PM) concentrations in many regions of China, Africa, and India have considerably exceeded the level that is considered healthy ($10 \mu\text{g m}^{-3}$) by The World Health Organization (WHO) [WHO, 2005; Boman *et al.*, 2009; Kothai *et al.*, 2011; Guo *et al.*, 2014]. For example, the average $\text{PM}_{2.5}$ (particulate matter under $2.5 \mu\text{m}$ in diameter) in Beijing was $101.85 \mu\text{g m}^{-3}$ in 2013 [U.S. Department of State, 2013] and $103 \mu\text{g m}^{-3}$ during 2007–2009 at a site in

Delhi [*Chelani*, 2013]. For reference, the current U.S. Environmental Protection Agency (EPA) National Ambient Air Quality Standard (NAAQS) for PM_{2.5} is 35 µg m⁻³ for a 24 hr. period, and the annual average PM_{2.5} primary standard is 12 µg m⁻³ (see Table 1). Model projections based on a ‘business-as-usual’ emission scenario indicate that premature mortality due to air pollution to could double by 2050 [*Lelieveld et al.*, 2015].

Significant progress has been made towards understanding the chemistry of air pollution, but the mechanisms of several important processes remain unclear. Modeling of aerosol processes in climate models is presently flawed because of the lack of understanding of their formation mechanisms and the complicated physicochemical properties of aerosols. Particularly the formation mechanisms leading to urban haze episodes remain uncertain and controversial [*Zhang et al.*, 2012; *Guo et al.*, 2014; *He et al.*, 2014; *Sun et al.*, 2014], which hinders the development of effective mitigation policies. Furthermore, different urban centers (e.g. Mexico City, Houston, Los Angeles, or Beijing) and pristine environments (e.g. over the ocean, the amazon rain forest, etc.) exhibit distinct aerosol formation and growth mechanisms due to the diverse conditions [*Zhang et al.*, 2013; *Zhang et al.*, 2015b]. The global variation in the particle number, size, and composition of aerosols creates major challenges when evaluating the impacts on weather, air quality, and climate at both the regional and global scale; therefore, many field, laboratory, and modeling studies have been conducted in an effort to better understand the role of aerosols in the atmosphere [*Forster et al.*, 2007; *Cheng et al.*, 2009; *Aiken et al.*, 2010; *Bond et al.*, 2013; *IPCC*, 2013; *Levy et al.*, 2013; *Guo et al.*, 2014; *Levy et al.*, 2014a].

i) Climate Effects

Aerosol research remains an active field because aerosols produce the greatest source of uncertainty when projecting global climate change [Forster *et al.*, 2007; Zhang, 2010]. This uncertainty arises due to the wide range of effects aerosols can have on the atmosphere. Aerosols influence the climate directly through scattering and absorption solar radiation [Haywood and Boucher, 2000; Ramanathan *et al.*, 2001; Forster *et al.*, 2007] and indirectly by modifying cloud formation [Twomey, 1977; Albrecht, 1989; Fan *et al.*, 2007; Fan *et al.*, 2007; 2008]. Aerosols have a net cooling effect in the atmosphere since the dominant species, such as mineral dust, sulfates, nitrates, and organic carbon, reflect solar radiation; however, some species, such as black and brown carbon [Bond and Bergstrom, 2006; Moosmuller *et al.*, 2009; Bond and Bergstrom, 2013], absorb solar radiation and are major contributors to global warming [Jacobson, 2000, Jacobson, 2001; Bond *et al.*, 2013]. One particular challenge is the evaluation of direct radiative forcing when non-absorbing aerosols and light absorbing aerosols are co-located within the same air mass [Ramanathan and Carmichael, 2008; Ramana *et al.*, 2010]. Laboratory experiments [Khalizov *et al.*, 2009a; Xue *et al.*, 2009a, b; Qiu *et al.*, 2012; Khalizov *et al.*, 2013], modeling calculations [Jacobson, 2001], and field observations [Knox *et al.*, 2009; Moffet and Prather, 2009] have revealed that, when mixed with non-absorbing aerosol constituents, such as sulfate or organic aerosols, the absorption by black carbon is enhanced, and the mixture exerts a higher positive direct radiative forcing. The combination of these processes may prevent a significant portion of solar radiation from reaching the earth's surface, affecting thermal



Figure 1. An example of light scattering caused by aerosols resulting in a dimming effect. These photographs were taken on the campus of Peking University in Beijing at the same time of day. The photo on the left was taken on a clean day, and the photo on the right was taken on a polluted day.

structure and stability of the atmosphere. Highly concentrated aerosols may result in a dimming effect due to the decreased solar radiation reaching the surface as can be seen in Figure 1. *Ramanathan et al.* [2007] compared the aerosol optical depth (AOD) over 26 mega cities and found that urban centers have distinct contributions to the AOD, indicating that they may have different degrees of impact on global and regional climate. It was determined that the annual reduction of net solar radiation at the surface in most tropical megacities exceeds 20 W m^{-2} , which is equivalent to reducing solar irradiance at the top of the atmosphere by more than 10%.

ii) Alteration of Global Weather Patterns

Once emitted into the atmosphere, pollutants can alter cloud microphysics, weather systems, and air quality worldwide, but the extent of these impacts remains largely unknown. Some aerosols act efficiently as cloud condensation nuclei (CCN) and ice

nuclei, resulting in greater concentrations of smaller cloud particles than would be generated naturally [Lohmann and Feichter, 2005]. Some studies have shown that increasing the amount of aerosols may reduce precipitation efficiency; thus, increasing cloud lifetime and total reflectivity [Lohmann and Feichter, 2005]. Generally, the aerosol number concentration is higher in urban areas when compared to cleaner regions; therefore, urban clouds contain a greater concentration of smaller particles and exhibit longer cloud lifetime, suppressed drizzle, and enhanced deep cloud convection [Rosenfeld *et al.*, 2014]. As precipitation efficiency is inhibited, an enhancement of deep convection is possible, as clouds retain water longer [Seifert and Beheng, 2006]. In addition, the increased aerosol number concentration results in smaller ice particles that precipitate more slowly from the anvil region of deep convective clouds. This can create larger and longer-lasting cirrus clouds [Rosenfeld *et al.*, 2014]. These alterations of cloud properties have significant impacts on the hydrological cycle, producing droughts in regions accustomed to heavy precipitation and floods in otherwise naturally arid regions [Levin and Cotton, 2009]. For example, a marked increase in the cloud to ground lightning has been observed in regions of the highest AOD near the Pearl River Delta megacity area confirming the enhancement of the convective systems in the region [Wang *et al.*, 2011].

Recent studies indicate that Asian air pollution is strengthening storms in the Pacific Ocean, causing more precipitation, and enhancing the transport of heat from the tropics toward the North Pole [Wang *et al.*, 2014a, b]. Models have indicated that PM produced in China can be transported as high as nine km vertically into the atmosphere, where it is

introduced into the jet stream and subsequently globally dispersed [Wang *et al.*, 2014a]. The Pacific storm track is a major driving force of global weather patterns, especially for areas downstream, such as North America, and is also a key component in the transport of heat and moisture from low to high latitudes. Notably, Chinese air pollution impacts the air quality in the United States [Ewing *et al.*, 2010; Wang *et al.*, 2014a; Lin *et al.*, 2014]. Measurements on the U.S. West Coast have revealed that nearly a 30% of certain pollutants, particularly sulfate and lead, originated in China [Ewing *et al.*, 2010; Lin *et al.*, 2014].

iii) Visibility

Visibility, the distance we are able to perceive, is determined by the mass and size distribution of particles in the atmosphere. When aerosols are sufficiently large, they scatter and absorb sunlight efficiently enough to reduce visibility (often resulting in haze) and reddened sunrises and sunsets. Field results reveal that 72% of light scattering is attributed primarily to aerosols with sizes that range from 260 to 900 nm, corresponding to the wavelength band of visible light [Lee *et al.*, 2005]. Sulfate has been found to be a dominant aerosol that affects both the light scattering coefficient and visibility. When the particles are small (diameter < 0.5 μm) the amounts of light is equally scattered in the forward and backward directions, referred to as Rayleigh scattering [Seinfeld and Pandis, 2006]. As the particle size increases, solar radiation is more efficiently scattered in the forward direction. When the particles are roughly the same size as the incoming solar radiation, all wavelengths of visible light are scattered

nearly equally, and the haze appears to be white or gray due to Mie scattering, as can be seen in Figure 1.

Recent severe haze events in China have attracted significant public attention due to the severely reduced visibility and unprecedentedly high pollutant concentrations caused by the rapidly expanding economic and industrial developments. Observations by the Chinese Meteorological Association reveal that the visibility has significantly decreased over the last 50 years in many locations in China (Figure 2) [Zhang *et al.*, 2012]. In one extreme example, the city of Harbin in northern China was forced to cancel school, temporarily shut down the airport, and suspend bus routes because the visibility was less than 50 meters (164 feet) [Associated Press, 2013].

iv) Air Quality Standards

The U.S. EPA has established standards for six "criteria" pollutants which are considered harmful to public health and the environment: sulfur dioxide, nitrogen

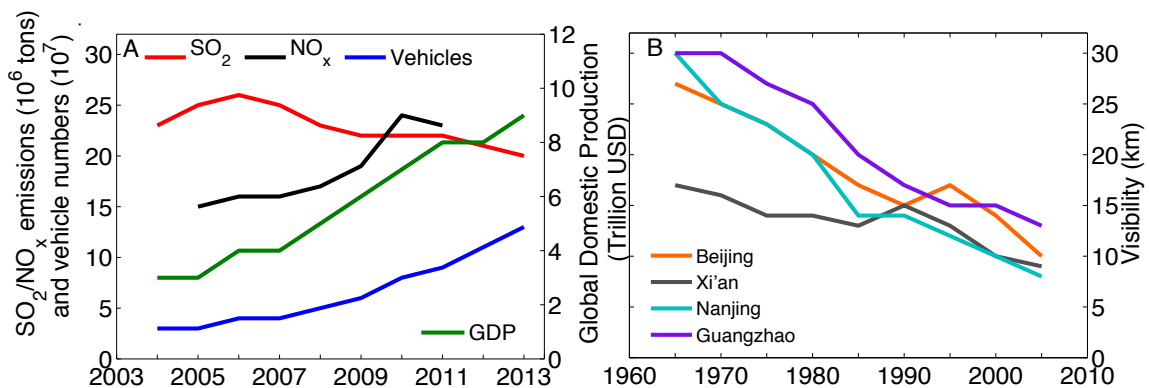


Figure 2. Historic trends in A) SO₂ and NO_x concentrations, the number of vehicles, and the gross domestic product in China, and B) the visibility in Beijing, Xi'an, Nanjing, and Guangzhou.

dioxide, carbon monoxide, lead, ozone, and PM. The U.S. EPA utilizes two benchmarks for determining national standards: ‘primary standards’, which focus on protecting public health, and ‘secondary standards’, which protect the public against adverse environmental effects [U.S. EPA, 2015]. U.S. law requires primary standards to protect, with an adequate margin of safety, the health of the public most at risk from pollutant exposure, such as individuals with heart or lung disease, asthmatics, children, the elderly, and people of lower socioeconomic status. Secondary standards must protect the public welfare from both known and anticipated adverse effects, such as decreased visibility from haze and damage to animals, crops, vegetation, and buildings. For comparison, Table 2 presents a comparison of the U.S. standards with the ambient air quality standards in China, as detailed in GB 3095-2012, and the air quality standards that have been suggested by WHO. The Chinese standards were phased-in beginning in 2012 in the Beijing-Tianjin-Hebei, Yangtze River Delta, and Pearl River Delta regions and will be enforced for all cities nationwide in 2016. The Chinese government has established two benchmarks for determining national standards: Class 1 standards, which apply to special regions such as national parks, and Class 2 standards, which apply to all other areas, including residential, commercial, industrial urban, and rural areas. WHO has established four air quality benchmarks [WHO, 2006]. The air quality guideline (AQG) indicates the lowest concentrations at which cardiopulmonary cancer mortality have been shown to increase with more than 95% confidence in response to long-term exposure. Interim target-1 (IT-1) indicates the concentrations that have been associated with an approximate 15% increases long-term mortality risk relative to the AQG level.

Standard	U.S. Primary	U.S. Secondary	China (I)	China (II)	WHO IT-1	WHO AQG
CO 1 hour ave.	35 ppm	-	10 mg m ⁻³	10 mg m ⁻³	-	30 mg m ⁻³
CO 24 hour ave.	9 ppm ****	-	4 mg m ⁻³	4 mg m ⁻³	-	10 mg m ⁻³ ****
Lead annual ave.	0.15 **	0.15 **	0.5	0.5	-	0.5
NO ₂ 1 hour ave.	100 ppb	-	200	200	-	200
NO ₂ annual ave.	53 ppb	53 ppb	40	40	-	40
NO ₂ 24 ave.	-	-	80	80	-	-
O ₃ 1 hour ave.	-	-	160	200	-	200
O ₃ 8 hour ave.	75 ppb	75 ppb	100	160	160	100
PM ₁₀ annual ave.	-	-	40	70	70	20
PM ₁₀ 24 hour ave.	150	150	50	150	150	50
PM _{2.5} annual ave.	12	15	15	35	35	10
PM _{2.5} 24 hour ave.	35	35	35	75	75	25
SO ₂ 1 hour ave.	75 ppb	500 ppb ***	150	500	-	500 *
SO ₂ annual ave.	-	-	20	60	-	50
SO ₂ 24 hour ave.	-	-	50	150	125	20
TSP 24 hour ave.	-	-	120	300	-	-
TSP annual ave.	-	-	80	200	-	-

*10 minute ave. ** 3 month rolling ave. *** 3 hour max **** 8 hour ave.

Table 1. Air pollution standards established by the United States, China, and The World Health Organization. The concentrations have been listed in $\mu\text{g m}^{-3}$ unless otherwise indicated.

Interim target-2 (IT-2) indicates the concentrations that reduce the risk of premature mortality by approximately 6% relative to the IT-1 level. Interim target-3 (IT-3) indicates the concentrations that reduce the mortality risk by approximately 6% relative to the IT-2 level. While publishing the actual concentration is the most precise way of quantitatively describing air pollution, this method isn't the most ideal for public awareness and multiple pollutant comparisons. Therefore, pollution monitors often display real-time data in terms of the air quality index (AQI). The AQI qualitatively describes air pollution as 'good', 'moderate', 'unhealthy for sensitive groups', 'unhealthy', 'very unhealthy', and 'hazardous', which is easily comprehensible to the general public. The AQI indicates the health effects of continuous exposure over a 24 hour period. A ranking of 'good' (i.e. AQI 0 – 50) indicates that the air quality is considered satisfactory and poses little or no risk to the public. A ranking of 'moderate' (i.e. AQI 51 – 100) indicates that the air quality is acceptable; however, some pollutants may pose a moderate health concern for certain extremely sensitive individuals. A ranking of 'unhealthy for sensitive groups' (i.e. AQI 101 – 150) indicates that the air quality may affect certain people (i.e. individuals with lung disease, older adults, and children), although the public is not likely to be affected overall. A ranking of 'unhealthy' (i.e. AQI 151 – 200) indicates that all individuals may begin to experience adverse health effects due to the poor air quality. A ranking of 'very unhealthy' (i.e. AQI 201 – 300) indicates that the entire population may experience serious health effects. A ranking of 'hazardous' (i.e. AQI greater than 300) indicates that the air quality triggers an emergency health warning, and the entire population is likely to be affected. Both the

AQI	United States		China		Europe	
	Name	24 hour ave. ($\mu\text{g m}^{-3}$)	Name	24 hour ave. ($\mu\text{g m}^{-3}$)	Name	24 hour ave. ($\mu\text{g m}^{-3}$)
0 - 50	Good	< 12	Excellent	< 35	Very Low	< 10
51 - 100	Moderate	12.1 – 35.4	Good	35 – 75	Low	10 – 20
101-150	Unhealthy for Sensitive Groups	35.5 – 55.4	Light	75 – 115	Medium	20 – 30
151 - 200	Unhealthy	55.5 – 150.4	Moderate	115 – 150	High	30 – 60
201 - 300	Very Unhealthy	150.5 – 250.4	Heavy	150 – 250	Very High	> 60
> 300	Hazardous	> 250.5	Serious	> 250		

Table 2. Comparison of the air quality index for PM_{2.5} in the United States, China, and Europe.

U.S. and China use AQI systems that rank the air quality from 0 – 500, however, confusion can arise due to the countries employing different thresholds for each level (see Table 2). Overall, the U.S. standards are stricter at lower concentrations, but compare similarly at higher concentrations. For comparison, the AQI values used by the European Union have also been displayed.

CHAPTER II

WHICH ATMOSPHERIC SPECIES ARE INTEGRAL FOR AEROSOL FORMATION IN THE ATMOSPHERE? INVESTIGATION INTO THE ROLE OF ORGANICS IN ATMOSPHERIC NEW PARTICLE FORMATION

i) Introduction

New particle formation (NPF) events have been observed for many years and account for the production of more than 50% of the global CCN concentration [Merikanto *et al.*, 2009], but the chemical species and mechanisms responsible for NPF have yet to be fully understood or reproduced in atmospheric models. While sulfuric acid has been identified as essential for atmospheric nucleation to occur because sulfate represents an important component of the nucleation mode aerosol, a variety of other species have also been associated with aerosol nucleation, including ammonia, amines, organic acids, ion clusters, cosmic rays, and pre-existing background aerosols [deReus *et al.*, 1998; Kavouras *et al.*, 1998; Korhonen *et al.*, 1999; Kulmala *et al.*, 2000; Yu and Turco, 2001; Zhang *et al.*, 2004; Kurtén *et al.*, 2008; Zhang *et al.*, 2009; Sipilä *et al.*, 2010; Wang *et al.*, 2010; Kirkby *et al.*, 2011; Yu *et al.*, 2012; Zhang *et al.*, 2012; Kirkby *et al.*, 2011; Kulmala *et al.*, 2014; Riccobono *et al.*, 2014]. However, the nucleation binary theory (water and sulfuric acid) does not explain atmospheric NPF at all the observed locations, and it is clear the presence of sulfuric acid, organic amines, or ammonia is not enough to induce nucleation as all three compounds have been measured at locations where NPF is rarely observed such as Atlanta, Georgia, the Amazon Basin, and Tijuana, Mexico [Zhou *et al.*, 2002; Woo *et al.*, 2010; Levy *et al.*, 2014a]. Solving

this “nucleation puzzle” is necessary to assess the role that NPF has in the tropospheric loading of atmospheric aerosols and its impact on climate, cloud formation, and regulatory implications [Andreae, 2013]. Atmospheric measurements of NPF reveal distinct spatial patterns in the global continental troposphere: NPF occurs on a regular basis near boreal forests [Boy et al., 2004; Kulmala et al., 2004], sporadically in many urban centers [Dunn et al., 2004; Stanier et al., 2004; Levy et al., 2013], but rarely in other locations, including the Amazon Basin [Zhou et al., 2002], the 1999 Atlanta supersite [Woo et al., 2001], the 2009 Study of Houston Radical precursors (SHARP) field campaign [Levy et al., 2013], Tijuana, Mexico during the 2010 California – Mexico (Cal-Mex) field study [Levy et al., 2014a], and during the southeastern U.S. during the 2013 Southern Oxidant and Aerosol Study (SOAS) field campaign [Uin et al., 2013]. These environments exhibit distinct species of anthropogenic and biogenic VOCs, i.e. higher concentrations of pinenes in boreal forests, elevated aromatic hydrocarbons combined with biogenic VOCs in urban regions, higher concentrations of isoprene in the Amazon Basin, and anthropogenically dominated VOCs at the U.S.-Mexico border. The photochemical oxidation of VOCs emitted from the biosphere, as well as, anthropogenic activities lead to the formation of non-volatile products, some of which may contribute to aerosol nucleation and growth [Ehn et al., 2007]. Biogenic sources dominate VOC emissions globally ($\sim 1150 \text{ Tg yr}^{-1}$) when compared to anthropogenic sources ($\sim 142 \text{ Tg yr}^{-1}$), representing a major source of secondary organic aerosols (SOA) (up to 90% or more by mass) in the troposphere [Goldstein and Galbally, 2007; Merikanto et al., 2009; Sipilä et al., 2010; Hallar et al., 2011; Shen et al., 2011; Pöhlker et al., 2012; Jung et al.,

2013]. *O'Dowd et al.* [2002] determined that the clusters produced during NPF events in the boreal forests in Finland were most likely composed of organic compounds such as pinic acid or *cis*-pinonic acid and that the nucleation mode particles could not be inorganic in composition.

The formation of thermodynamically stable clusters from low vapor pressure atmospheric gas phase species is known as homogeneous nucleation. The process leading to new particles is frequently divided into two-steps: the formation of thermodynamically stable clusters and the subsequent growth of these clusters. Formation of molecular clusters in the atmosphere occurs through random collisions and rearrangements of atoms or molecules of the gas phase species. In order for nucleation to occur, clusters must overcome the 'nucleation barrier'. Newly formed clusters are exothermic; therefore, they are thermodynamically favorable according to the first law of thermodynamics. However, the clusters are unfavorable according to the second law of thermodynamics [*Zhang et al.*, 2011]. Hence, a free energy barrier must be overcome before the transformation to a cluster becomes spontaneous. In the atmosphere, several species are often needed for nucleation to occur, since the equilibrium vapor pressures of mixed systems are typically lower than pure systems, and homomolecular nucleation requires an extremely high supersaturation [*Zhang et al.*, 2011]. Given that pristine high supersaturation, supercooled environments are not common in the atmosphere, heterogeneous nucleation, i.e. nucleation that occurs on pre-existing small particles or ions which assist in overcoming the free energy barrier, is the dominant mechanism in the environment. Another major restriction on the nucleation and growth of atmospheric

nanoparticles is that the elevated equilibrium vapor pressures above small clusters, resulting from the increased surface curvature at these sizes, inhibits the growth of freshly nucleated nanoparticles, known as the Kelvin or curvature effect. The freshly nucleated nanoparticles must also compete with capture and removal processes by coagulation with other pre-existing aerosols. Several prominent homogeneous nucleation theories have been suggested to explain the first step in nucleation: 1) binary nucleation of sulfuric acid and water, 2) ternary nucleation of sulfuric acid, water, and ammonia, 3) and ion-induced nucleation, and it is probable that the distinctive mechanisms dominate in different locations [Korhonen *et al.*, 1999; Kulmala *et al.*, 2004; Kurtén *et al.*, 2008].

Once a cluster has reached the size of the ‘critical cluster’, the size for which the probabilities of particle growth and decay are equal, the droplet will persist and most likely grow by condensation of gas phase molecules. Clusters with diameters smaller than the critical size are more likely to undergo evaporation than condensation, so they frequently dissociate into the separate gas molecules again [Zhang *et al.*, 2011]. After reaching a critical size, further growth of the cluster becomes spontaneous. Other condensable species, such as supersaturated organic compounds with higher nucleation barriers due to a large Kelvin effect, are thought to be largely responsible for the growth of freshly nucleated particles. The nucleation rate (J) is the number of clusters that grow beyond the critical size per second.

NPF events are typically identified by the signature ‘banana curve’ as shown in Figure 3A. NPF events are typically comprised of three phases: 1) rapid increase in the particle number concentration of small particles (< 30 nm), 2) ongoing particle growth

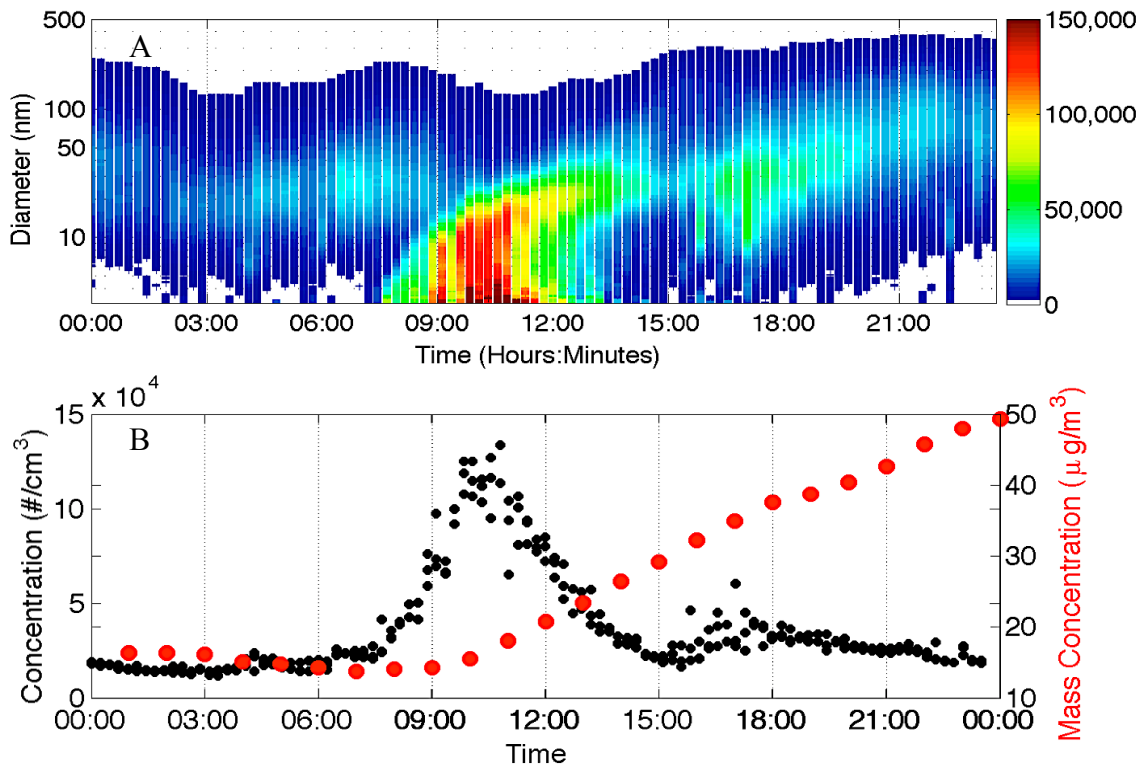


Figure 3. A) The iconic ‘banana curve’ that indicates new particle formation. B) The subsequent changes in the total number (black dots) and mass concentration (red dots) during and after new particle formation.

due to the condensation of gas phase species, typically in the size range 30 – 100 nm but the resultant particle size is dependent on the environment, and 3) the gradual decrease of the particle number concentration due to coagulation and dilution. Some NPF events are called ‘apples’ because they solely exhibit the first phase; therefore, they are observed as highly concentrated, short-lived pulses of small particles. NPF events do not contribute significantly to the mass concentration initially (Figure 3B); however, as the particles grow, the mass increases, which can result in a rapid increase in the PM_{2.5} mass concentration.

Many NPF laboratory studies have been conducted to try to elucidate what species regulate NPF events. Experiments have frequently been conducted with flow reactors [e.g., *Berndt and Böge*, 1997; *Ball et al.*, 1999; *Bonn and Moortgat*, 2002; *Wang et al.*, 2009; *Berndt et al.*, 2010; *Sipilä et al.*, 2010; *Wang et al.*, 2010] and aerosol chambers [e.g., *Forstner et al.*, 1997; *Hallquist et al.*, 1999; *Iinuma et al.*, 2004; *Riccobono et al.*, 2014] to try to isolate aerosol nucleation and growth. In particular, the nucleation potential of H₂SO₄ and α -pinene have been extensively studied [e.g., *Marti et al.*, 1997; *Hoffman et al.*, 1998; *Ball et al.*, 1999; *Bonn and Moortgat*, 2002; *Iinuma et al.*, 2004; *Wang et al.*, 2009]. Many nucleation chamber studies introduce to other atmospherically relevant species, such as seed aerosols [e.g., *Stern et al.*, 1987; *Odum et al.*, 1996; *Forstner et al.*, 1997; *Iinuma et al.*, 2004; *Kroll et al.*, 2006;], nitrogen oxides (NO_x, NO_x = NO + NO₂) [e.g., *Aschmann et al.*, 1998; *Stern et al.*, 1987; *Wildt et al.*, 2013], or sulfur dioxide (SO₂) / sulfuric acid [e.g., *Kim et al.*, 1998; *Berndt et al.*, 2010; *Sipilä et al.*, 2010; *Riccobono et al.*, 2014], to observed the modified NPF efficiency. Several species have been used to initiate the nucleation process, including ozone [e.g., *Bonn and Moortgat*, 2002; *Iinuma et al.*, 2004;], hydrogen peroxide [e.g., *Hildebrandt et al.*, 2009], NO₃ [e.g., *Berndt and Böge*, 1997; *Hoffman et al.*, 1998; *Bonn and Moortgat*, 2002], and CH₃ONO [e.g., *Aschmann et al.*, 1998; *Bonn and Moortgat*, 2002]. *Bonn and Moortgat* [2002] compared the efficiency of NPF from the oxidation of α - and β -pinene when ozone, OH, and NO₃ were used as the oxidant. The results indicated a considerably higher nucleation potential of the ozonolysis mechanism than either OH or NO₃. Also of the three oxidants, only the ozonolysis reaction was effected by water vapor

concentration. *Ball et al.* [1999] conducted experiments using the binary H₂SO₄-H₂O vapor system and reported that a critical cluster typically consisted of 7–8 molecules of H₂SO₄ and 5 molecules of H₂O. *Sipilä et al.* [2010] reported that particles with diameters near 1.5 nanometers were observed immediately after their formation at atmospherically relevant sulfuric acid concentrations and correlations between measured nucleation rates and sulfuric acid concentrations suggest that freshly formed particles are composed of one to two sulfuric acid molecules. However, *Zhang* [2010] proposed that one or two sulfuric acid molecules (a monomer or dimer) are not large enough overcome the nucleation barrier, as a hydrated sulfuric acid dimer has a diameter of 0.7 nm, and the presence of organic acids may be required to form a critical nucleus. *Riccobono et al.* [2014] showed that sulfuric acid and oxidized organic species at atmospheric concentrations reproduce particle nucleation rates observed in the lower atmosphere. The experiments revealed the newly formed critical clusters contained both sulfuric acid and oxidized organic molecules. *Jokinen et al.* [2015] reported that extremely low volatile organic compounds promote aerosol particle formation. They showed that under atmospherically relevant concentrations, species with an endocyclic double bond efficiently produce extremely low volatile organic compounds, and that the ozonolysis of monoterpenes produced a higher particle concentration than the OH radical-initiated reactions. Also, isoprene-derived products were found to suppress atmospheric new particle formation, but they supported particle growth. *Kiendler-Scharr et al.* [2009] presented evidence from experiments conducted in a Jülich Plant Aerosol Chamber that revealed that isoprene significantly inhibits new particle formation due to the high

reactivity of isoprene with OH. Amines and carboxylic acids have also been recognized as important precursor species in atmospheric new particle formation [Hoffman *et al.*, 1998; Ball *et al.*, 1999; Yu *et al.*, 2012]. The initial concentration of the reacted species has also been found to alter the aerosol production in several of these chamber studies [Hallquist *et al.*, 1999; Bonn and Moortgat, 2002].

ii) Methodology

To assess the role of organic compounds in NPF, we performed laboratory studies of the homogenous nucleation from the photochemical oxidation of biogenic (α -pinene and isoprene) and anthropogenic (m-xylene and toluene) VOCs, which are described in Table 3 [Toby *et al.*, 1985; Seinfeld and Pandis, 2006]. All experiments

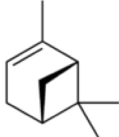
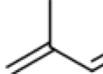
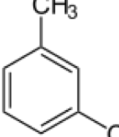
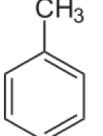
VOC	Molar Mass	K_{OH} ($\text{cm}^3 \text{ molecule}^{-1} \text{ s}^{-1}$)	K_{O_3} ($\text{cm}^3 \text{ molecule}^{-1} \text{ s}^{-1}$)	Structure
α -Pinene ($\text{C}_{10}\text{H}_{16}$)	136.24 g mol^{-1}	5.37×10^{-11}	8.66×10^{-17}	
Isoprene (C_5H_8)	68.12 g mol^{-1}	1.01×10^{-10}	1.28×10^{-17}	
m-Xylene (C_8H_{10})	106.16 g mol^{-1}	2.31×10^{-11}	8.48×10^{-22}	
Toluene (C_7H_8)	92.14 g mol^{-1}	5.63×10^{-12}	3.90×10^{-22}	

Table 3. Properties of the four VOCs utilized in the new particle formation experiments.

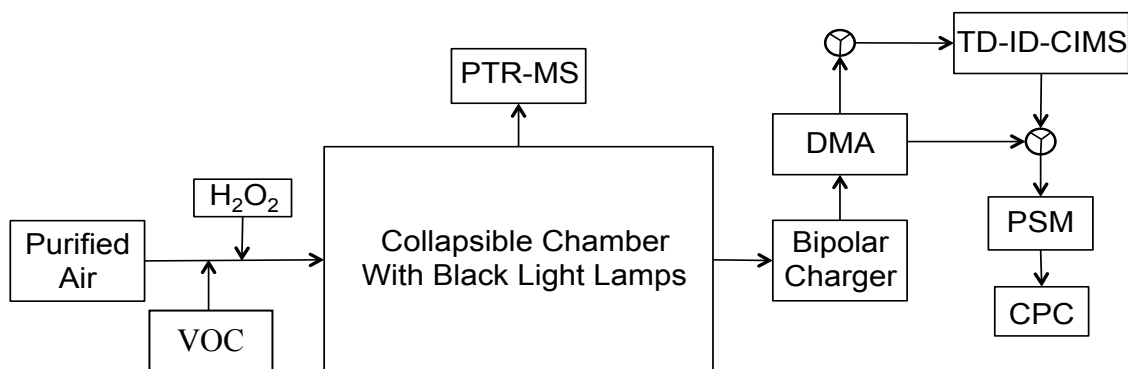


Figure 4. Schematic of instruments operated in new particle formation experiments.

were performed in a 1.2 m³ collapsible environmental chamber (Teflon® PFA) equipped with a row of nine black light lamps on two sides of the chamber (F30T8/350BL, Sylvania) and reflective aluminum sheets on all sides. The experiments were conducted with a comprehensive suite of instruments to detect the trace gases and nano-sized aerosols, including a compact proton transfer reaction – mass spectrometer (PTR-MS, Ionicon Analytik), an ultrafine condensation particle counter (CPC, model 3025A, TSI, Inc.), a nano differential mobility analyzer (NDMA, model 3081, TSI, Inc), a particle size magnifier (PSM), and a thermal desorption – ion drift – chemical ionization mass spectrometer (TD-ID-CIMS, Figure 4). The time-resolved particle size distributions, concentrations, and chemical compositions for 1.5 to 50 nm particles were obtained with this combination of instruments.

At the beginning of each experiment, the chamber was filled with ~750 liters of purified air. During experiments, the relative humidity and temperature in the chamber were approximately 8% and 302-304 K, respectively. Hydrogen peroxide was utilized in the experiments as an OH radical precursor ($\text{H}_2\text{O}_2 + h\nu \rightarrow 2\text{OH}$, $k_{300} = 5.26 \times 10^{-42} \text{ cm}^3$

molecule⁻¹ s⁻¹) [Sellevåg *et al.*, 2009]. Many NPF experimental studies utilize O₃ as the oxidizing agent; however, OH is the dominant oxidant for isoprene, m-xylene, and toluene and is comparable for α-pinene (0.21 versus 0.11 days, assuming 10⁶ molecules cm⁻³ and 50 ppb, for its reaction with OH and O₃, respectively) [Hoffmann *et al.*, 1998; Bonn and Moorgat, 2002]. The hydrogen peroxide aqueous solution (35 weight %, 200 μL) was injected into a glass reservoir and then flushed into the chamber with purified air. The VOCs were then injected into the glass reservoir and carried into the chamber by purified air. A filter with a Teflon liner and glass wool was placed between the glass reservoir and chamber to prevent any particulate matter from entering the chamber via the reservoir. After both injections, a fan was turned on for thirty seconds to thoroughly mix the gaseous species in the chamber. At this point, the inflow and outflow air valves were closed, and the nucleation occurred in a static system. Once the desired reactant concentration was established the black light lamps were turned on to initiate H₂O₂ photolysis. The lights remained on throughout the entire experiment. After the concentration reached a steady state, collection by the TD-ID-CIMS was initiated, which typically occurred for 2-6 hours depending on the initial concentration and species.

Throughout the experiment, the concentration of the VOC was then monitored by a PTR-MS as can be seen Figure 5A. PTR-MS is a very sensitive technique for real-time simultaneous monitoring of trace VOCs with a fast response time of less than 100 ms. PTR-MS instruments are known for their low detection limits down to parts per trillion (ppt) because it does not dilute low concentrated samples with a carrier gas and there is minimal precursor ions loss between the ion source and the drift tube. Also, the

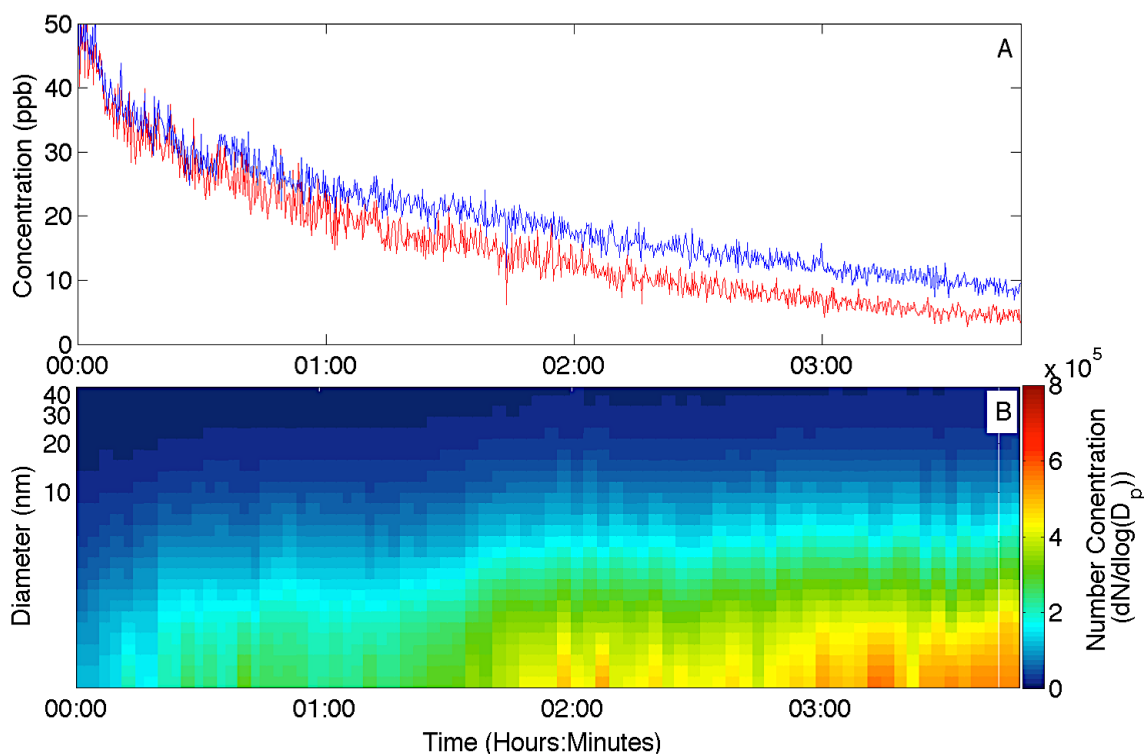


Figure 5. The A) concentration of isoprene (red) and α -pinene (blue) measured by the PTR-MS and B) size distributions of particles with a diameter between 1.5 and 40 nm.

hydronium, H_3O^+ , ions do not react with any of the major components present in clean air (i.e. nitrogen, oxygen, carbon dioxide, carbon monoxide, methane, and ozone) due to their low proton affinity, so this method is ideal for trace gases. Furthermore, proton ion transfer from H_3O^+ is a soft ionization method, which lessens fragmentation. The system was operated in multiple-ion mode, which simultaneously measures H_3O^+ (m/z 19), isoprene (m/z 69), toluene (m/z 93), m-xylene (m/z 107), and α -pinene (m/z 137). The TD-ID-CIMS has been proven to detect chemical species in the sub nanogram mass range and with a diameter less than 2 nm.

The size distribution and number concentration were determined using the DMA, PSM, and CPC. The DMA operated in a recirculating flow configuration, with a sheath

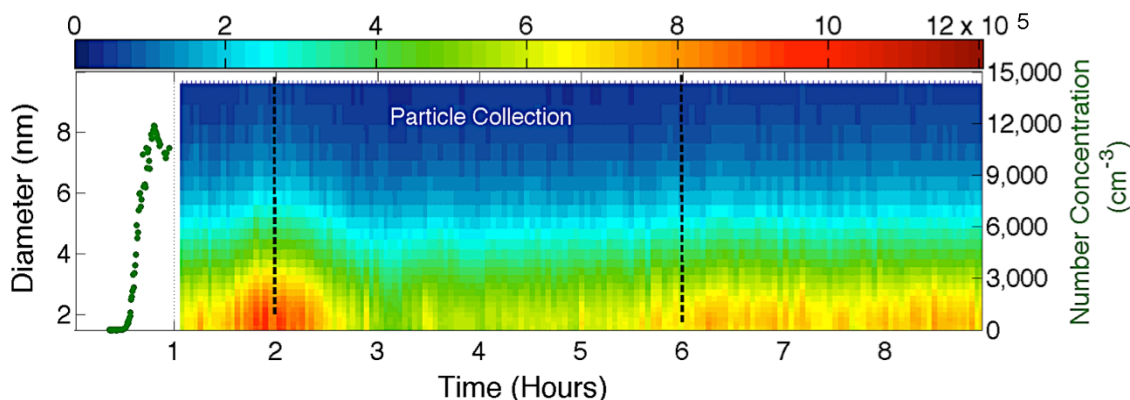


Figure 6. An example of the two methodologies utilized for collecting new particle formation data: the condensation particle counter, which determine the total concentration (shown in green dots) and scanning mobility particle sizing, which determines the particle size distribution (hours 2-9). The decrease in concentration between hours 2 and 6 is due to particles being collected by the TD-ID-CIMS to determine the chemical composition.

flow of 6.50 liters per minute (LPM) and a sample flow of 1 LPM. The relatively low sheath-to-sample flow ratio results in a better detection of small particle concentrations and a shorter residence time. A detailed description of the operating systems has been published previously [Khalizov *et al.*, 2009a, Pagels *et al.*, 2009; Xue *et al.*, 2009a, b]. The system was typically operated in one of two modes: scanning mobility particle sizing (i.e. DMA-PSM-CPC) and without size selections (PSM-CPC). The first mode obtains the size-resolved particle concentration as shown in Figure 6A, and the second mode calculates the total particle concentration as shown in Figure 6B. The PSM was used to enhance the detection of the number concentration of the nanoparticles since traditional CPCs fail to detect particle smaller than 3 nm [Xu *et al.*, 2014]. This is necessary since critical nuclei in the atmospheric nucleation are roughly 1.5 nm in size.

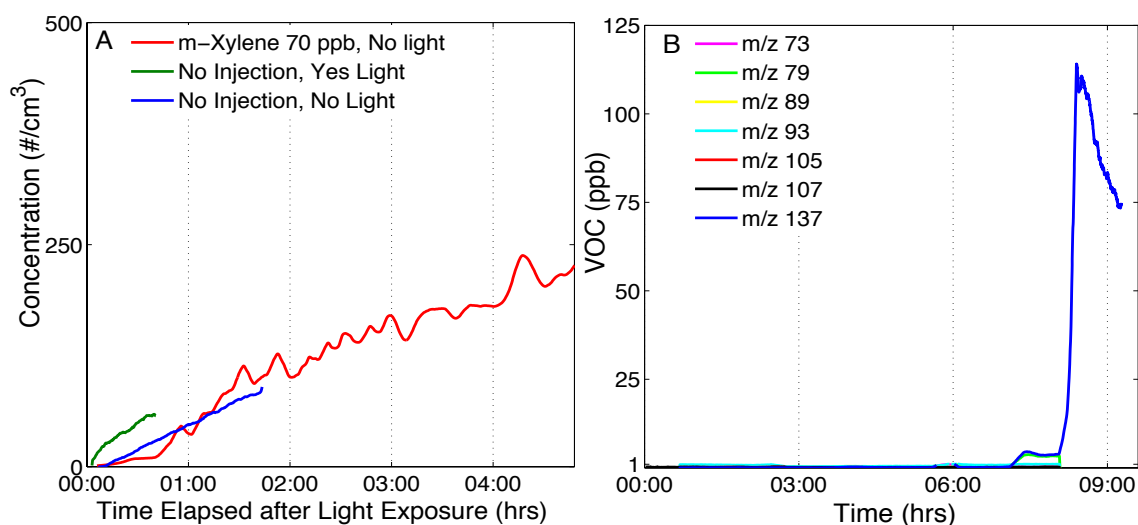


Figure 7. Background concentration of particles and VOCs in the chamber as a function of time.

The chemical composition was determined by utilizing a TD-ID-CIMS equipped with a triple quadrupole mass analyzer. The nucleated particles generated in the chamber were charged using a unipolar ²¹⁰Po charger and electrostatically deposited on a charged platinum precipitator. The collected particle mass was subsequently thermally desorbed at 300 °C and analyzed. The reagent ions H₃O⁺ and CO₃⁻/CO₄⁻ were employed for positive mode and negative mode analysis, respectively. The collection varied between two and four hours depending on the concentration of particles in the chamber.

Between each experiment, the chamber was cleaned overnight for at least 12 hours with a steady stream of purified air (Aadco 737-11, Aadco Inc.) and irradiated by black light lamps to remove any residual chemicals. Before each experiment, the chamber had a particle number concentration less than 0.01 cm⁻³ and the total hydrocarbons were less than 1 part per billion (ppb). Blank and background experiments

have been performed under conditions, such as VOC injection without black lights, no VOC injection with black lights, and neither VOC or black lights. No significant change in particle size or mass was observed during these experiments as can be seen in Figure 7A. Figure 7B shows the absence of VOCs in the chamber before an experiment.

iii) Results and Discussion

Figure 8 exhibits the concentrations of nucleation mode particles formed in the

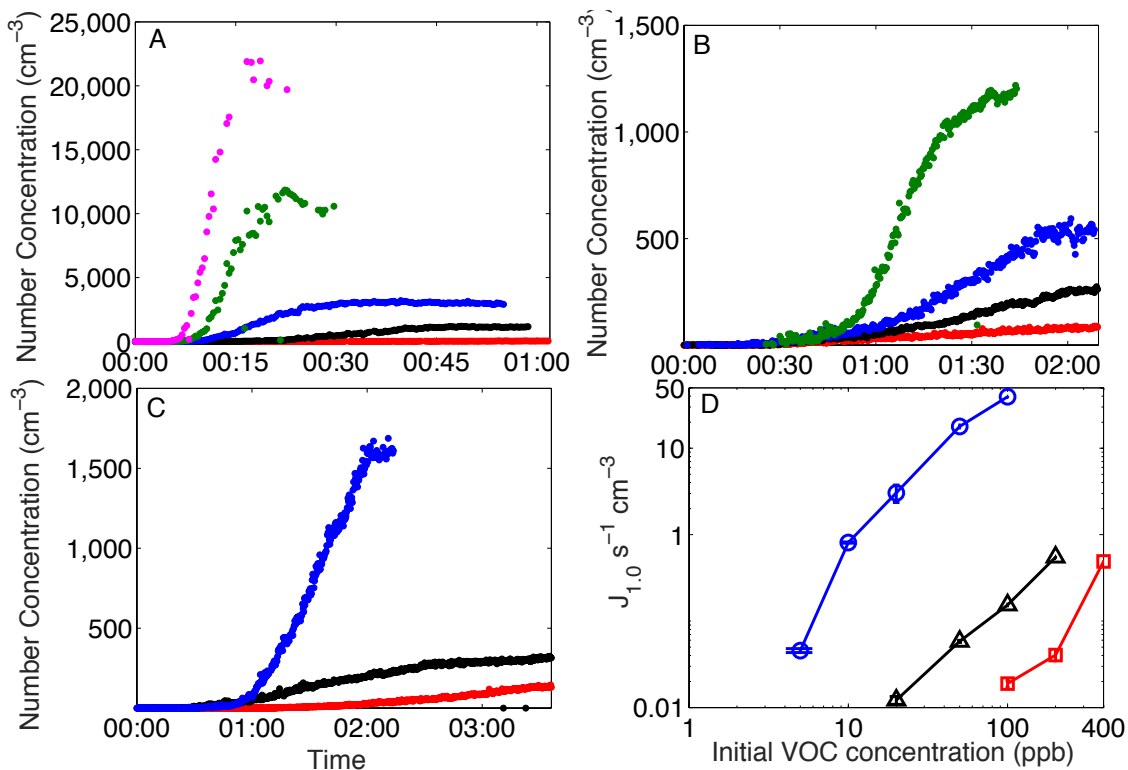


Figure 8. The concentration of particles formed from the photochemical oxidation of A) α -pinene with an initial concentration of 5 (red), 10 (black), 20 (blue), 50 (green), and 100 ppb (pink); B) m-xylene with an initial concentration of 20 (red), 50 (black), 100 (blue), and 200 ppb (green); and C) toluene with an initial concentration of 100 (red), 200 (black), and 400 ppb (blue) as a function of time. D) The new particle formation rates (J , $s^{-1} cm^{-3}$) for α -pinene (blue circles), m-xylene (black triangles), and toluene (red squares) at various initial concentrations

chamber as a function of time after the photochemical oxidation was initiated for A) α -pinene, B) m-xylene, and C) toluene, and the D) corresponding formation rates. The photochemical oxidation of α -pinene produced the highest concentration of new particles, followed by m-xylene, and then toluene (also shown in Figure 9). Isoprene did not produce NPF even at unrealistically high concentrations (500 ppb), which is in agreement with several previous studies [*Kiendler-Scharr et al.*, 2009; *Kanawade et al.*, 2011]. The formation rates of α -pinene with initial concentrations of 5, 10, and 20 ppb were less than $5 \text{ s}^{-1} \text{ cm}^{-3}$, but the formation rate was significantly enhanced at 50 ppb ($\sim 25 \text{ s}^{-1} \text{ cm}^{-3}$) and 100 ppb ($\sim 51 \text{ s}^{-1} \text{ cm}^{-3}$). The formation rates of m-xylene and toluene ranged between 0.01 and $0.65 \text{ s}^{-1} \text{ cm}^{-3}$. Increasing the initial concentrations resulted in a higher concentration of nucleated particles and a faster equilibrium time. The equilibrium time indicates the amount of time lapse before the concentration reaches a

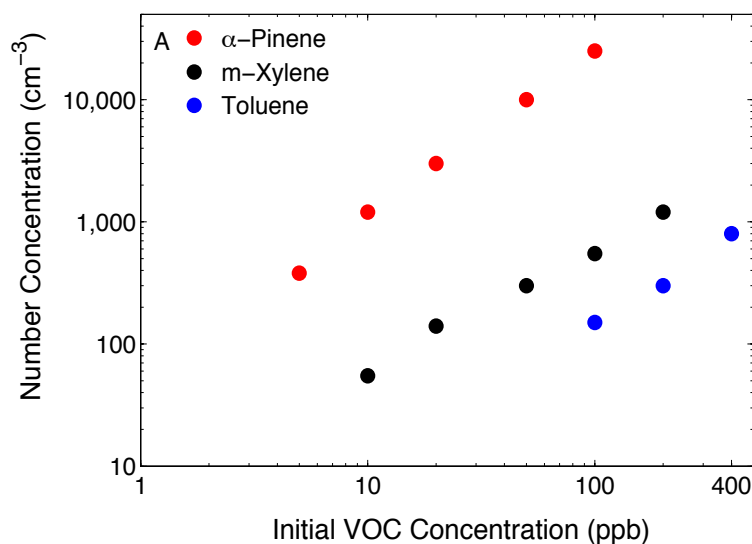


Figure 9. A comparison of the number concentration (cm^{-3}) produced from the photochemical oxidation of α -pinene (red), m-xylene (black), and toluene (blue) at various initial concentrations.

steady state. For example in Figure 6B, the equilibrium time would be ~30 minutes. In the α -pinene experiment with an initial concentration of 100 ppb, the resultant particle concentration stabilized 15 minutes after light exposure near 2.3×10^4 molecules cm^{-3} ; whereas, the 5 ppb experiment required 75 minutes to stabilize near 50 molecules cm^{-3} . Comparing the 100 ppb experiments for each VOC, the elapsed time before the concentration stabilized was significantly longer for m-xylene (120 minutes) and toluene (210 minutes) than α -pinene (15 minutes). In the toluene experiments, NPF only occurred after a certain threshold concentration was exceeded, which is substantially higher than the concentration observed in the ambient atmosphere.

Figure 10 shows the Selected Ion Monitoring (SIM) of the monomers (Figure 10A-C) and dimers (Figure 10D-F) produced by the oxidation α -pinene, m-xylene, and toluene determined by the TD-ID-CIMS. Figure 10A reveals the presence of several organic compounds generated after the oxidation of α -pinene. The mass-to-charge ratios (m/z) at 169, 171, 173, 185, 187, and 201 have been assigned to pinonaldehyde, pinalic acid, norpinic acid, pinonic acid, pinic acid, and hydroxypinonic acid, respectively [Hoffman *et al.*, 1998]. This is consistent with previous results that indicated that the oxidation of α -pinene might proceed through several reaction channels leading to a variety of different chemical structures including monocarboxylic and dicarboxylic acids [Hoffman *et al.*, 1998; Boy *et al.*, 2004]. Pinonaldehyde has a higher volatility and is not thought to be a significant promoter of particle nucleation, but has been observed in the particle phase during nucleation events [Kavouras *et al.*, 1999; Boy *et al.*, 2004]. Moreover, mass region corresponding to the dimerized products of the oxidation of

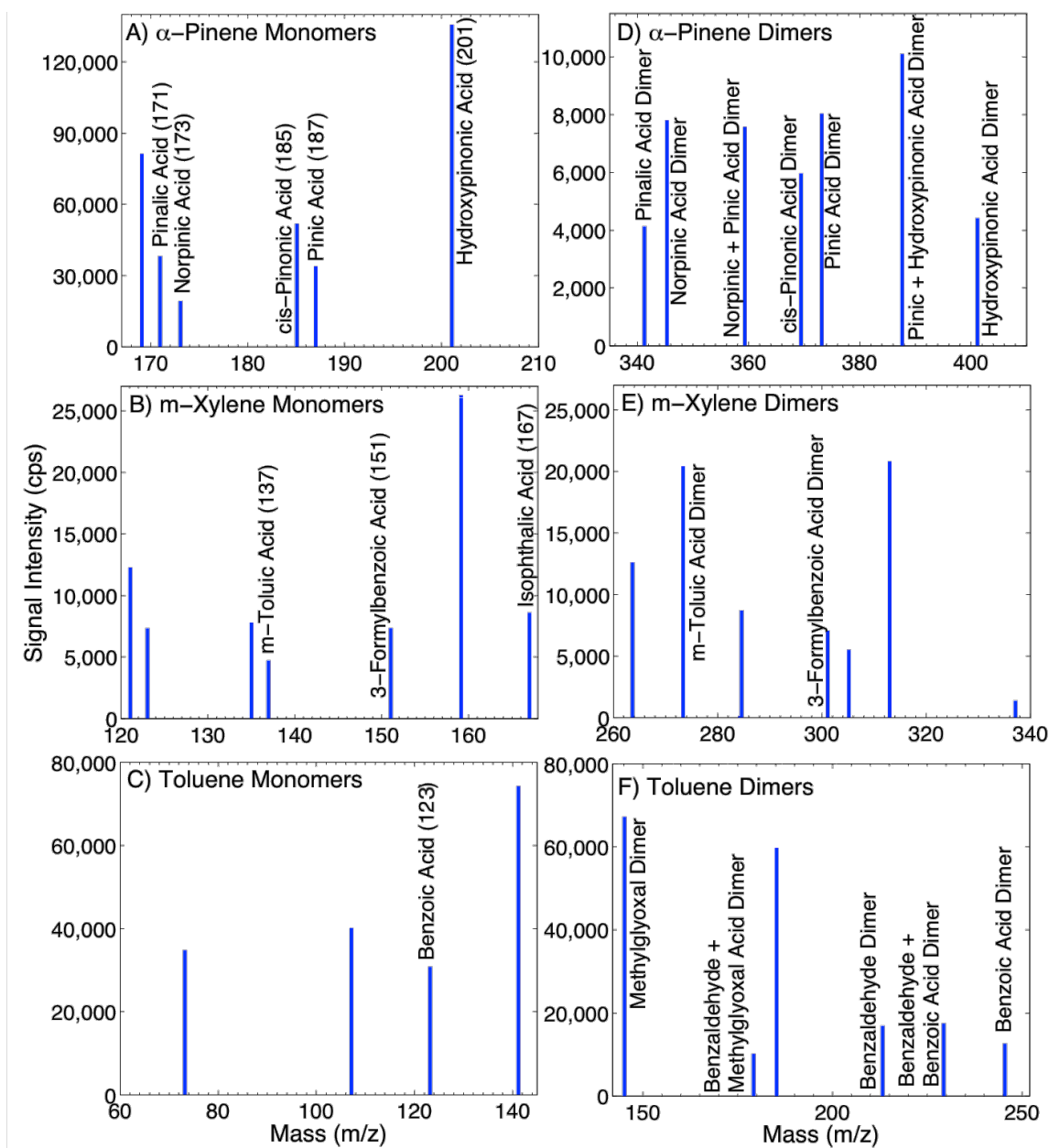


Figure 10. A-C) The protonated monomers of the oxidation products of α -pinene, m-xylene, and toluene shown in the mass-to-charge ratio (m/z) determined by TD-ID-CIMS analysis of the particle composition in positive ion mode. D-F) The protonated dimers of the corresponding oxidation products.

α -pinene (Figure 10D) revealed the presence of both homomolecular and

heteromolecular dimers of the various organic acids, especially diprotic acids (i.e. pinic and norpinic acid).

Figure 10B shows the chemical composition of particles formed in the chamber from the oxidation of *m*-xylene in the nucleation chamber. As indicated in the mass spectrum, the photooxidation of *m*-xylene produces *m*-tolualdehyde, 2,6-xylenol isophthalaldehyde, *m*-toluic acid, 3-formylbenzoic acid, and isophthalic acid, which have all been previously observed as products from the oxidation of *m*-xylene in field observation [Forstner *et al.*, 1997; Zhao *et al.*, 2005a]. However, the mass spectrum of the dimerized products (Figure 10E) revealed few acidic dimers, limited to the dimers of *m*-toluic acid and 3-formylbenzoic acid. This observation suggests that as the presence of nonacidic monomers increases, the efficiency of particle formation decreases, as there are fewer low volatility acidic species able to contribute to the critical nuclei.

Figure 10C exhibits the chemical analysis of particles formed from the oxidation of toluene in the nucleation chamber. The monomer mass spectrum revealed the presence of methylglyoxal, benzaldehyde, and benzoic acid, and the ion peak at $m/z = 141$ may be the epoxy dicarbonyl [Yu and Jeffries, 1997; Hamilton *et al.*, 2005; Wu *et al.*, 2014]. Figure 10F demonstrates that only two of the detected dimerized products were acidic in nature: the homomolecular dimer of benzoic acid and the heteromolecular dimer of benzaldehyde and benzoic acid at $m/z = 229$. Although benzaldehyde does not have a carboxylic group to hydrogen bond with benzoic acid, the presence of this m/z peak at 229 may correspond to the adduct of benzoic acid with benzaldehyde.

An investigation into the presence of sulfate species in the chamber and the possible clustering of VOC oxidation species with sulfate species was conducted with the TD-ID-CIMS. The mass spectrum did not identify any significant peaks that could be attributed to VOC-sulfate clusters. Also considering the relative concentrations of any potential sulfate contaminants and VOCs in the chamber, we have determined that sulfate did not play a role in the nucleation events observed in these experiments.

We also investigated the modification of the NPF efficiency in the presence of multiple VOCs, which is a better representation of an urban atmosphere. Figure 11A-C displays the particle concentration produced by the photooxidation of α -pinene (20 ppb), m-xylene (200 ppb), and toluene (400 ppb) combined with increasing concentrations of isoprene. In all the experiments, the mixtures generated a lower concentration of particles than the pure sample, and increasing the concentration of isoprene further suppressed nucleation. The overall concentration of 20 ppb α -pinene, 200 ppb m-xylene, and 400 ppb toluene was reduced by 62, 68, and 78%, respectively, when an equal concentration of isoprene (i.e. 20, 200, and 400 ppb, respectively) was added to the chamber. Adding isoprene also reduced the rate of formation of particles in the α -pinene and m-xylene experiments. For example, adding 20 and 100 ppb of isoprene to 20 ppb of α -pinene increased the experimental time by about 30 and 90 minutes, respectively. The suppression of NPF by isoprene has also been observed in field and plant chamber studies [Kiendler-Scharr *et al.*, 2009; Kanawade *et al.*, 2011]. m-Xylene and toluene also substantially reduced the concentration of newly formed particles of α -pinene, by 90 and 70%, respectively (Figure 11D). The combination of m-xylene and toluene also

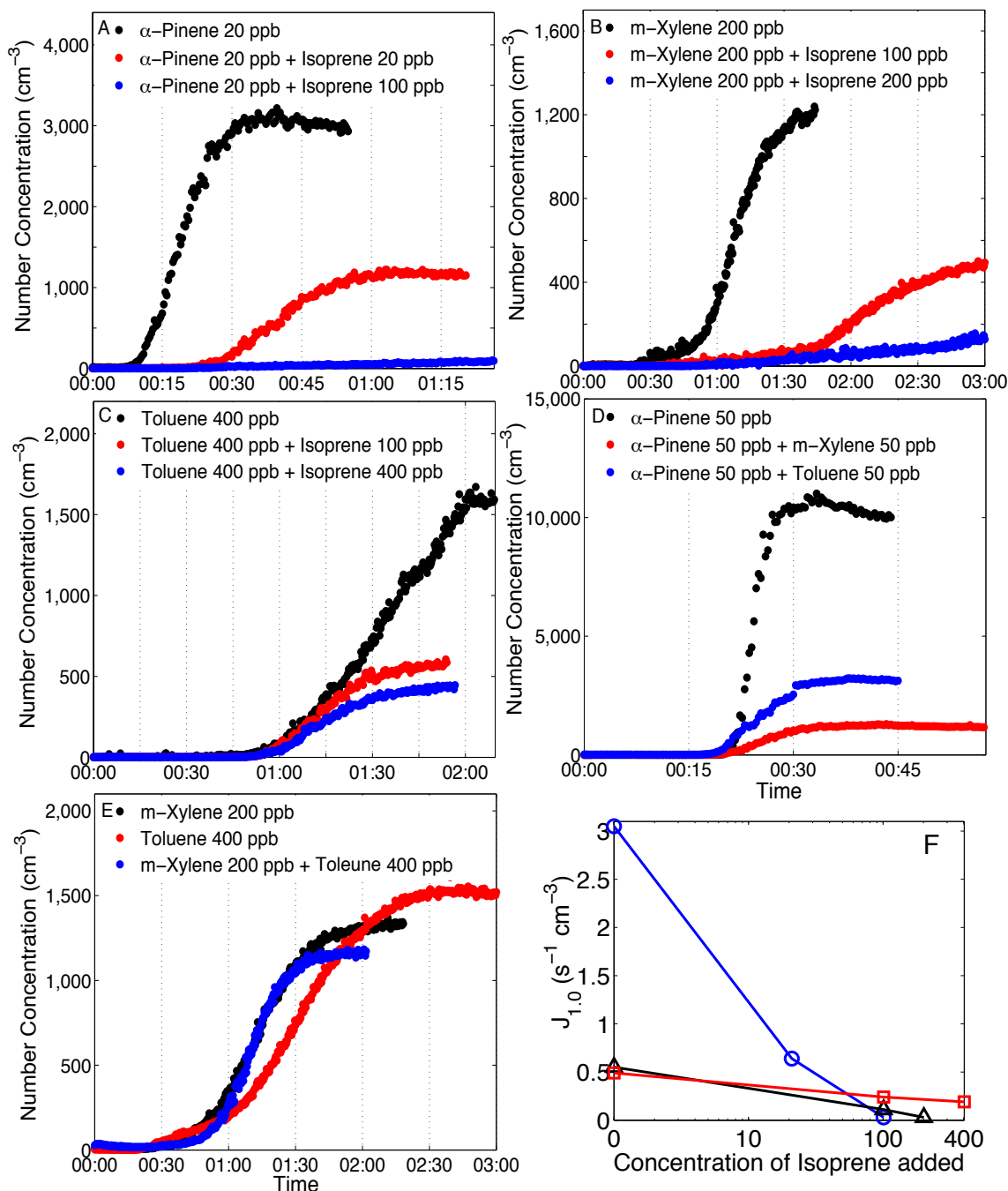


Figure 11. The concentration of particles (cm^{-3}) formed from the photochemical oxidation of A) 20 ppb of α -pinene mixed with increasing concentration of isoprene, B) 200 ppb of m-xylene mixed with increasing concentration of isoprene, C) 400 ppb of toluene mixed with increasing concentration of isoprene, D) 50 ppb of α -pinene mixed with 50 ppb of m-xylene and toluene, and E) 200 ppb of m-xylene, 400 ppb of toluene, and their mixture. F) Comparison new particle formation rates (J , $\text{s}^{-1} \text{cm}^{-3}$) from the photooxidation of α -pinene (blue circles), m-xylene (black triangles), and toluene (red squares) with increasing isoprene concentrations.

resulted in a diminished particle concentration, but this reduction was inconsequential (Figure 11E). The resultant particle concentration is likely reduced due to the combined limitations of the different nucleation rate and chemical kinetics between the species (Table 3). For example, m-xylene reduced the particle production of α -pinene more effectively than toluene. The reaction rate of m-xylene ($2.31 \times 10^{-11} \text{ cm}^3 \text{ molecule}^{-1} \text{ s}^{-1}$) is significantly faster than toluene ($5.63 \times 10^{-12} \text{ cm}^3 \text{ molecule}^{-1} \text{ s}^{-1}$); therefore, m-xylene is depleting the OH concentration a higher rate compared to toluene (also see Figure 5). Subsequently, less oxidizing agent is available in the chamber to react with α -pinene, which corresponds with our previous findings that a lower initial concentration produces fewer particles. Furthermore, the particle production of m-xylene is less efficient than α -pinene so the resultant particle concentration of a mixture is correspondingly lower.

In Figure 12A, a particle size distribution from each VOC is exhibited. The particles produced in the chamber were less than 10 nm in diameter, with a peak particle size near 1.7 nm. This diameter is consistent with previous works that estimated the critical cluster diameter to be between 1 and 2 nm [Zhang *et al.*, 2004; Zhang *et al.*, 2009; Zhang, 2010]. The oxidation of α -pinene produced the greatest concentration of nanoparticles followed by m-xylene and toluene. In Figure 12B, the particle size distribution as a function of time for 50 ppb of α -pinene is shown. Even after several hours of observations, the particles did not exhibit growth. In the ambient atmosphere, particles typically originate near this size and exhibit growth, although a number of locations have exhibited no particle growth after nucleation [Cheung *et al.*, 2011; Betha *et al.*, 2013; Young *et al.*, 2013; García *et al.*, 2014]. There are several possible reasons

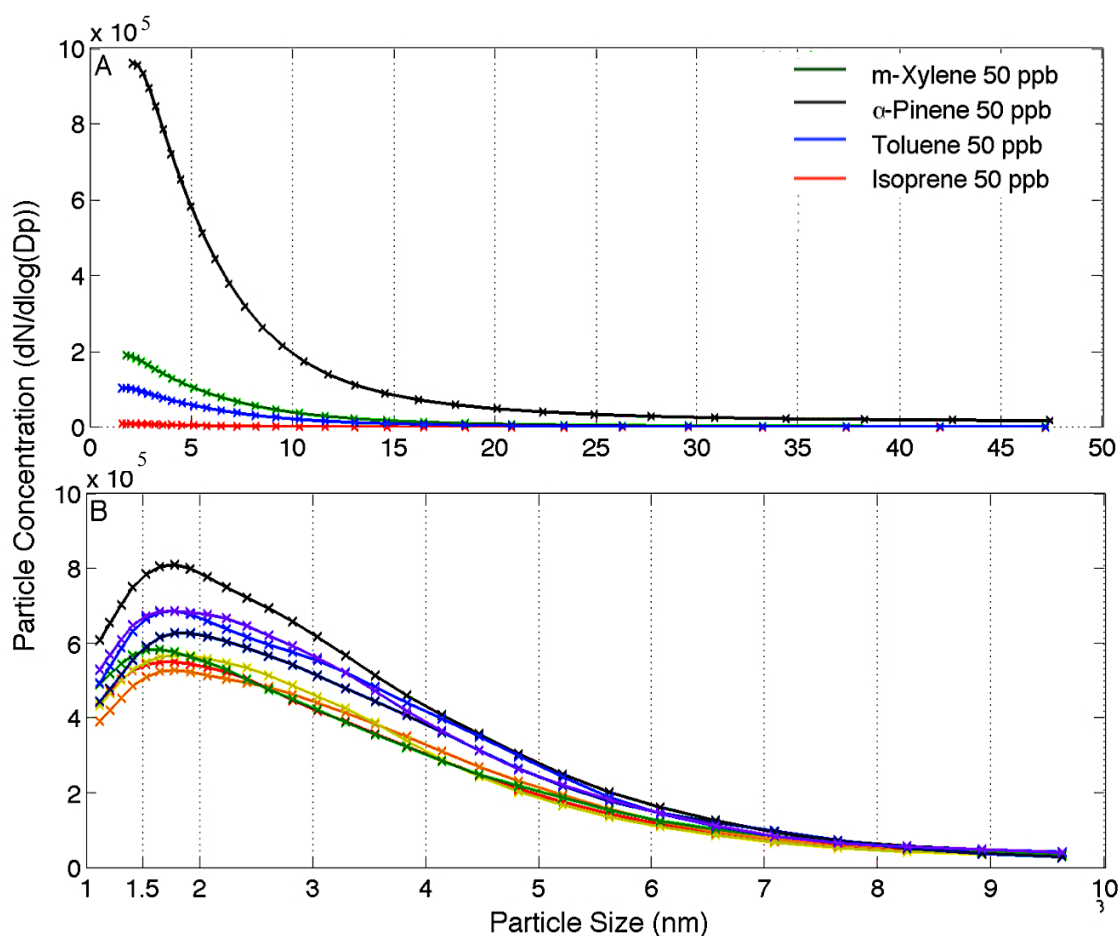


Figure 12. A) The particle size distributions of the new particle formation from α -pinene (black), m-xylene (green), toluene (blue), and isoprene (red) with an initial concentration of 100 ppb, and B) the initial (black) and succeeding particle size distribution measured hourly for seven hours (red, orange, yellow, green, blue, indigo, and violet) of α -pinene with an initial concentration of 50 ppb.

that may explain the absence of particle growth in our system. Many nucleation chamber studies introduce seed aerosols, other gaseous precursors, such as NO_x , SO_2 , or live plants into the chamber, but our system is a pristine environment with no preexisting particles or gases [Stern *et al.*, 1987; Odum *et al.*, 1996; Forstner *et al.*, 1997; Bonn and Moorgat, 2002; Kroll *et al.*, 2006; Sipilä *et al.*, 2010; Wildt *et al.*, 2013]. Our system is

static with virtually no moving air after the initial injection of the VOC, which differs from the ambient atmosphere or chamber experiments with flow tubes or constant injection. *García et al.* [2014] reported that NPF events that exhibited little or no particle growth occurred during reduced wind speeds and low SO₂ concentrations. *Cheung et al.* [2011] reported that these nucleation bursts (i.e. NPF without growth or ‘apples’) occurred when winds blew from industrial point sources, but then due to convective and turbulent winds, the freshly nucleated particles were transported away from the source and dispersed in the ambient air before they could agglomerate and grow.

The oxidation products from by the photooxidation of the various VOCS also govern the growth of nucleation-mode particles. We have demonstrated that not all species produce enough organic acids to effectively generate a NPF event; therefore, it is likely that growth potential is also regulated by the structure and properties of the products. A previous publication demonstrated that the Kelvin effect represents a major limitation for the spontaneous growth of nanoparticles, particularly for freshly formed nucleation-mode particles [*Wang et al.*, 2009; *Zhang et al.*, 2011]. Since the Kelvin barrier is sufficiently elevated, condensation on nanometer-sized particles is unlikely even for organics with low volatility [*Wang et al.*, 2009].

CHAPTER III

WHAT HAPPENS TO AEROSOLS AFTER EMISSION INTO OR FORMATION IN THE ATMOSPHERE? FIELD MEASUREMENTS IN BEIJING OF PARTICULATE MATTER PROPERTIES*

i) Introduction

Three decades of rapid industrialization have made China an economic powerhouse and a geopolitical force to be reckoned with. As the gross domestic product continues to grow, the number of vehicles in China, specifically in Beijing, has dramatically increased due to increased affluence. Beijing alone has added nearly 4 million of its 5 million vehicles since 2000 (Figure 2) [*Ministry of Environmental Protection of China*, 2014]. However, this economic development has resulted in a deterioration of the quality of air, water, land, and health of the population and ecosystems [*WHO et al.*, 2006; *Wang et al.*, 2008; *Yang et al.*, 2013]. As the population continues to migrate to large cities, the demand for transportation and energy has increased correspondingly. Therefore, emissions of NO_x, which are produced by vehicles, and SO₂, which is produced by coal combustion in industrial sources and power plants, have dramatically increased since the 1990s. NO_x and SO₂ negatively influence the ecosystem in many ways, including the formation of acid rain, ozone, and particulate matter and increase respiratory diseases [*Peel et al.*, 2012]. Recent severe

* Portions of this section have been reproduced with permission of the National Academy of Sciences from Guo, S., Hu, M., Zamora, M. L., Peng, J., Shang, D., Zheng, J., ... & Zhang, R. (2014). Elucidating severe urban haze formation in China. *Proceedings of the National Academy of Sciences*, 111(49), 17373-17378. Copyright 2014 National Academy of Sciences, USA..

haze events in China have attracted significant public attention due to the unprecedented pollutant concentration, severely reduced visibility, and severe health effects [*Chang et al.*, 2009; *Zhang et al.*, 2012; *Sun et al.*, 2013; *Zhang et al.*, 2013; *Huang et al.*, 2014]. The annual mean PM_{2.5} concentration at the U.S. Embassy in Beijing in 2013 was 101.85 µg m⁻³ [*U.S. Department of State*, 2013]. This concentration considerably exceeds the WHO's suggested PM_{2.5} concentration level of 10 µg m⁻³ at which cardiopulmonary and lung cancer mortality have been shown to noticeably increase. It has been projected that the 500 million residents living in northern China have lost a total of 2.5 billion years of life expectancy, which is about a 5.5 year reduction per person, due to an increased incidence of cardiorespiratory mortality. Furthermore, the average cancer risk from exposure to inhalable PM toxic metals on haze days is one order of magnitude higher than in developed cities [*Lin et al.*, 2015]. It has also been calculated that hazardous levels of air pollution in China have resulted in the premature death of up 1.2 million citizens annually [*Yang et al.*, 2013] or an estimated 4,000 mortalities per day [*Rohde and Muller*, 2015].

These events have attracted attention from the Chinese government and the scientific community who have endeavored to understand the mechanisms that produce these high concentrations of particulate matter and that allow the haze conditions to persist for several days. As a result, the Chinese government has committed nearly 300 billion U.S.D to address these air quality concerns. In September of 2013, the Chinese Central Government announced that the air quality in China will be “significantly improved” by the end of 2017 and that the PM_{2.5} concentration in all major cities will be

reduced by 10% below 2012 levels [*The Ministry of Environmental Protection*, 2013]. Furthermore, the PM_{2.5} mass concentration in Beijing will be reduced by an additional 15%. Beijing, one of the world's most heavily polluted and populated regions, has become this generation's 'poster child' for poor air quality. The action plan intends to reduce the annual average PM_{2.5} concentrations in Beijing to 60 µg m⁻³ by 2017, which will largely be accomplished by reducing coal consumption, updating the vehicle fleet, and improving the legal system to allow for environmental law enforcement, taxation, and subsidies. The Chinese government has successfully demonstrated a reduction in the SO₂ concentration after the passing of the 11th Five-Year Plan in 2006 (see to Figure 2A).

It has become evident that the mechanism of haze formation in Beijing is distinct from other regions of the world. The transition from clean conditions can be remarkably fast. For example, the mass concentration in Beijing increased by over 769 µg m⁻³ in less than one day on January 22, 2012 [*U.S. Department of State*, 2013]. This rapid PM_{2.5} increase has not been observed in any other region of the world. In addition, the efficiency of NPF events is higher in Beijing when compared to other urban regions, such as Houston, Texas, Los Angeles, California, or Mexico City [*Zhang et al.*, 2015b]. Ambient measurements and receptor model analysis of the annual mean PM_{2.5} mass concentration indicates that the aerosols in Beijing are mainly generated from industrial pollution and secondary inorganic aerosol formation, and negligibly from primary traffic emissions [*Zhang et al.*, 2012; *Sun et al.*, 2013; *Zhang et al.*, 2013; *Huang et al.*, 2014].

The Chinese government has announced that it intends to predict and control the air quality in Beijing. However, recent studies indicate that the air pollution in China is far more complicated than previously realized. It is necessary to have accurate and extensive field measurements so that these complex interactions can be better understood and effectively reproduced in air quality models. Once the air quality can be properly modeled, it will be easier to decide which mitigation strategies would be the most effective. Therefore two field campaigns have been conducted to measure ambient particulate matter and gaseous concentration in Beijing, China between 25 September to 13 November 2013 and between December 2014 and February 2015.

ii) Methodology

All measurements were conducted on the campus of Peking University (PKU, 39°59'21" N, 116°18'25' E) located in northwestern Beijing. The instruments were located in an air conditioned room on the roof of a building about 15 m above ground level. This urban site is located outside the fourth-ring road and is mainly influenced by mobile sources (a major highway is located 200 m east of the measurement site) with no significant stationary sources, which is likely representative of the Beijing urban area. A suite of instruments were deployed to simultaneously measure several gaseous species and aerosol properties, including particle mass concentration, size distribution, chemical composition, temporally and size resolved effective density, and hygroscopicity.

A Tapered Element Oscillating Microbalance (TEOM, 1400a, Thermo, USA.) with a PM_{2.5} cyclone inlet was used to measure the ambient PM_{2.5} mass concentration.

The sampling flow was 16.7 LPM, of which 1 LPM was introduced to the instrument. The TEOM measures the mass collected on a filter by monitoring the corresponding frequency changes of a tapered element. As the mass concentration increased on the exchangeable filter, the tube's natural frequency of oscillation decreased. The mass concentration was determined from the change in the oscillation frequency.

An Aerodyne High-Resolution Time-of-Flight Aerosol Mass Spectrometer (HR-ToF-AMS) was employed to measure the size-resolved chemical compositions of submicron particles. The HR-ToF-AMS operated in 5 minute cycles, including a V-mode to obtain the mass concentrations of non-refractory species such as ammonium, sulfate, nitrate, organics, and chloride, a W-mode to obtain high resolution mass spectral data, and a particle time-of-flight mode to determine size distributions of species measured with the V-mode. The HR-ToF-AMS was calibrated for inlet flow, ionization efficiency, and particle sizing at the beginning, middle, and end of the measurements, as suggested in the protocol. The calibration of ionization efficiency was conducted with size-selected pure ammonium nitrate particles. The HR-ToF-AMS detection limits were determined for each species by passing filtered ambient air through the system and measuring the corresponding species signals for three five-minute intervals. The detection limit was defined as three times the standard deviations of the observed signals. The detection limits of sulfate, nitrate, ammonium, chloride, and organics were determined to be 0.008, 0.004, 0.026, 0.004, and 0.033 $\mu\text{g m}^{-3}$, respectively. Using known properties (i.e. the oxygen/carbon ratio, O/C) of the measured organic aerosols (OA), the OA component can be further decomposed into hydrocarbon-like organic

aerosols (HOA, O/C = 0.04 - 0.13), semi-volatile oxygenated organic aerosols (SV-OOA, O/C = 0.27 - 0.48) factors, and low volatility oxygenated organic aerosols (LV-OOA, O/C = 0.59). HOA is frequently employed as a surrogate of primary organic aerosols (POA), whereas, the sum of the concentrations of SV-OOA and LV-OOA is the surrogate SOA [*Sun et al.*, 2012].

Ambient aerosols were sampled at a rate of 1 LPM through a 3 m long thermally insulated 3/8" stainless steel tube and then passed through a series of Nafion driers (PD-070-18T-24SS, Perma Pure, Inc.) to reduce the relative humidity of the aerosols to less than 10%. A scanning mobility particle sizer (SMPS) and a nano-SMPS were used to concurrently measure the number size distribution of particles between 3 and 500 nm in the ambient air. In the SMPS/nano-SMPS configuration, polydisperse aerosols were brought to charge equilibrium and passed through the DMA and CPC to determine the particle size and concentration. The sheath flow rate was maintained at 3 LPM for the DMA and 20 LPM for nano-DMA. The particle size was calibrated with mono-disperse polystyrene latex spheres (PSL, Duke Scientific, Palo Alto, California, USA.) with nominal diameters of 100 – 700 nm. To determine the size resolved effective density, the flow was then passed through an Aerosol Particle Mass analyzer (APM, model 3600, Kanomax Inc., Japan). Effective density is defined as the measured mass over the volume if the particle was assumed to be a sphere determined by the measured particle size; therefore compounds with the same mass but different shapes may have extremely different effective densities. The effective densities for five-particle sizes were obtained hourly. Since the mobility diameter corresponds to a unique voltage, if the applied

voltage and effective density of PSL are known, the effective density of the sample aerosols can be calculated by the following equation,

$$\rho_{eff} = V_{APM} / V_{APM,PSL} \times \rho_{PSL}$$

where V_{APM} and $V_{APM,PSL}$ are the peak APM voltages corresponding to the masses of sample and PSL particles, respectively. The material density of the PSL particles is 1.054 g cm^{-3} . Each effective density distribution scans from 0.1 to 2.2 g cm^{-3} . Effective density peaks at 1.76 , 1.78 , and 1.73 g cm^{-3} corresponding to ammonium sulfate, ammonium bisulfate, and ammonium nitrate. The effective density of organic aerosols can vary significantly due to the numerous compounds in this category, the different emission sources, and the distinct structures of the compounds. *Turpin and Lim* [2001] reported that SOA from the oxidation of aromatics and alkanes had a density between 1.20 and 1.40 g cm^{-3} , whereas *Kostenidou et al.* [2007] determined SOA density can vary between 1.40 and 1.65 g cm^{-3} . The effective densities of fresh black carbon, mineral dust, and sea salt are $0.1 - 0.6$, 2.65 , and 2.2 g cm^{-3} , respectively [*Geller et al.*, 2006; *Khalizov et al.*, 2009b]. This methodology has been utilized and discussed previously [*Levy et al.*, 2013, 2014a].

A Hygroscopic Tandem DMA (HTDMA) was used to determine the size resolved hygroscopic growth factor (HGF) distributions. During hygroscopicity measurements, a monodisperse aerosol flow of known size was produced by the first DMA and exposed to relative humidity near 90% in a multi-tube Nafion drier/humidifier (PD-070-18T-24SS, Perma Pure, Inc.). The particles were then passed through a second DMA to measure the change in the mobility diameter compared to the initial

monodispersed flow. The growth factor is determined by the ratio of the initial dry particle diameter (D_0) and the processed diameter (D_p). A HGF of unity indicates no change in particle size after exposure to 90% relative humidity, a value less than one indicates a decrease in mobility particle size, and a value greater than one indicates an increase in size. Pure ammonium sulfate has a HGF of 1.70 at 90% RH [Wise *et al.*, 2003]. Organics exhibit lower HGFs, ranging from 1.08 to 1.17 at 90% RH, with POA occurring at the lower values and the more oxidized secondary organic aerosols in the upper values [Meier *et al.*, 2009]. The HGF for both black carbon and mineral dusts is typically near 1.0 due to their hydrophobic properties.

The hygroscopicity was also quantified by using the parameter kappa (κ). Kappa is derived using the following formula:

$$\kappa = \frac{v\rho_d}{\rho_w} \frac{M_w}{M_d} = \sum_i \varepsilon_i \kappa_i$$

where M , ρ , v , and ε , are the molecular weight, molecular densities, van Hoff factor, and volume fraction of the component in the aerosols mass, respectively. Using the volume-weighted average fraction determined by the AMS measurement and an ε_i of 0.0, 0.09, 0.48, 0.58, 0.55, and 0.246 for black carbon, organic aerosols, SO_4 , NO_3 , NH_4 , and Cl, respectively, the chemical composition derived kappa was calculated.

The concentration of nitric oxide (NO) and nitrogen dioxide (NO_2) were determined using a chemiluminescent NO- NO_x analyzer (Thermo Inc., Model 42i). NO and O_3 reacted and produced a luminescence that is linearly proportional to the NO concentration. The concentrations of NO_x was determined by passing the sample through a reducing molybdenum NO_2 -to-NO converter, and the NO_2 concentration was

calculated by subtracting the measured NO concentration from the total. The ozone concentration was determined using a Thermo 49i (Thermo Inc., Model 49i). The O₃ concentration was determined by the amount of UV light absorption at 254 nm. The SO₂ concentration was measured by a Thermo 43i analyzer (Thermo Inc., Model 43i-TLE). SO₂ molecules were excited to a higher energy state by the absorption of UV light, which decayed to a lower energy level and released a photon. The SO₂ concentration was proportional to the intensity of UV light observed.

A commercial PTR-MS (Ionicon Analytik, Innsbruck, Austria) was used to measure ambient VOCs. The detailed operation and calibration procedures for the instrument have been described previously [Zhang *et al.*, 2015b]. Background signals were measured by passing ambient air through a platinum coated-wool trap (Shimadzu Inc., Japan) heated to 350 °C for 30 cycles after every 300 cycles of ambient measurements. The PTR-MS was calibrated by cylinder gas standards (provided by Apel-Riemer Environmental Inc., USA). The system was operated in multiple-ion mode with 24 simultaneous masses measured including H₃O⁺, benzene (*m/z* 79), toluene (*m/z* 93), styrene (*m/z* 105), C8 aromatics (*m/z* 107), C9 aromatics (*m/z* 121), methanol (*m/z* 33), acetaldehyde (*m/z* 45), acetone (*m/z* 59), methyl vinyl ketone / methacrolein (*m/z* 71), methyl ethyl ketone (*m/z* 73), isoprene (*m/z* 69), and acetonitrile (*m/z* 42).

iii) Results and Discussion

a) Beijing 2013

The PM_{2.5} mass concentration, number size distribution, mean diameter, and total number concentration during the period of 25 September to 13 November 2013 are exhibited in Figure 13. We further elucidated the processes regulating the particle number and mass concentrations by examining in detail the PM_{2.5} cycle that occurred between 25 and 29 September 2013. The temporal evolutions of particle number size distribution and mean diameter (white dashed curve) are shown in Figure 14A, and the PM_{2.5} mass concentration (black solid line), mean diameter (purple dashed line), and PM₁ (particulate matter smaller than 1.0 μm) chemical composition are shown in Figure 14B. The development of the pollution episode was comprised of two distinct secondary aerosol formation processes: NPF and growth. The measurements exhibited a clear periodic cycle (Figure 13A) with the PM_{2.5} concentration less than 20 μg m⁻³ during the initial clean phase, continuous particle mass growth of 50 - 110 μg m⁻³ occurring during the transition period, and a PM_{2.5} concentration exceeding several hundred μg m⁻³ (polluted) within 2 - 4 days. It is interesting to observe how rapidly the air quality could shift from being extremely polluted to clean. The PM_{2.5} mass concentration frequently decreased by hundreds of μg m⁻³ at the end of the haze events in a span of a few hours. The mean particle diameter (Figure 13C) displayed a similar cycle as that of the mass concentration: continuously increasing diameter from the clean (20 nm) to polluted (200 nm) period, with 40 – 60 nm daily growth during the transition period. The measured particle size distributions (Figure 13B) exhibited high number concentrations of small

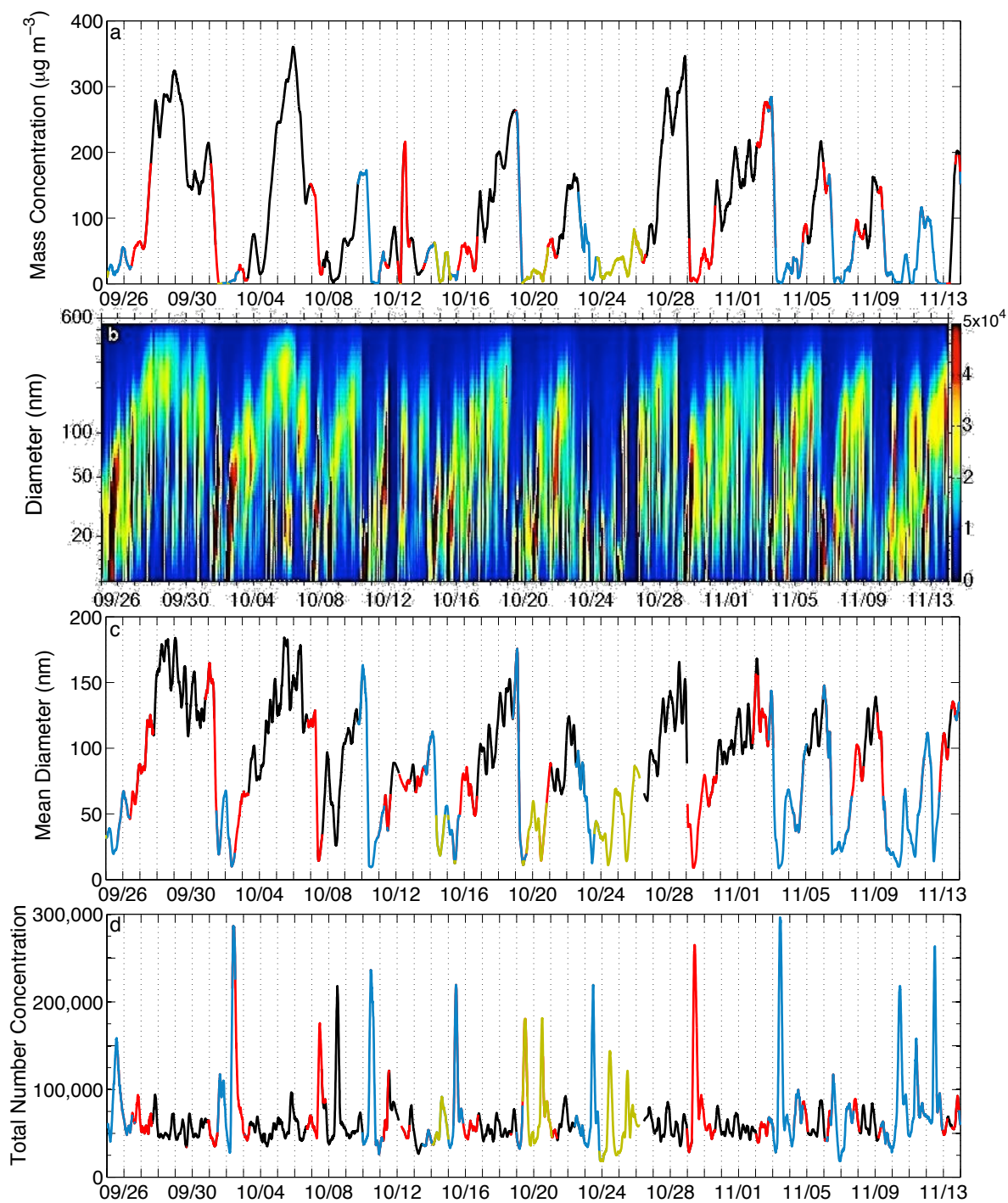


Figure 13. Temporal evolutions of A) $PM_{2.5}$ mass concentration, B) number size distribution, C) mean diameter, and D) total number concentration during the period of 25 September to 13 November 2013. The colors in A, C, and D represents the air mass originating from the south (black), northwest (blue and red), and northeast (yellow). Reprinted with permission of the National Academy of Sciences from Guo, et al., (2014). Elucidating severe urban haze formation in China. *Proceedings of the National Academy of Sciences*, 111(49), 17373-17378. Copyright 2014 National Academy of Sciences, USA.

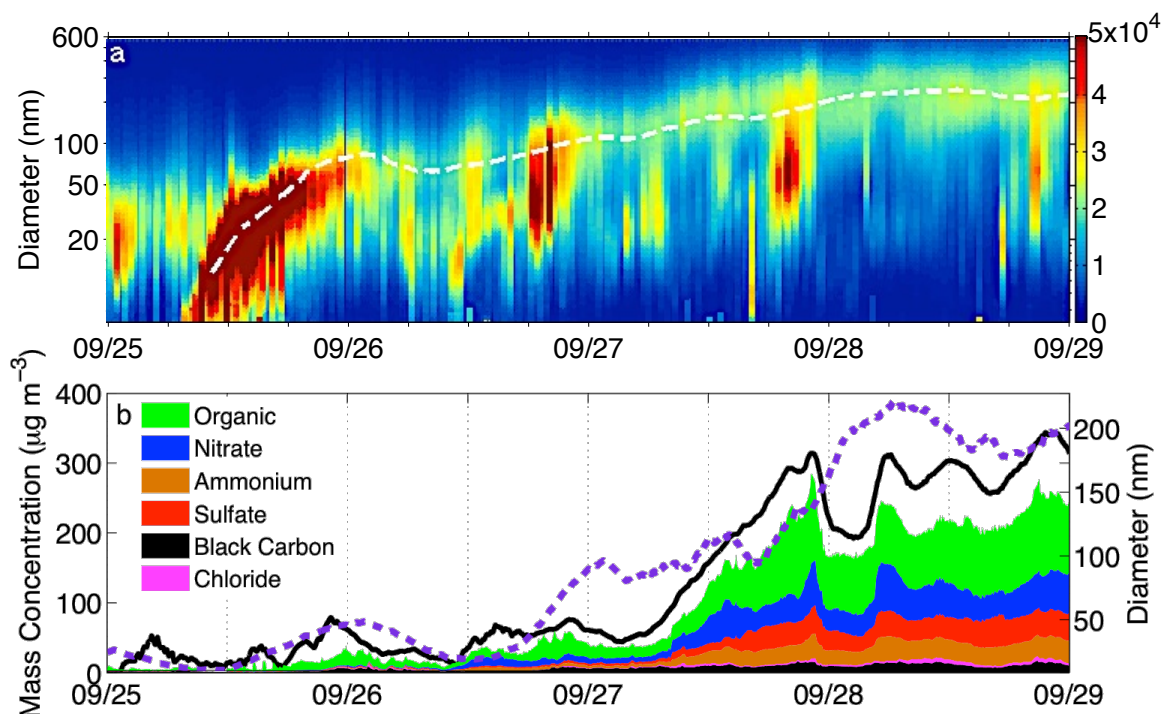


Figure 14. A) Temporal evolutions of particle number size distribution and mean diameter (white dashed curve) and B) $\text{PM}_{2.5}$ mass concentration (black solid line), mean diameter (purple dashed line), and PM_{10} (particulate matter smaller than $1.0 \mu\text{m}$) chemical composition between 25-28 September 2013. Reprinted with permission of the National Academy of Sciences from Guo, et al., (2014). Elucidating severe urban haze formation in China. *Proceedings of the National Academy of Sciences*, 111(49), 17373-17378. Copyright 2014 National Academy of Sciences, USA.

particles ($< 20 \text{ nm}$) during the clean period, but lower particle number concentrations and larger particle diameters during the polluted period. The total particle number concentration exceeded $200,000 \text{ cm}^{-3}$ during the clean period, but as the pollution event developed, the total number decreased slightly and remained at about $80,000 \text{ cm}^{-3}$ (Figure 13D). The occurrence of high concentrations of nano-sized particles during the clean period is characteristic of aerosol nucleation (Figure 13D). Interestingly, there is a noticeable absence of new particle formation as the $\text{PM}_{2.5}$ mass concentration increased,

indicating the suppression of nucleation by pre-existing background particles. Favorable conditions for NPF events often include low pre-existing aerosol concentrations because aerosol surfaces easily act as a sink for condensable vapors. During the transition from the clean to polluted periods, the evolution of the nucleation mode particles was clearly detected by the changes in the mean particle size over the course of three days (Figures 13 and 14), which increased from about 10 to 200 nm. Periodically high concentrations of 30 - 100 nm particles were observed during the morning (6:00 - 9:00) and evening (18:00 - 21:00) rush hours. The timing and size of the elevated aerosols are indicative of primary particle emissions originating from local transportation (Figure 14A). Although the local traffic emissions were clearly discernible by the transiently elevated number concentrations (Figure 14), the primary particles did not appear to appreciably alter the particle growth process. The minor fluctuations in the mass concentration can largely be explained by variations in the wind speed and direction. For example, the noticeable decrease in the mass concentration during the morning hours of 9/26, 9/27, and 9/28 coincided with an increasing wind speed by 1.8, 0.5, and 1.8 m s^{-1} , respectively.

The shaded regions in Figure 14B represent the mass concentrations of aerosol constituents determined by AMS. The aerosol composition was dominantly composed of organic aerosols (44%), followed by nitrates (22%), sulfate (17%), ammonium (15%), and chloride (2%), which is comparable to many other large urban centers in the world [Jimenez *et al.*, 2009; Zhang *et al.*, 2011; Guo *et al.*, 2012; Guo *et al.*, 2013]. Similar particle size and mass evolutions to those shown during the clean period (i.e., from 9:00 to 24:00 on 9/25) have also been commonly observed under diverse environmental

conditions, including in pristine areas and urban centers. Typically, new particle formation and growth cycles occur daily [Boy *et al.*, 2004], but few other locations exhibit the sustained and efficient particle growth as those displayed during the transition and polluted periods in Beijing (i.e., between 9/26 and 9/29 in Figure 13A, B). The chemical composition measurements from the 25 - 29 September episode revealed continuously increasing organic, sulfate, and nitrate aerosols, which was closely associated with the increasing PM_{2.5} mass concentration and mean particle size (Figure 15). The organic mass fraction dominated in the clean period, and remained the largest throughout the haze event, but decreased from 77 to 42% from the clean to polluted periods (Figure 15A). Therefore, organic aerosols were likely responsible for NPF during the clean period. Additional AMS-positive matrix factor analysis revealed the organic dominant composition was comprised of both primary and secondary organic aerosols and that the SOA fraction was the largest throughout the episode. The POA

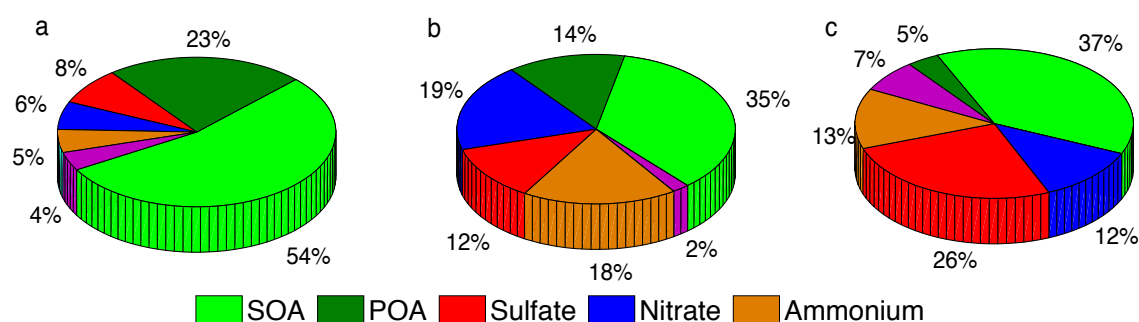


Figure 15. A-C) Chemical composition for 80, 100, and 240 nm particles from the corresponding particle mean diameter during the clean ($12 \mu\text{g m}^{-3}$), transition ($167 \mu\text{g m}^{-3}$), and polluted periods ($288 \mu\text{g m}^{-3}$), respectively. Reprinted with permission of the National Academy of Sciences from Guo, *et al.*, (2014). Elucidating severe urban haze formation in China. *Proceedings of the National Academy of Sciences*, 111(49), 17373-17378. Copyright 2014 National Academy of Sciences, USA.

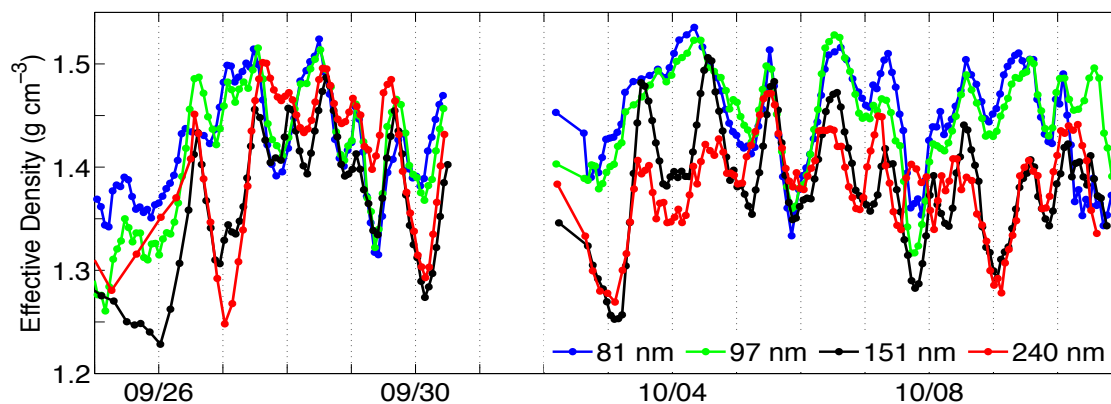


Figure 16. The weighted average effective density of 81 (blue), 97 (green), 151 (black), and 240 nm (red) particles during the 2013 Beijing field campaign.

mass fraction decreased considerably during the transition and polluted periods, indicating small contributions of primary aerosol emissions to the development of haze events. The contributions of sulfate and nitrate to the particle mass concentration increased, with the mass fractions of 8 and 6% during the clean period and 26 and 12% during the polluted period, respectively.

The variation in the particle chemical composition was also reflected in the measured effective density and hygroscopicity. The weighted average effective density for 81, 97, 151, and 240 nm particles are exhibited in Figure 16, and the hygroscopic growth distributions of 46, 81, 97, and 151 nm particles are shown in Figure 17. The 81 and 240 nm particles exhibited the least (1.45 to 1.53 g cm⁻³ on an average day) and greatest (1.27 to 1.45 g cm⁻³ on average) amount of diurnal variability, suggesting that the larger particles exhibited more efficient growth or greater variability in the composition of the aerosols throughout the day. The lowest effective density was observed between 5 and 7 a.m. for all particle sizes; however, the larger particles

exhibited a much lower effective density overall between 6 p.m. and 7 a.m., likely due to the increased concentration of black carbon. Previous observations with a similar methodology have demonstrated that black carbon is most ubiquitous near 151 and 240 nm particles [Levy *et al.*, 2014a]. Diesel trucks, which emit copious amounts of black carbon, are only permitted in the city between 9 p.m. and 7 a.m. The effective densities increased from the morning to the early afternoon, likely due to the increase in the particle-phase oxidized organic and sulfates components. The hygroscopic distributions of 46, 81, 97, and 151 nm particles determined by a HTDMA is presented in Figure 17. The hygroscopicity measurements indicate that the HGF distributions were dominantly unimodal, indicating an internally mixed aerosol composition or one dominant aerosol source. The pollution cycle was most evident in the hygroscopicity of the larger particles (i.e. 151 nm): the peak HGF was near 1.1 during the clean phase, between 1.3 and 1.6 during the heavily polluted phase, and rapidly increased from 1.1 to 1.8 during the transition period on 27 September (Figure 17D). The hygroscopicity of the 46 nm was less influenced by the variations in the mass concentration since the mean diameter of the particles during the haze events was larger than 50 nm. Diurnally, the highest HGFs were observed during the early afternoon, likely due to the increased gas-to-particle conversion of hygroscopic components, such as nitrate and sulfate, due to enhanced oxidation during the afternoon. The periodic pulses of HGFs near 1.05 observed during the morning (6 a.m. – 9 a.m.) and evening (6 p.m. – 9 p.m.) rush hours are indicative of primary particle emissions originating from local transportation. However, during the haze event (i.e. 28 September) the transient mass of hydrophobic aerosols was not

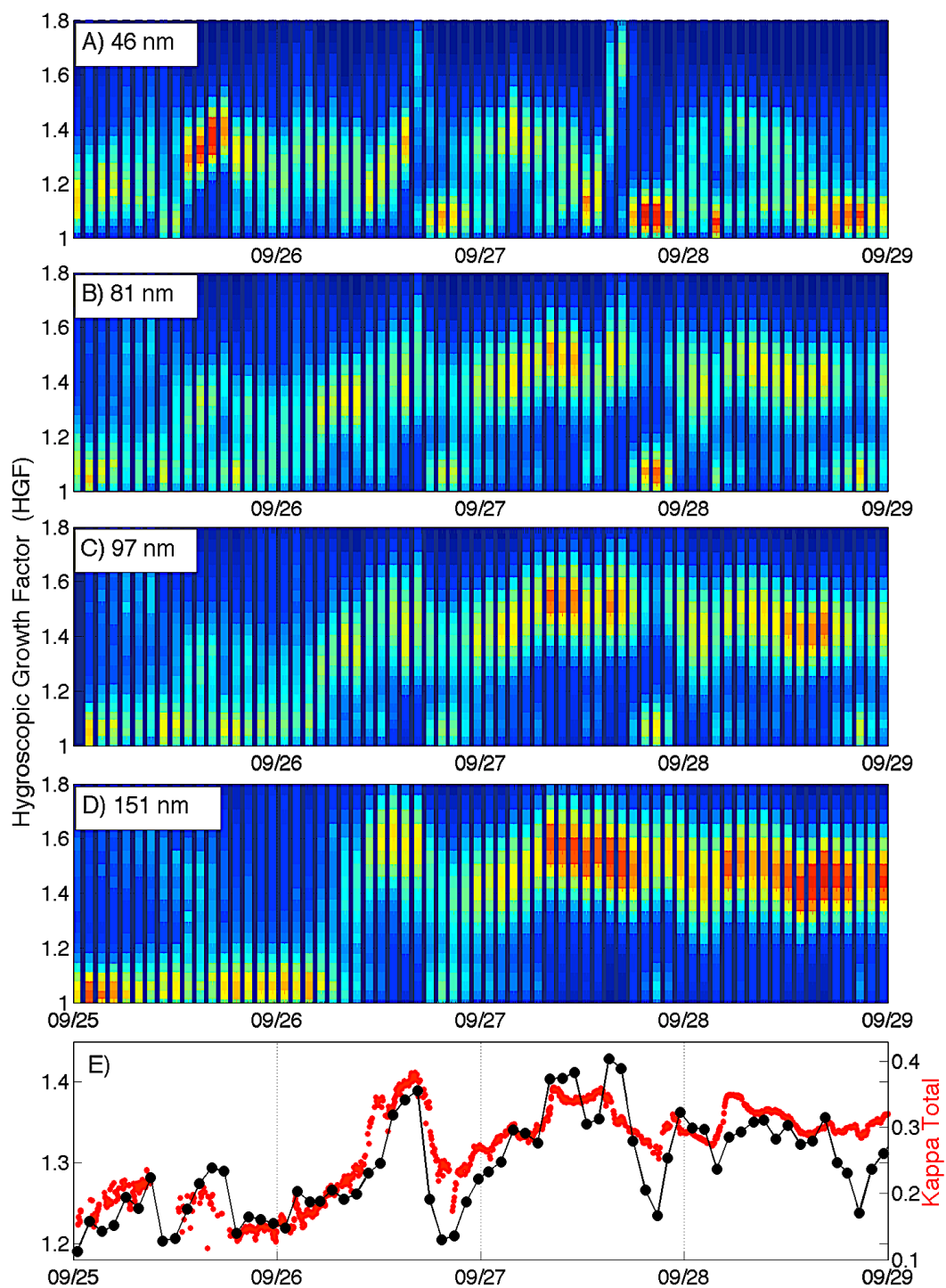


Figure 17. The hygroscopic distributions of A) 46, B) 81, C) 97, and D) 151 nm particles determined by a HTDMA. The intensity of the colors correlate to the concentration of particles: the more red, the higher the relative concentration. E) A comparison of the weighted hygroscopic growth factor (black) and kappa (red) between 25 and 29 September.

discernible in the hygroscopic distributions suggesting that the primary aerosols were insignificant to the overall mass concentration. The comparison of the hygroscopicity derived from the HTDMA (hygroscopic growth factors) and the chemical composition (κ) is shown in Figure 17E. Both approaches exhibit similar trends diurnally and throughout the pollution cycle.

During the clean period, the lower average effective density and the unimodal hygroscopic distributions were both indicative of an organic-dominant composition [Turpin and Lim, 2001; Kostenidou et al., 2007; Swietlicki et al., 2008; Khalizov et al., 2009b; Massoli et al., 2009; Meier et al., 2009]. In addition, the increased hygroscopicity and effective density during the transition and polluted periods correspond to the formation of an internally mixed secondary organic and inorganic species due to the increasing contributions from sulfate and nitrate. During the transition and polluted periods, the average HGFs were 1.50 and 1.53, and the effective densities were 1.48 and 1.51 g cm⁻³, respectively. There was also a noticeable absence of the primary aerosol constituents from the hygroscopicity and effective density measurements during the transition and polluted periods, including black carbon, POA, and mineral dusts. Hence, our analysis of the aerosol chemical compositions suggests that SOA are principally responsible for producing the nucleation mode particles and SOA and inorganic salts contribute jointly to particle growth, further confirming that the secondary formation dominates the development of PM_{2.5} pollution episodes in Beijing, with small contribution from primary particle emissions.

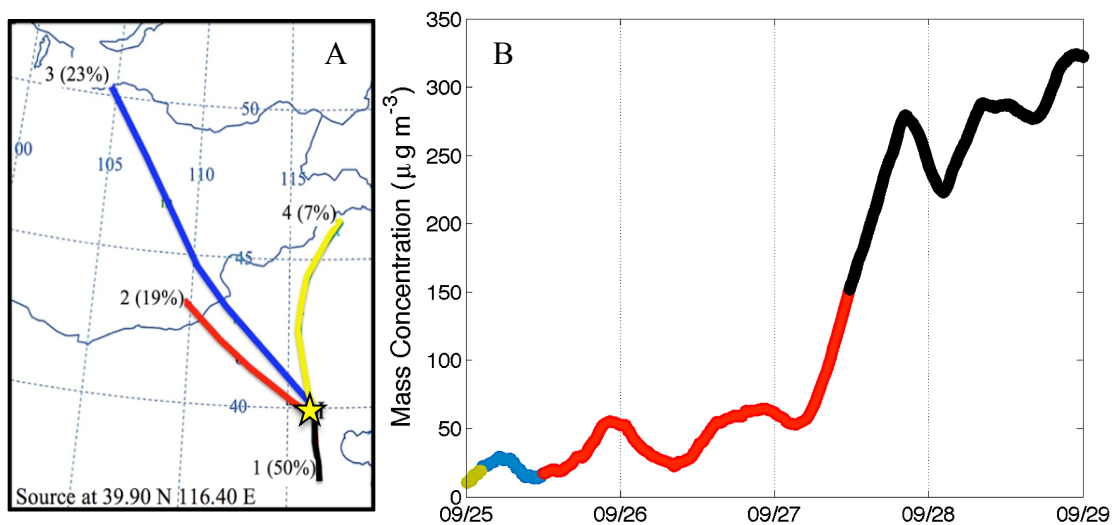


Figure 18. A) Map demonstrating the location of the sampling site and back-trajectories using the NOAA-HYSPLIT model to illustrate the frequency of synoptic flow patterns observed during the field campaign. B) The predominant wind direction throughout a haze event. Reprinted with permission of the National Academy of Sciences from Guo, et al., (2014). Elucidating severe urban haze formation in China. *Proceedings of the National Academy of Sciences*, 111(49), 17373-17378. Copyright 2014 National Academy of Sciences, USA.

Since measurements at a fixed site are affected by local emissions, transport, and chemistry, we analyzed the evolution of the particle size, mass, number concentration, chemical composition, and meteorological parameters, such as wind direction and speed, back-trajectories, and mixing layer depths, in order to decouple the various processes. The back-trajectories were determined by utilizing the National Oceanic and Atmospheric Administration's (NOAA) hybrid single-particle Lagrangian integrated trajectory (HYSPLIT) model. During the observation period, southerly winds were most prevalent (black, 50%), followed by winds from the northwest (blue and red, 42%) and northeast (yellow, 7%, Figure 14A). The stronger northwesterly (i.e. blue) and northeasterly winds typically occurred during the clean periods (Figure 14B), carrying

unpolluted air masses from the less populated mountainous areas. During the transition and polluted periods, the wind decreased and shifted from northerly to southerly winds, resulting in the transport of air masses from the more populated southern industrial regions and stagnant conditions that trapped the local gaseous pollutants from city traffic. The average mass concentrations were 35 and 114 $\mu\text{g m}^{-3}$ during the northerly and southerly wind conditions, respectively (Figure 14B). It is clear that the meteorological conditions are a critical parameter in the cycling of pollution episodes in Beijing. During the most polluted period, the movement of the air mass was less than 25 km day^{-1} (the Beijing metropolis is 16,801 km^2) [Zhang *et al.*, 2015b], suggesting that during the severe $\text{PM}_{2.5}$ episodes regional transport is negligible.

The presence of particle-phase OA, sulfate, and nitrate was largely attributable to the conversion of gaseous VOCs, SO_2 , and NO_x , respectively. Photochemical oxidation and multi-phase reactions of VOCs, SO_2 , and NO_x in the atmosphere lead to the formation of less or non-volatile species. Our gaseous measurements show highly elevated concentrations of these species during pollution episodes (Figure 19). For example, during the pollution episodes the peak SO_2 and NO_x concentrations exceeded 40 and 200 ppb, respectively, and the aromatic VOCs (i.e. xylenes and toluene) represented the most abundant type of VOCs, with peak xylene concentration exceeding 10 ppb. The peak isoprene concentration was typically around 1-2 ppb. For reference, the annual SO_2 concentration in Houston, Texas, Los Angeles, California, Mexico City, Mexico, and Beijing, China were 0.35, 0.37, 2.50, and 7.8 ppb [Zhang *et al.*, 2015b]. The NO_x and SO_2 concentrations were the lowest in the presence of northerly and

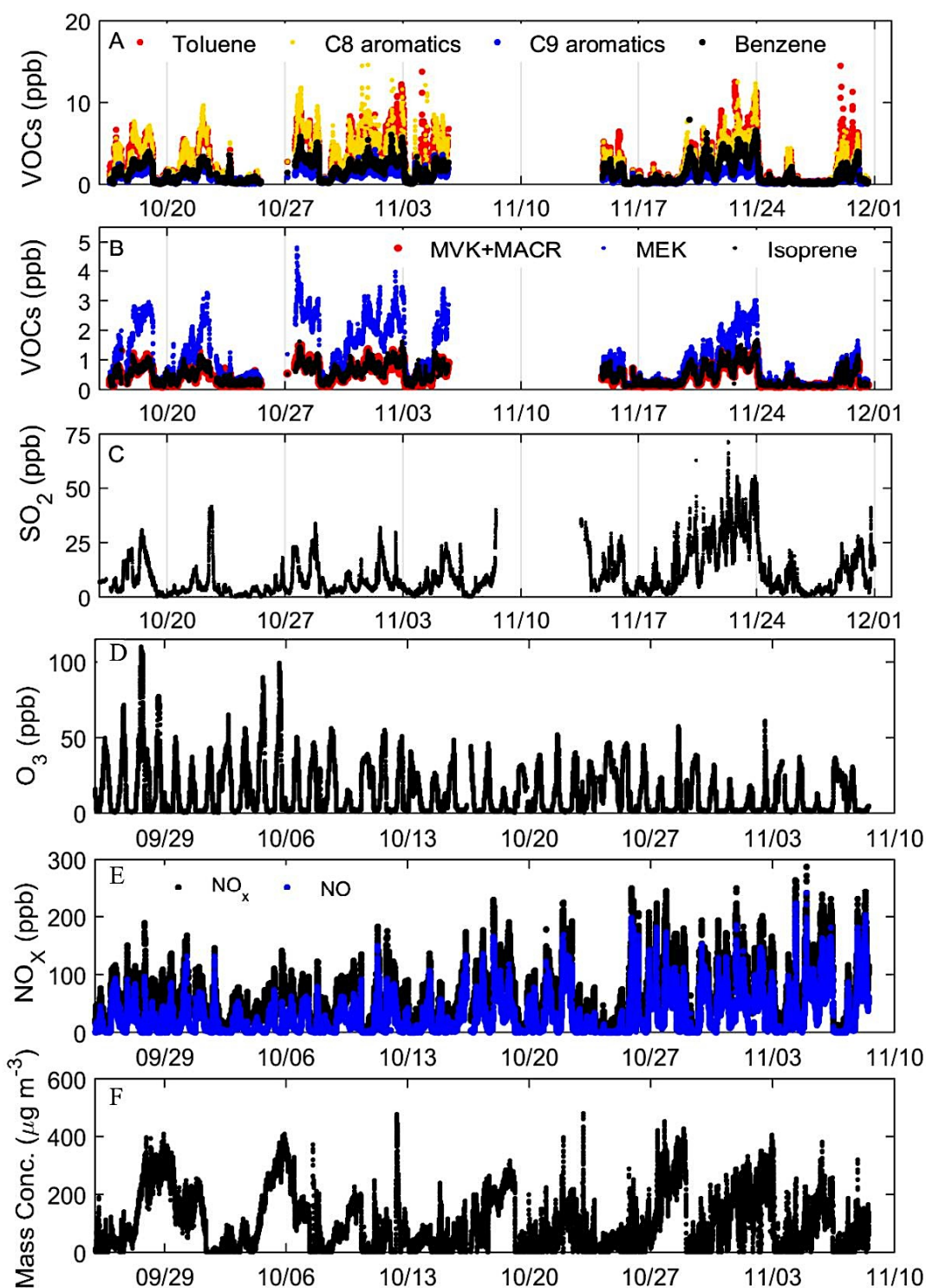


Figure 19. Concentrations (ppb) of A) aromatic VOCs, B) biogenic VOCs, and C) SO₂ measured between 16 October and 31 November (i.e. the period when these instruments were online) and of D) ozone, E) biogenic VOCs, and F) PM_{2.5} mass concentration (µg m⁻³) measured between 25 September and 10 November 2013.

northeasterly winds (i.e. the clean period), but increased considerably with northwesterly and southerly winds (i.e. the transition and polluted periods). The average ozone concentration was 17 ppb during the entire observational period, but higher concentrations were observed at the beginning of the campaign than near the end, likely reflecting a seasonal variation. The ozone concentration was noticeably elevated for the PM_{2.5} events on 27 September (110 ppb) and 5 October (99 ppb), indicating the efficient photochemical activity during the transition and polluted periods. While traffic emissions represent the dominant sources of VOCs and NO_x in Beijing, industrial emissions contribute mainly to the SO₂ concentration. Considering the relatively stagnant air mass during the pollution periods and the atmospheric lifetimes of aromatics, SO₂, and NO_x (about 0.5 - 2.5 days, 9.6 days, and 1.0 days, respectively), the SO₂ level in Beijing was likely due to a large regional contribution from the southern industrial area, and the VOC and NO_x concentrations were dominated by local traffic emissions. Furthermore, the AMS measurements reveal a non-negligible mass fraction of ammonium during the transition and polluted periods, which is also likely linked to automobile emissions.

In order to further confirm that the high PM_{2.5} concentration was predominantly produced locally and not due to transport, analyses of the AOD and the relationship between SOA formation and odd-oxygen (the combined concentrations of O₃ and NO₂, O_x) have been conducted (Figure 20). The AOD is a measure of the extinction of the solar beam by particles in the atmosphere i.e. (dust, smoke, pollution). It is a dimensionless number that is directly related to the number of aerosols in the vertical

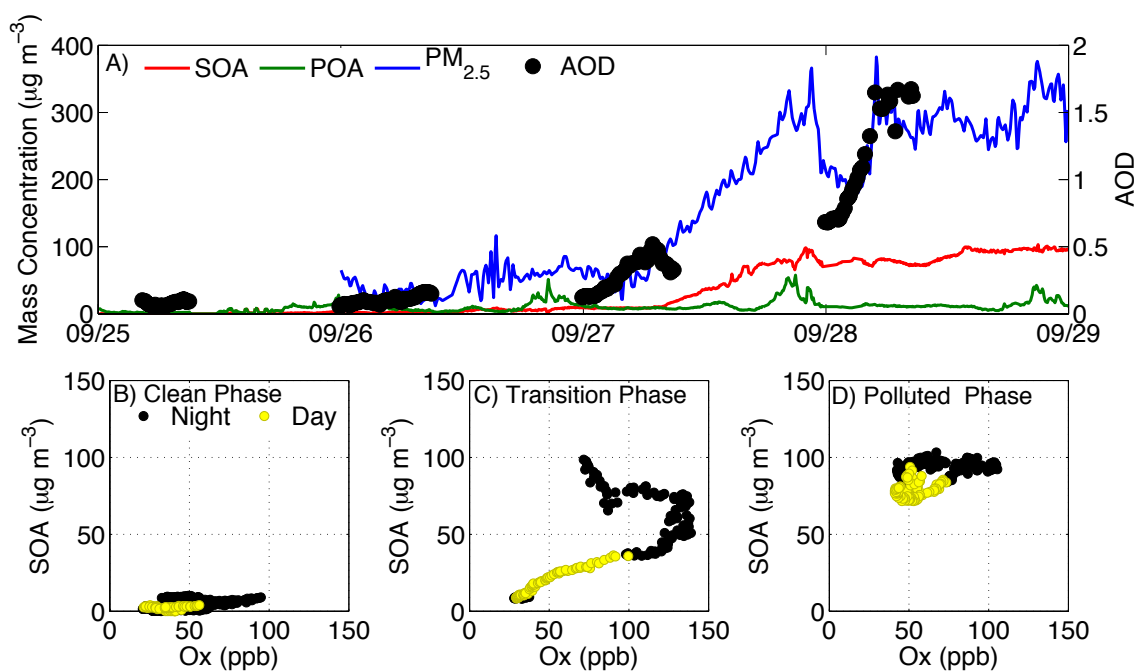


Figure 20. A) The mass concentrations of $\text{PM}_{2.5}$ (blue), secondary organic aerosols (red), and primary organic aerosols (green), and the aerosols optical depth (black). B-D) Scatterplots of odd-oxygen ($\text{O}_3 + \text{NO}_2$, O_x) and secondary organic aerosols during the clean, transition, and polluted phases.

atmospheric column over the observation location. A value, such as 0.01, indicates an extremely clean atmosphere, and hazy conditions in the U.S. may be near 0.40. The average AOD in the U.S. is between 0.1 and 0.15 [ESRL, 2015]. The AOD values were obtained through the Aerosol Robotic Network (AERONET) site on the roof of the Institute of Atmospheric Physics building in Beijing (39.97689° N , $116.38137^\circ \text{ E}$) [AERONET, 2015]. An analysis of the AOD can be instructive because it reveals the mass concentration in the entire atmospheric column and can be used to decouple vertical and horizontal transport. The planetary boundary layer (PBL) is the lowest level of the atmosphere that determines the volume of air that pollutants will be mixed into on short time scales. Typically the PBL is low (on the order of hundreds of meters high)

overnight, but as the sun rises in the morning, the ground and air are heated, resulting in ascending air. As the air rises, the mixing layer height increases, therefore allowing emitted pollutants to mix into a larger volume (on the order of a few thousands of meters high). As the sun's intensity begins to wane in the afternoon, the mixing region begins to decrease, which compresses the pollutants into a smaller volume. While a majority of the $PM_{2.5}$ mass concentration will be in the mixed layer, it is possible that aerosols produced in an adjacent city could be transported into the atmospheric column over the city in the residual layer (the middle portion of the nocturnal atmospheric boundary layer containing pollutants remaining from the mixed layer of the previous day) when the PBL is low overnight. In this scenario, as the PBL height increases due to daytime heating, the transported aerosols would mix downward and increase the mass concentration at the surface; however, the mass concentration in the total atmospheric column would not exhibit significant fluctuations because the aerosols are not being created but simply being transported between layers. Conversely, if aerosols are brought into the region by horizontal transport or are produced locally, a dramatic increase in the total column would be observed. This would be particularly evident in the Beijing case where the mass concentration can increase by several hundred micrograms in a short period of time. Figure 20A shows that the AOD increased simultaneously as the $PM_{2.5}$ and SOA mass concentrations increase, indicating that the aerosols were not mixed in from the upper troposphere and vertical transport was not a significant source.

A scatterplot of the SOA and O_x mass concentrations can be used to identify if horizontal transport is a major source of aerosols in the observed region. Since SOA are

formed as the result of gas-to-particle partitioning of low-volatility compounds and O_x is formed as a by-product of VOC oxidation, the high formation rate for both species is high during periods of intense photochemistry. It has previously been demonstrated that odd-oxygen and SOA are strongly correlated in air masses where both species were formed on similar timescales and poorly correlated when their formation timescales or formation location differed greatly [Wood *et al.*, 2010]. Therefore if the correlation is strongly positive, then horizontal transport must not be a significant SOA mass concentrations source. The scatterplot from the daytime during the clean phase is weakly positive, which indicates that the aerosols were locally produced; however, the aerosol production rate was quite low. The scatterplot from the daytime and early evening during the transition period is positive ($R^2 = 0.97$) indicating that the aerosols were formed locally and produced recently. It possible for an influx of aerosols to occur simultaneously as the rise in photochemical activity during the morning and early afternoon, thus mimicking a rise in SOA formation; however, this correlation was present in other haze cycles and the large scale meteorological patterns did not recommend this scenario. The poor correlation of SOA with O_x observed during the polluted phase ($R^2 = 0.21$), indicates large differences in the timescales of production between SOA and O_x , i.e. the aerosols were not formed on that day, which corresponds with the high concentration of aerosol that were trapped due to the stagnant conditions. The clustering of points observed during the afternoons in the clean and polluted phases was likely caused by a combination of several factors such as entrainment of air with

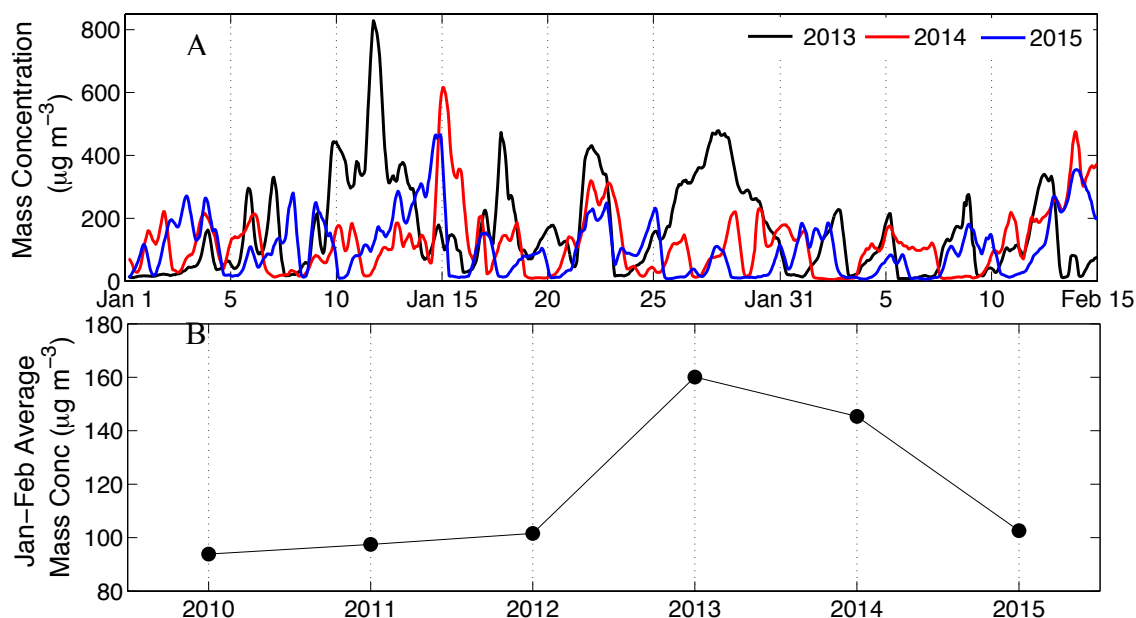


Figure 21. Comparisons of the winter PM_{2.5} concentration between 2010 and 2015 in Beijing, China measured at the U.S. Embassy [U.S. Department of State, 2013].

variable OOA and O_x concentrations due to changes in the PBL height, changes in the production rates of SOA and O_x, or dry deposition of SV-OOA [Wood *et al.*, 2010].

b) Beijing 2015

During the winter of 2014-2015, we analyzed the size-resolved effective density, PM_{2.5} concentration, particle size distributions, and chemical composition of ambient aerosols with a focus on understanding the winter haze formation mechanism and elucidating how the formation processes compare between seasons. The haze events have historically been most severe during the wintertime in China. In Figure 21A, the 2013, 2014, and 2015 PM_{2.5} mass concentrations in January and February are presented. The three years appear to exhibit the same general trends and concentrations, and all

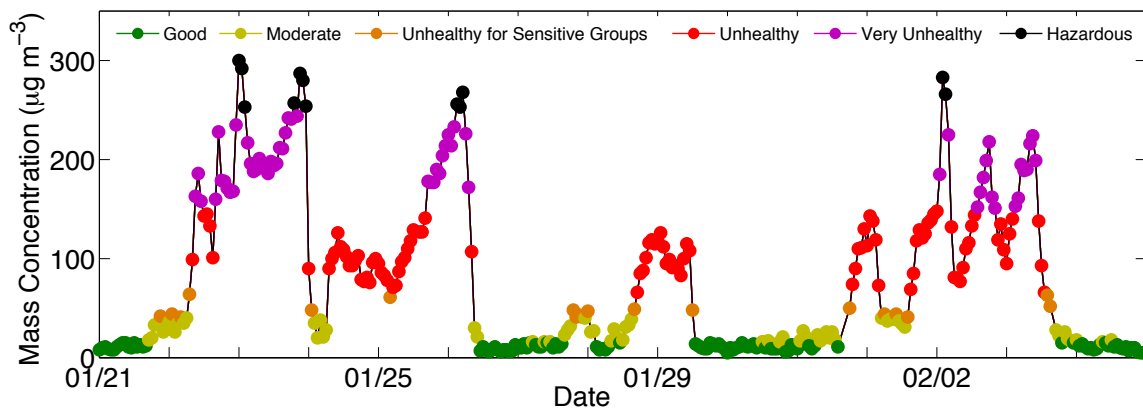


Figure 22. The $PM_{2.5}$ mass concentration and the corresponding air quality index between 21 January and 5 February 2015.

three years experienced at least one ‘hazardous’ episode. Both the public and the scientific community have extensively discussed the $PM_{2.5}$ mass concentrations in 2013 and 2014 since these winters were exceptionally polluted (Figure 21B), which resulted in global awareness of the extreme haze events [Gou *et al.*, 2014; Sun *et al.*, 2014]. In comparison, January and February 2015 appeared to be less polluted due to the implementation of new regulations and mitigation strategies; however, the 2015 $PM_{2.5}$ mass concentration was comparable to the concentrations observed between 2010 and 2012 (Figure 21B). It is noteworthy to add that if the mixing layer depths from winter 2015 and winter 2013, i.e. the winter that produced extraordinarily high mass concentrations, are compared, winter 2015 exhibited higher mixing layer depths, which may partially explain the lower average mass concentration in winter 2015.

In Figure 22, the $PM_{2.5}$ mass concentration measured between 21 January and 5 February 2015 and the corresponding AQI have been displayed. During this two week measurement period when all the instruments were online, we were able to examine

three pollution cycles, two of which reached a ‘hazardous’ ranking according the U.S. AQI criterion. In order to better understand the mechanisms that led to these events, we focused on the temporal evolutions of the number size distribution, $PM_{2.5}$ mass concentration, chemical composition, total number concentration, and average diameter measured between 21 and 27 January 2015 (Figure 23). Each haze event began with a NPF event, which was followed by continuous particle growth over several days (Figure 23A). The total number concentration exceeded $300,000\text{ cm}^{-3}$ during the NPF events, but generally remained below $200,000\text{ cm}^{-3}$ otherwise (Figure 23 C). The average diameter of the particles was about 10 nm during the NPF events and steadily increased until their average diameter was near 150 nm (Figure 23D). In the subsequent days, the average diameter cycled between 50 and 130 nm. The influence of the PBL was apparent because the highest concentrations were frequently observed overnight after the PBL contracted (Figures 23B, C). During overnight 22 January and the morning of 24 January, the concentration initially increased and the diameter decreased; so it is possible that as the atmosphere compressed, smaller particles were brought down from the upper boundary layer. Minor mass growth was observed on 21 January (Figure 23B), with an increase from $8\text{ to }30\text{ }\mu\text{g m}^{-3}$, and the most rapid mass concentration increase occurred on 22 January, with an increase from $30\text{ to }300\text{ }\mu\text{g m}^{-3}$. The chief difference between these two days was the relative humidity; the relative humidity was below 30% on 21 January and greater than 60% on 22 January. At first glance, the mass concentration appears to indicate that this event should be broken into two separate episodes (21-23 and 24-26 January); however, the properties of the aerosols (i.e. size, chemical

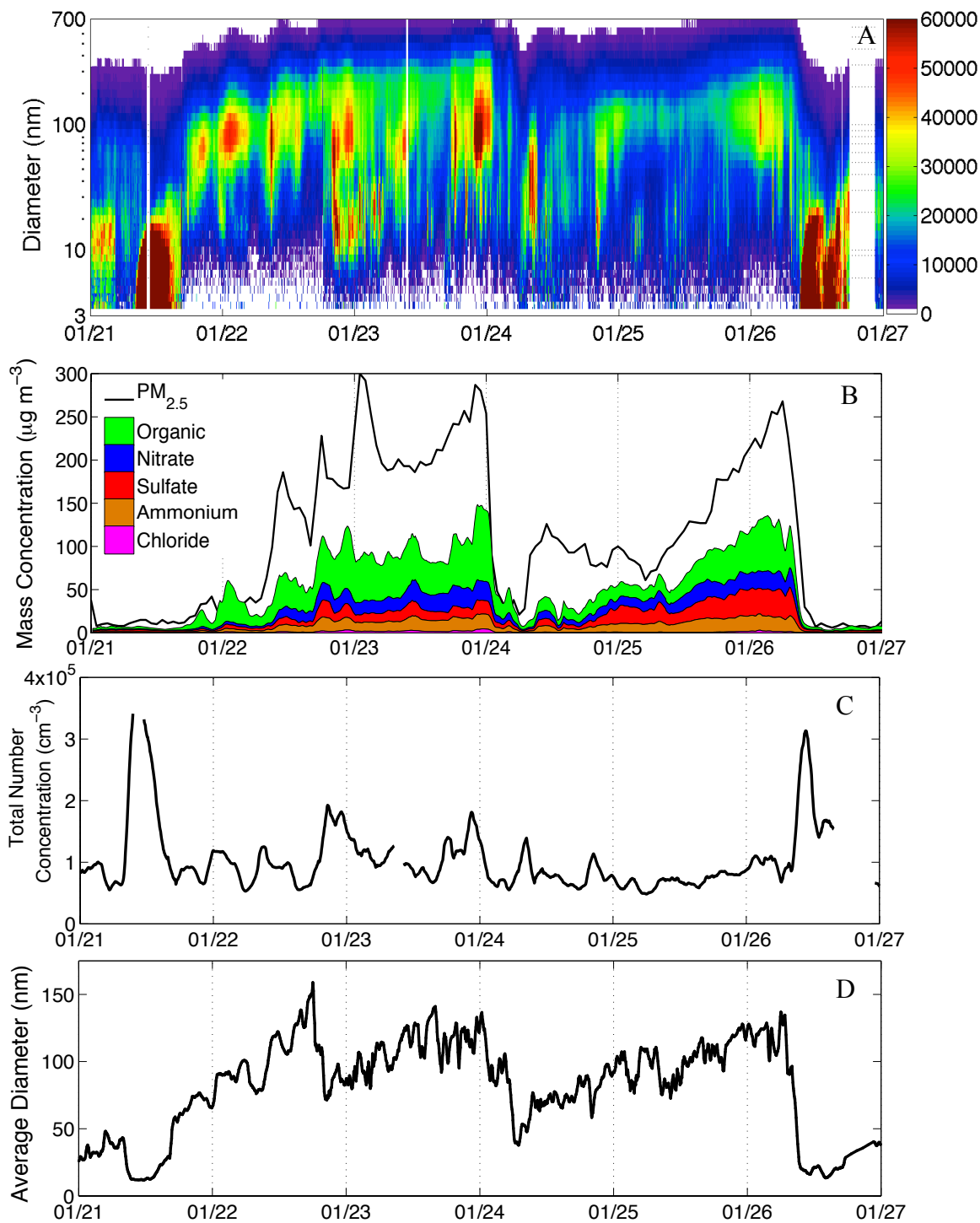


Figure 23. Temporal evolutions of the A) number size distribution, B) PM_{2.5} mass concentration, chemical composition, C) total number concentration, and D) mean diameter between 21 and 27 January 2015.

composition, and effective density) were consistent throughout the entire period and no

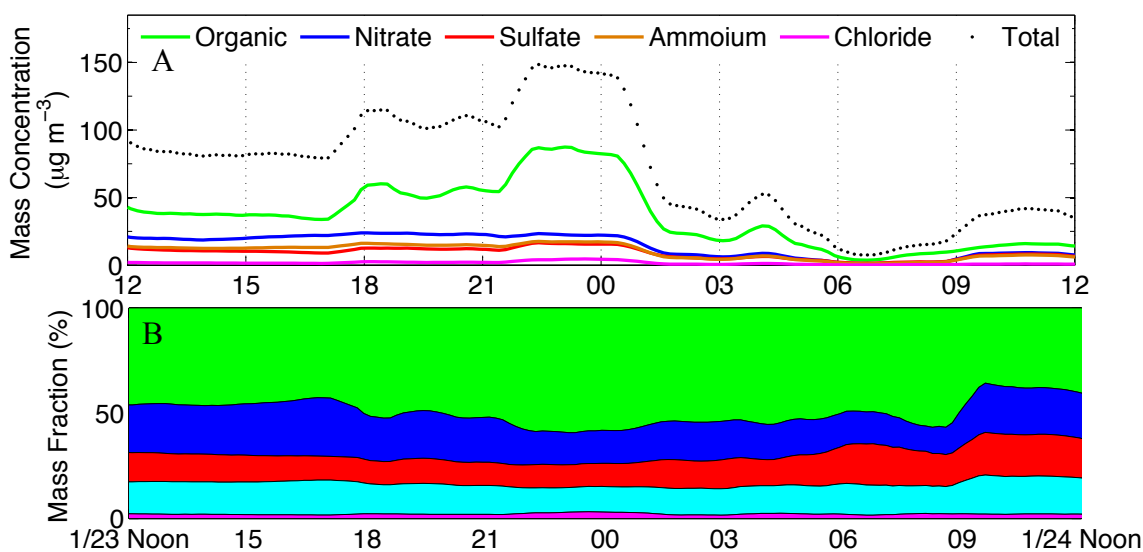


Figure 24. A) The mass concentration ($\mu\text{g m}^{-3}$) and B) mass fraction from 12 p.m. on 23 January to 12 p.m. 24 January.

NPF event was observed. In Figure 24, the mass concentration and the mass fraction have been displayed. It is clear that even though the mass concentration exhibited a substantial decrease, the ratio of the aerosol constituents remained quite constant, indicating that the air mass as a whole was the same. Furthermore, a back-trajectory analysis using the HYSPLIT model revealed that on 23 January the boundary layer was very low (~ 350 m during the afternoon) and the winds were calm, thus creating extremely stagnant conditions. Conversely, on 24 January a weak front passed through the region, which initially created weak winds from the north and enough vertical lift to increase the PBL to around 700 m. The increased winds and enhanced boundary layer height diluted the mass concentration in Beijing. However, after the frontal passage, the winds shifted to southerly, which recirculated the air mass back into the region. On 25 January, weak winds continued to come from the south and the boundary layer height

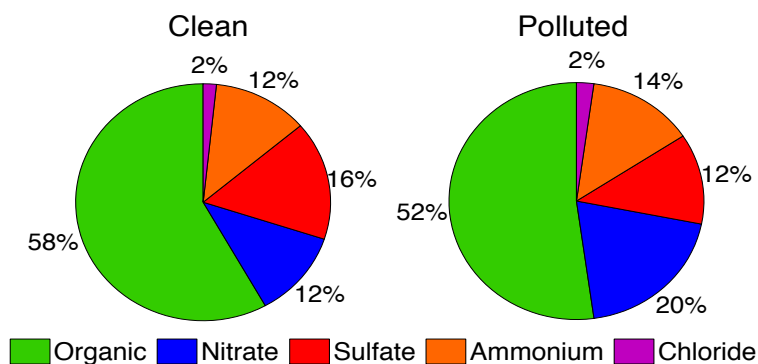


Figure 25. Comparison of the chemical composition between the clean and polluted periods.

increased to about 300 m; therefore, the stagnant conditions and accumulation of pollutants resumed.

Organic aerosols accounted for the largest percent of the aerosol mass (Figure 25) during both the clean (58%, 21 January) and the polluted phase (52%, 23 January). Nitrate, ammonium, and sulfate accounted for 12, 12, and 16%, respectively, during the clean phase, and they remained fairly constant throughout the polluted phase at 20, 14, and 12%. Nitrate exhibited the largest percentage increase of the three. Chloride remained constant at about 2%. It is apparent in Figure 23B that a large percentage of the $PM_{2.5}$ was unaccounted for in the AMS measurements. The AMS provides quantitative measurement of the chemical composition of non-refractory aerosols with a diameter between 40 and 1000 nm; therefore, any particles with a diameter between 1.0 and 2.5 microns or are composed of black carbon or mineral elements will be excluded. It is likely that the exclusion of black carbon accounts for some of this discrepancy, since it accounted for 5-15% of the aerosol mass during the fall campaign and this percentage would likely be higher in the winter due to increased heating demands during the winter

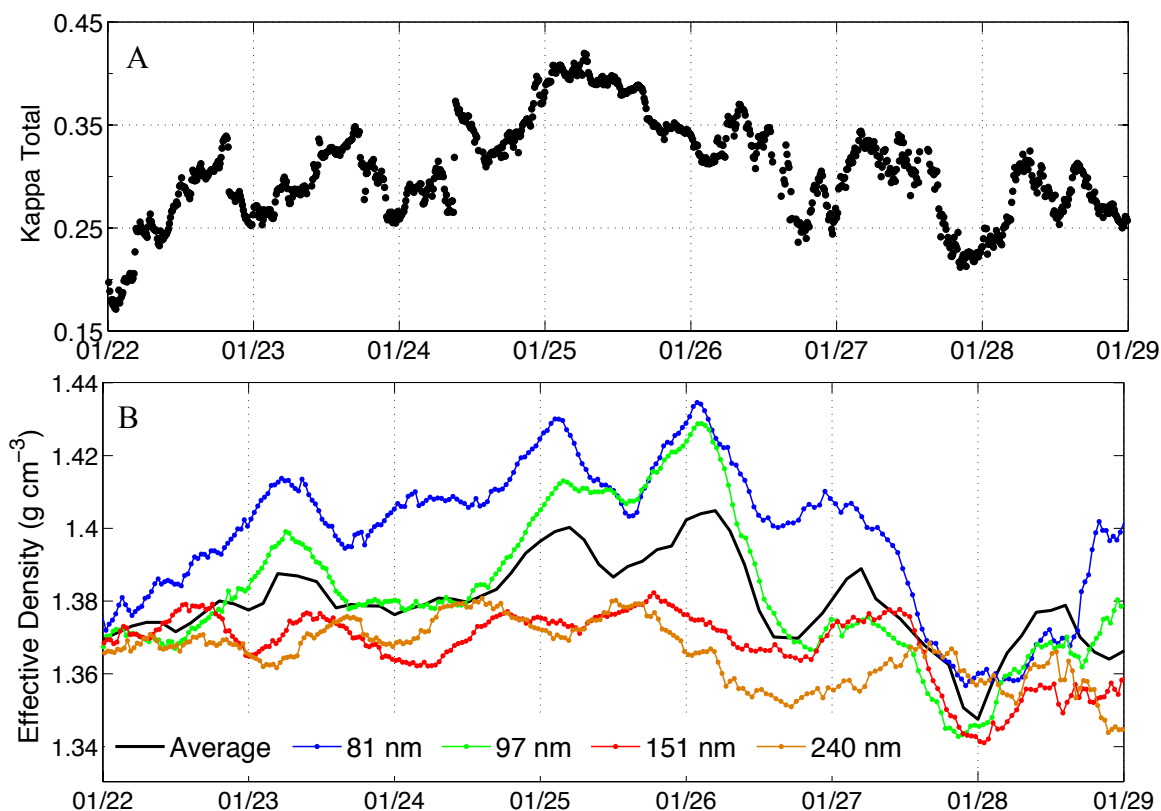


Figure 26. A) The hygroscopicity determined on the basis of chemical composition (i.e. kappa) of the aerosols. B) Temporal evolutions of the effective density of particles with a diameter of 81 (blue), 97 (green), 151 (red), 240 nm (orange), and the weighted average of the four particle sizes between 21 and 29 January 2015.

(Figure 14). In addition, several substantial dust storms occurred during early 2015 in Beijing; therefore, dust may account for a large portion of the missing aerosols.

The hygroscopicity of the aerosols determined on the basis of chemical composition between 21 January and 29 January 2015 is shown in Figure 26A. Both a diurnal cycle and an overall trend governed by the pollution cycle are evident in the aerosol hygroscopicity. Diurnally, the least hygroscopic aerosols were observed overnight, while the most hygroscopic were observed near sunset. The reduced nighttime

hygroscopicity was concurrently observed as the transiently elevated organic aerosol mass concentration (Figure 23B) and reduced effective density of the larger particles (Figure 26B), therefore this may be due to the increase of diesel vehicles in the city overnight, which produce copious amounts of hydrophobic POAs and black carbon. The increased hygroscopicity in the mid-morning and early afternoon hours (9 a.m. to 1 p.m.) was due to the rapid increase in the mass concentrations of nitrate, ammonium, and sulfate aerosols (Figure 23B). Previous work in Mexico City revealed that ammonium nitrate (NH_4NO_3) dominated the inorganic aerosol fraction and rapid production of NO_3^- was observed in the morning hours between 08:00–12:45. A box model was used to analyze these variations and found that the concentration increase was caused chiefly by secondary formation (~80%), with a lesser contribution from the entrainment of air from the free troposphere (~20%) [Hennigan *et al.*, 2008]. It is probable that a similar mechanism is occurring in the Beijing region given the rapid increase of both ammonium and nitrate. From the onset of the first pollution cycle on 21 January to the peak hygroscopicity on the morning of 25 January, the hygroscopicity increased from 0.15 to 0.42, revealing that the conversion of an air mass that is predominantly composed of organic aerosols (κ ranges between 0.07 to 0.29 dependent on the species and degree of oxidation [Chang *et al.*, 2010]) to one that also contains organics, nitrates (0.58), ammonium (0.55), and sulfates (0.48).

The effective density for 81, 97, 151, and 240 nm particles are exhibited in Figure 26B. During the clean phase, all four particle sizes exhibited effective densities that clustered near 1.38 g cm^{-3} , but as the cycle progressed, the effective densities

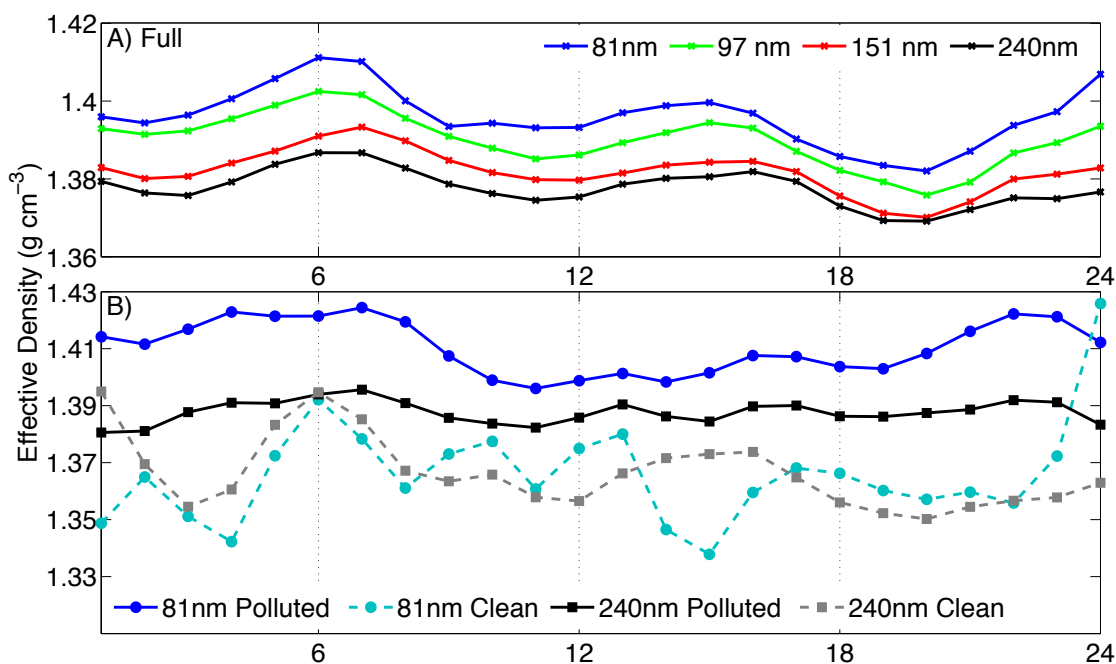


Figure 27. A) The diurnal cycle of the effective density (g cm^{-3}) of the four particle sizes from the full observational period. B) The effective density (g cm^{-3}) diurnal cycle of the 81 (blue circles) and 240 (black squares) nm particles during the clean (dashed, lighter colors) and polluted periods (solid, darker colors).

became dissimilar. As the $\text{PM}_{2.5}$ mass concentration decreased at the end of the haze event (i.e. 27 January), the effective density of the particles again clustered near 1.35 g cm^{-3} . The lower average effective density during the clean period can be attributed to the organic dominated aerosols composition. Furthermore, the increasing effective density corresponds to the increasing sulfate and nitrate composition that was observed as the haze events progressed (Figure 23B). Generally, the effective density distributions were unimodal, indicating that the aerosols were internally mixed. The weighted average, i.e. the effective density weighted by the total number concentration of particles near each size, of the four particles sizes is depicted by the black lines. It is clear that the average effective density increased throughout the haze event, but this was largely due to the

changes in the particles smaller than 100 nm. The smaller particles (i.e. 81 and 97 nm) increased in effective density as the region became more polluted; whereas, the larger particles (i.e. 151 and 240 nm) remained near 1.37 g cm^{-3} . In Figure 27, the average diurnal cycle of the effective density of 81, 97, 151, and 240 nm particles are displayed from the full observational period, the polluted period, and the clean period. It is clear that a diurnal cycle existed, i.e. an increasing effective density overnight, decreasing effective densities during the morning and evening rush hours, and moderately stable effective densities during the day. In the full campaign, the lowest average effective densities were observed during the afternoon hours (i.e. 1.38 g cm^{-3} for 81 nm particles), and the highest average effective density ($\sim 1.41 \text{ g cm}^{-3}$ for 81 nm particles) was observed in the early morning before the intensification of traffic. During the elevated traffic periods (i.e. 6 - 9 a.m. and 4 - 8 p.m.), the effective density decreased likely due to the increased concentration of black carbon and POAs. Overnight, the effective density likely increased to due to aerosol aging. The variation in the effective density was suppressed during the polluted days. This may be due to the variations in the PBL (i.e. high on clean days, but low on polluted days) and because the newly emitted particles were being mixed into a higher concentration of particles; therefore, the average effective density of the entire air mass was not as sensitive to the individual particles.

Frequently, the large-scale meteorology governed the length and severity of haze events because the region was either exceedingly stagnant or there were strong, cleansing winds. On the clean days (i.e. 21 January and 27 January) the winds were very strong and the PBL was high, which enhanced the dilution of pollutants both vertically

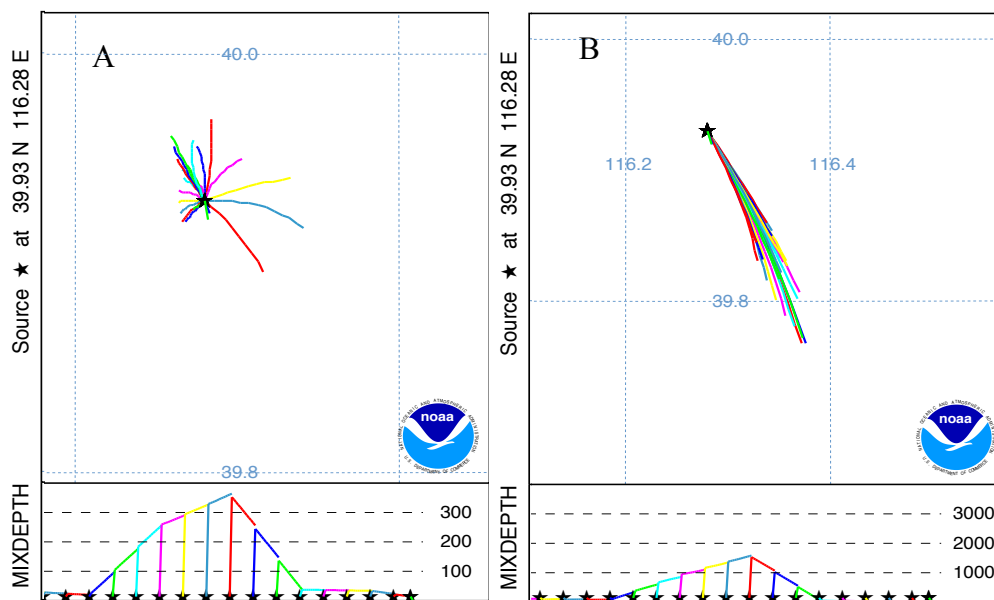


Figure 28. Typical synoptic conditions observed during A) polluted and B) clean days. The forward trajectories and mixing depths were determined by the HYSPLIT model.

and horizontally (Figure 28). The days with the highest concentration (i.e. 22 January and 26 January) exhibited calm winds and low PBL heights, which trapped the pollutants near their emission source.

c) Comparisons of Beijing Aerosol Properties from Fall 2013 and Winter 2015

One of the primary goals of conducting a second field campaign during the winter period was to elucidate the seasonal variations, if any, in the haze formation mechanisms. In Figure 29, a comparison of the mass concentration, total number concentration, and the average diameter from the fall 2013 and winter 2015 field campaigns has been displayed, and a comparison of the chemical composition during the clean and polluted period from both campaigns is exhibited in Figure 29. Both seasonal

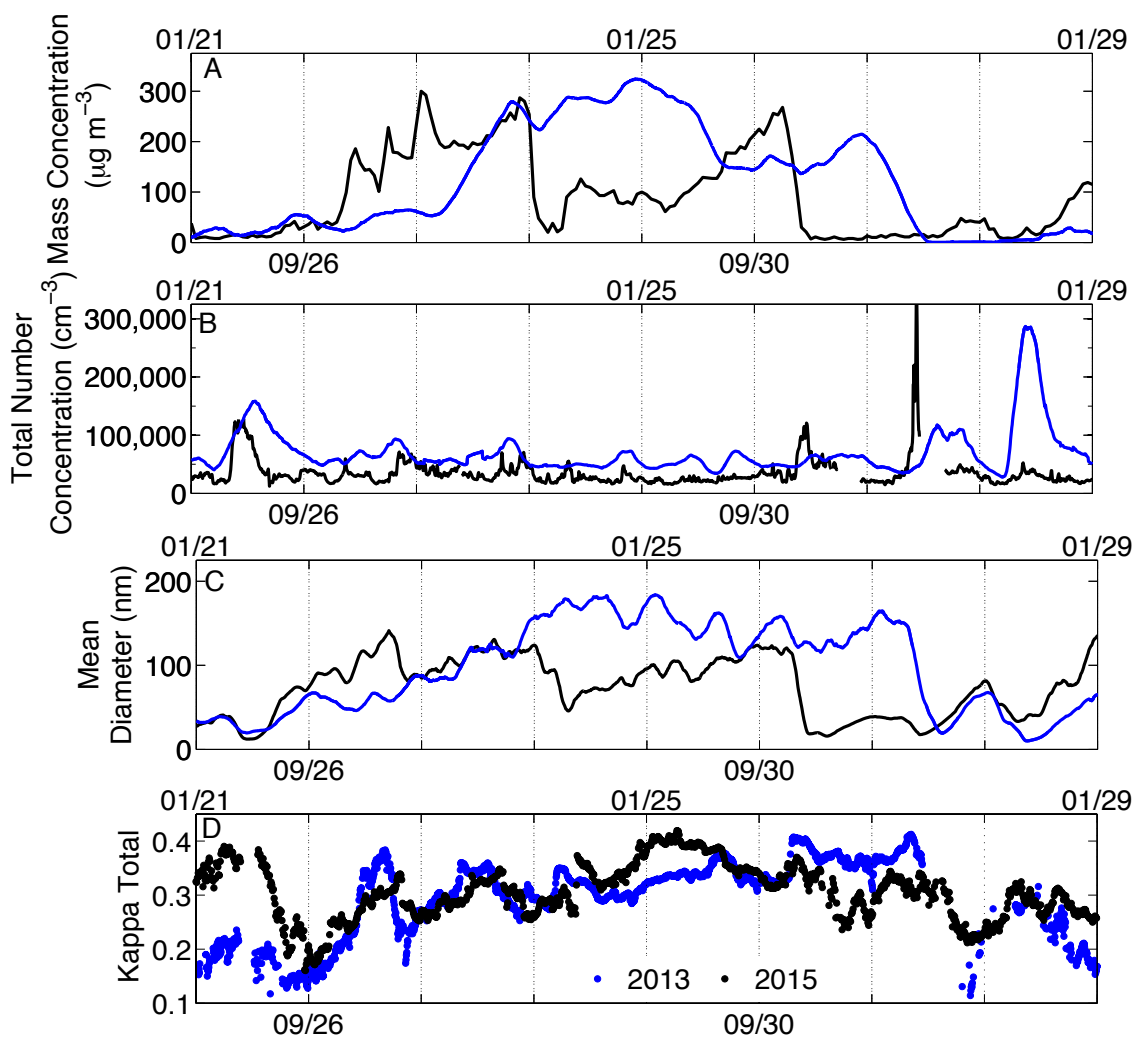


Figure 29. A comparison of the A) mass concentration, B) total number concentration, C) average diameter, and D) hygroscopicity between the fall 2013 and winter 2015 field campaigns.

haze events began with NPF events, which were typically followed by particle growth over several days. The large-scale meteorological processes heavily influenced the haze cycles during both seasons. Overall various properties (i.e. particle size, number concentration, chemical composition) appear to be similar in the fall and winter

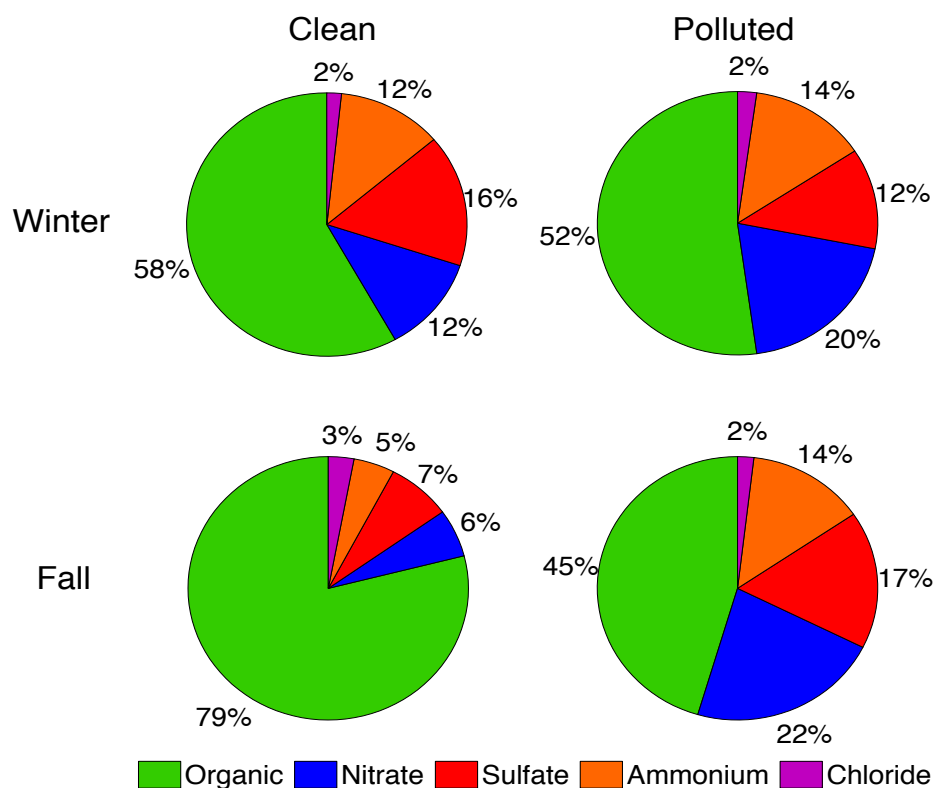


Figure 30. A comparison of the chemical composition during the clean and polluted period from both campaigns.

campaigns, with a few notable caveats (Figures 29 and 30). The particle growth and formation was more efficient in the fall campaign: i.e. the final particle size was near 200 nm in the fall compared to 150 nm in the winter, and the NPF events resulted in a greater total number concentration. This could be due to several reasons. First, it has been shown in previous work that increased RH enhances particle growth particularly for hygroscopic particles, such as sulfates, but the winter of 2015 was especially dry, i.e. there was only one very light winter weather event in the two months the researchers were in Beijing. Therefore, the dry conditions during this winter may have suppressed particle growth, which in turn reduced the total mass concentration. Also, the efficiency

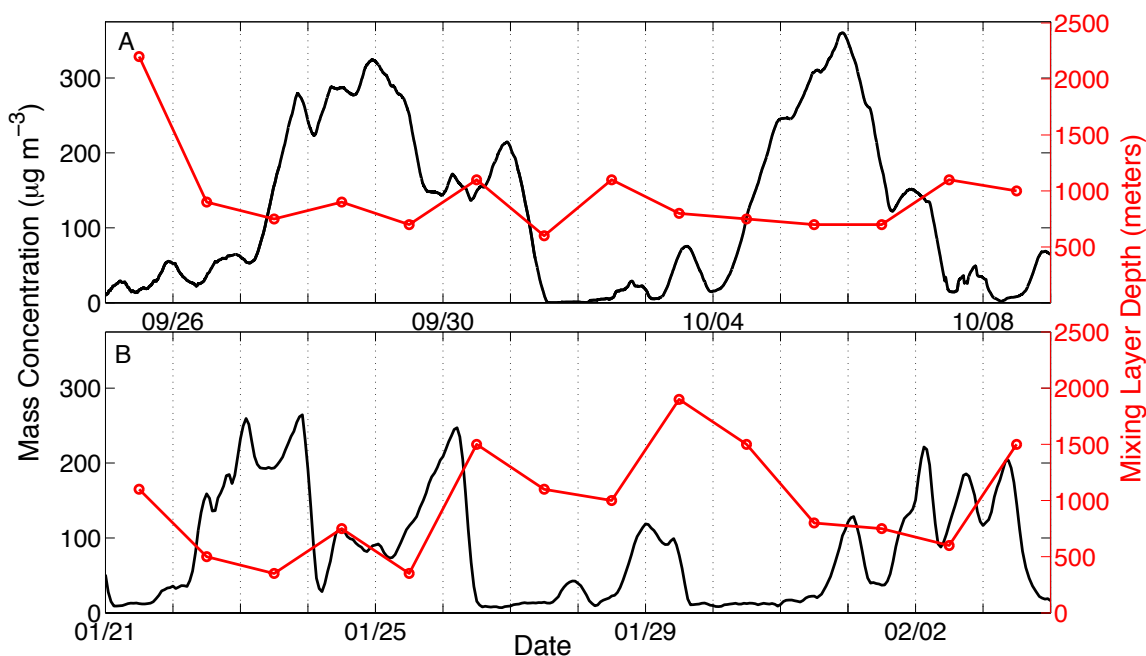


Figure 31. A comparison of the mixing layer depth (m) determined by the HYSPLIT model and the mass concentration ($\mu\text{g m}^{-3}$) in A) Fall 2013 and B) Winter 2015.

of NPF events is dependent on the intensity of solar radiation: the stronger the sunlight, the more efficient the NPF events. Therefore, the fall haze events were seeded with a higher concentration of particles, which then grew and resulted in a higher mass concentration. Furthermore, if the mixing layer depth is taken into consideration (see Figure 31), the particle growth and formation was likely much more efficient in the fall because while the resultant concentrations were similar, the mixing layer was nearly twice as high during the fall.

The trends in the hygroscopicity of the particles are similar between the two seasons (Figure 29D), with the only significant difference occurring on the clean days (i.e. 21 January, 25 September, 27 January, and 1 October). The hygroscopicity of the fall aerosols (25 September) during the clean phase was much lower (0.2) than the

hygroscopicity of the wintertime aerosols (0.35). This is likely due to the increase presence of sulfate (7% in the fall, 16% in the winter, Figure 30) due to residential heating and suppressed dilution of local pollutant (mixing layer depth of 1100 m compared to 2200 m, Figure 31).

CHAPTER IV

DOES MATERNAL EXPOSURE DURING PREGNANCY FUNDAMENTALLY ALTER HER OFFSPRING? ANIMAL PROXY STUDIES OF EXPOSURE TO POLLUTANTS UNDER ATMOSPHERICALLY RELEVANT CONDITIONS

i) Introduction

Atmospheric aerosols affect human health in numerous ways, ranging from aggravating allergies, the development of serious chronic diseases, or leading to premature death [Dockery *et al.*, 1993; Dockery and Pope, 1994; Gauderman *et al.*, 2004; Kunzli *et al.*, 2005; Yan *et al.*, 2014]. After inhalation, aerosols can affect nearly all the vital structures of the body including the lungs, heart, brain, and vascular system. The WHO estimated that in 2005 over 800,000 deaths occurred as a result of poor outdoor air quality, and recent studies are indicating that this assessment may have severely underestimated the mortalities due to air pollution. According to a 2014 news release, WHO now states that indoor air contributes to 4.3 million deaths globally and outdoor air pollution from urban and rural sources is likely linked to 3.7 million deaths in 2012. As the global urbanization trend continues these number are likely to correspondingly increase. The mortality rates are disproportionately high in low and middle income countries (88%), and the greatest burden of diseases has been found to be in the Western Pacific and South-East Asia regions [WHO, 2014]. A recent study calculated that 1.6 million deaths each year (or 4,000 deaths per day) could be attributed to PM_{2.5} air pollution in China [Rhode and Muller, 2015]. It has been projected that the 500 million residents living in northern China have lost a total of 2.5 billion years of life expectancy,

which is roughly a 5.5 year life reduction per person, due to an increased incidence of cardiorespiratory mortality [*Chen et al.*, 2013]. Fatalities due to aerosol exposure result from many pathways including respiratory infection, interference with lung function, cancers, cardiovascular disease, and stroke [*Dockery et al.*, 1993; *Dockery and Pope*, 1994; *Millman et al.*, 2008]. WHO attributed 40% of mortalities to ischemic heart disease, 40% of mortalities to stroke, 11% of mortalities to chronic obstructive pulmonary disease (COPD), 6% of mortalities to lung cancer, and 3% of mortalities to acute lower respiratory infections in children [*WHO*, 2014].

Not all atmospheric compounds and particle sizes are equally dangerous to human health; however, PM_{2.5} is often treated as a uniform pollutant in health related studies, regardless of its properties and chemical composition. Ultrafine aerosols, i.e. particles with a diameter less than 100 nm, have greater effects on health as they are small enough to bypass the natural defenses in the human body and can be carried deep into the lungs where they can cause inflammation and worsen heart and lung diseases [*COMEAP*, 2006]. Although ultrafine aerosols contribute little to the overall ambient aerosol mass concentration, they are often present in high concentrations (see Figures 13 and 22). The relatively large surface area of ultrafine aerosols and their ability to form radical species are believed to induce inflammatory effects and cause cellular DNA damage [*Kreyling et al.*, 2004; *Araujo et al.*, 2008]. Other factors, such as aerosol hygroscopicity, may influence the uptake of aerosols within the lungs [*Broday and Georgopoulos*, 2001]. Knowledge of the impacts of the individual species and physical properties of particles is crucial to truly evaluate health impacts since biological

responses to PM will not always be linked with the major constituents, but rather with a minor, more influential species [Schlesinger *et al.*, 2006]. It has also been proposed that the toxicity of a mixture of primary and secondary gaseous species and PM can differ greatly from exposure to just one of the individual pollutants [Mauderly and Samet, 2009].

Unfortunately, certain individuals within a community are particularly sensitive to PM_{2.5}, such as children. Given the global urbanization trend, more children are conceived, gestated, and mature in polluted environments than ever before. Therefore, many studies have recently been conducted to determine how pollutant exposure during gestation alters the lifetime health of the individual. Reduced fetal and childhood growth, asthma, allergies, developmental impairment, preterm birth, reduced birth weight, an increased occurrence of intrauterine growth restriction, and increased risk of cancer in children have frequently been correlated with high PM_{2.5} loading [Millman *et al.*, 2008; Morgenster, *et al.*, 2008; Pereira *et al.*, 2012; Lung *et al.*, 2013]. Birth weight is a significant factor in neonatal survival (0 - 27 days of life) and lifelong health. Not only is low birth weight associated with increased perinatal morbidity and mortality, it is also associated with an increased incidence of certain diseases, such as diabetes, seizure disorders, cardiovascular diseases, and a number of neurological disorders later in life [McCormick, 1985; McCormick *et al.*, 1992; Norris, 2013].

Rats and other laboratory animals have frequently been used as human surrogates to assess potential health effects of inhaled particulate matter. The total deposition percent for 10, 50, and 100 nm particles was found to be 71, 40, and 22% in human

lungs and 52, 31, and 18% in rat lungs, respectively [Bergmann, 1998]. An analysis of the particle deposition efficiency of diesel exhaust PM in human and rat lungs performed by Yu and Xu [1986] found that despite the considerable differences in lung structure, airway size, and breathing parameters, human and rats exhibited similar deposition patterns of pollutants in the lungs. Dosimetric calculations indicate that rats may be less susceptible to inflammatory responses than humans from acute PM exposures, but more susceptible than humans to adverse pulmonary effects from chronic exposures to high levels of PM. However, since the clearance of PM is faster from the lung of rats than humans, much higher exposure concentrations may be required for the rat to simulate retained burdens [Brown et al., 2005]. Laboratory animals are frequently exposed to pollutants by administering intranasal or intratracheal doses [e.g., Wang et al., 2013] or full body exposure systems [e.g., Mauad et al., 2008; Veras et al., 2008], with a variety of research objectives. Veras et al., [2008] continuously exposed rats to pollution from a major highway exposed during pre-gestational and gestational periods and found changes in the functional morphology of the placenta. A two-way analysis of the variance revealed that both periods of exposure led to significantly smaller fetal weights when compared to rats in filtered exposure chambers. In a similar study, mice were exposed from the 10th to the 120th days of life in open-top chambers (filtered $\sim 3 \mu\text{g m}^{-3}$, nonfiltered $\sim 17 \mu\text{g m}^{-3}$) placed 20 m from a street with heavy traffic in Sao Paulo, Brazil for 24 hours/day for an 8 month period [Mauad et al., 2008]. After the mating and birth of offspring, the pups were divided into four groups: non-exposure, prenatal exposure, postnatal exposure, and pre and postnatal exposure. Mice exposed to traffic-

related PM in the pre- and postnatal period developed significant alterations of alveolar structure and lung elastic properties, indicating that traffic-related pollution adversely impacts lung growth [Mauad *et al.*, 2008]. In order to understand the mechanism by which ambient PM_{2.5} can affect the cardiovascular system, Wistar rats were intratracheally exposed to concentration of 0.2, 0.8, or 3.2 mg/rat of particulate matter [Wang *et al.*, 2013]. The heart rates, systolic blood pressure, and electrocardiogram were monitored at approximately 24-h after the 3rd exposure and 6th exposure. The results revealed that PM_{2.5} exposure can trigger a significant increase of systemic inflammation biomarkers and decreased heart rate variability. Furthermore, if the rats were concurrently exposed to ozone, the negative responses were found to be exacerbated [Wang *et al.*, 2013]. In a study conducted by Morishita *et al.*, [2004], Brown Norway rats, with and without ovalbumin-induced allergic airway disease, were exposed to concentrated air particles generated from ambient air in an urban Detroit community where the pediatric asthma rate was three times higher than the national average. Rats were exposed to either 676 $\mu\text{g m}^{-3}$ or 313 $\mu\text{g m}^{-3}$. It was found that the exposed rats demonstrated a higher retention of particle in allergic airways of air particulates derived from identified local combustion sources after a short-term exposure. Pollutant exposure has also been found to alter fertility markers (i.e. a reduction in the number of reproductive cycles, a significant increase in time necessary for mating, and a 70% increased post-implantation loss rates). Veras *et al.* [2009] demonstrated that exposure to ambient urban traffic PM negatively affects different functions and stages of the reproductive process, even if the exposure occurs only before conception. In this study,

both pre-gestational and gestational period exposure was linked to reduction in the fetal weight of the offspring [Veras *et al.*, 2009]. Interestingly, the reduction was similar for both pre-gestational and gestational exposure rats, with about a 20% reduction in the birth weight.

To date, scientists have not yet identified how a mother's exposure to air pollution alters the lifetime health of the offspring. This is due to complex processes that the fetus and mother undergo during gestation and is complicated by the fact that the mother will be exposed to many different pollutants throughout the protracted pregnancy. Due to the relative infancy of this area of investigation and the complex nature of the atmospheric pollutants, many effects have been identified through epidemiological studies; however, few animal model studies have been conducted to determine the cellular and molecular effects of air pollution on fetal development [Oldham *et al.*, 2004; Veras *et al.*, 2008; Guillette and Iguchi, 2012]. To try to understand the mechanism by which aerosols diminish human health, a series of animal exposure studies has been conducted to investigate the physiological responses of the mothers and offspring.

This project was funded as one of Texas A&M University's Tier One Program (TOP) grants. The program was designed to offer special faculty grants offered by the university to facilitate hands-on, interdisciplinary educational experiences that integrate emerging scholarly work with experiential and high impact learning practices into curricular offerings for students at Texas A&M. In order to qualify for a grant, the proposal must be a joint effort between faculty members of two or more academic

colleges. Our project, entitled ‘Enhancing Teaching and Research in Health Impacts of Air Pollution’, was done in collaboration with the Department of Animal Science in the College of Agriculture and Life Sciences and the Veterinary Integrative Biosciences Department in the College of Veterinary Medicine & Biomedical Sciences at Texas A&M University. Each department was responsible for different phases of the project. Our group in the Department of Atmospheric Science was tasked to design, test, and maintain a system that would continuously expose laboratory animals to pollutants of known size, concentration, and composition for weeks at a time. The Department of Animal Science was responsible for obtaining, caring for, humanely euthanizing, and dissecting the experimental animals. The Departments of Animal Science and Veterinary Integrative Biosciences were jointly responsible for collecting samples and conducting analysis of the dams and offspring including: weight variations, food intake data, metabolic chamber data, vascular ring stretch data, plasma analysis, gene expression in organs, and histology of organs. The tissues collected for analysis from dams and offspring pups included: heart, skeletal muscle, kidney, spleen, small intestine, brain, lung, testis, liver, ovary, white adipose, uterus, brown adipose, and trachea. The ultimate goal of the project is to elucidate the physiological responses by the mothers and the transgenerational effects of maternal air pollutant exposure on utero development.

ii) Developing the Animal Exposure System

a) The Chamber

The design of the chambers needed to address several criteria: 1) the pollutants must be evenly distributed throughout the chambers so that the animals are equally exposed, 2) the individual compartments must meet the requirement set forth by federal regulations, 3) the enclosure must allow for easy access to the animals in order to tend to the animal's daily needs, 4) the air flow must be rapid enough to generate at least 15 complete air exchanges per hour, 5) the system must be reasonably quiet since rats are sensitive to sight, sounds, and smells, and 6) the system must be able to operate for long periods of time unattended. A previous experiment that utilized a mobile whole-body exposure system that was designed to hold nine mice was used as the basis of our chamber design. While the space requirements differ between mouse and rat experiments, this prototype demonstrated inner plumbing that effectively produced no stagnant areas and good mixing throughout the exposure cage [Oldham *et al.*, 2004].

The custom-built compact whole-body stainless steel cage enables the uniform exposure of several animals simultaneously in individual compartments, while minimizing PM losses by deposition. The animal exposure chamber design consisted of a 12" x 8" x 32" stainless steel box with four inner compartments and a ¼" clear cast acrylic lid as shown in Figure 32. Air is continuously pumped through the chamber by stainless steel tubing attached to the lid and bottom of the chamber (Figures 32 and 33). The u-shaped inflow lines, attached to the underside of the lid, have evenly distributed

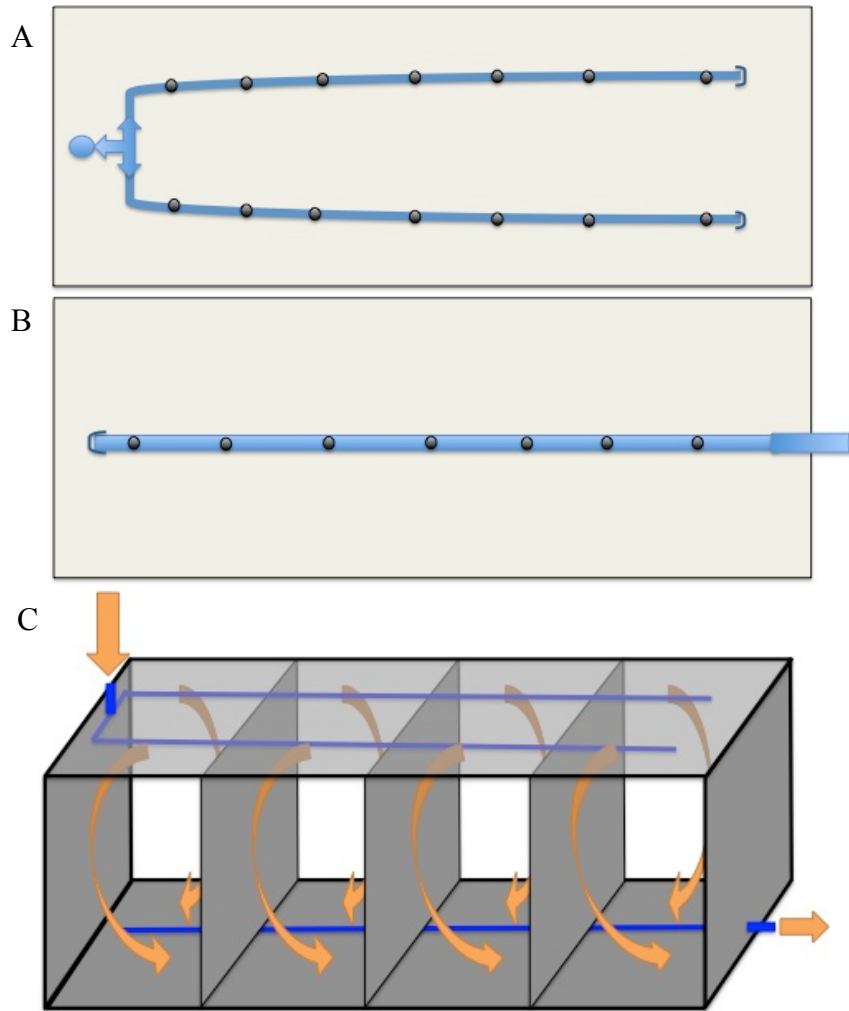


Figure 32. Schematic of the animal exposure chamber. The top panel depicts the underside of the lid, the middle panel is the bottom of the chamber, and the bottom panel illustrates the airflow within the chamber. The u-shaped inflow lines, attached to the underside of the lid, have evenly distributed holes over each of the compartments to produce even flow and exposure in each individual space. The outflow line, attached to the bottom, also has evenly distributed holes under each of the compartment to facilitate uniform removal of the chamber air.

holes over each of the compartments to produce even flow and exposure in each individual space. The inflow lines bring in ambient room air, which typically has a mass

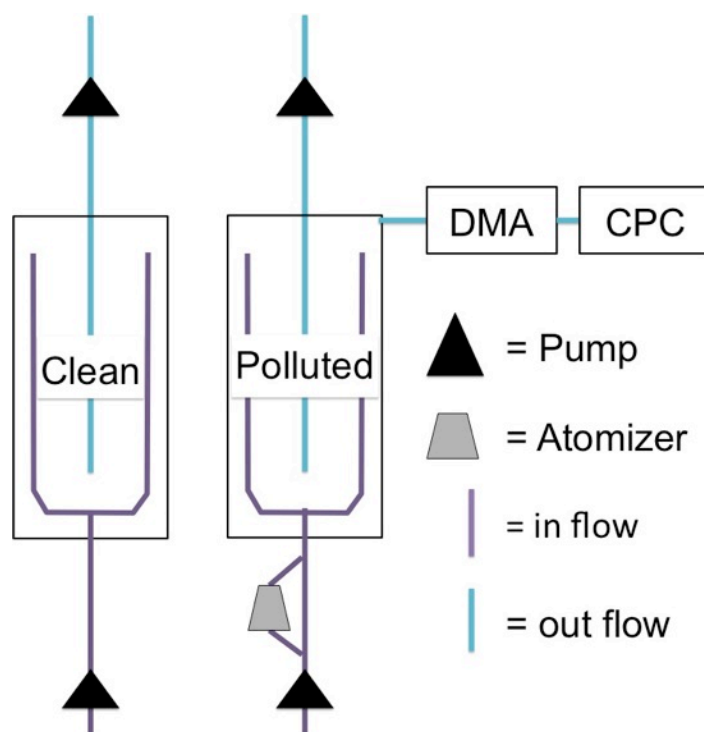


Figure 33. Diagram of the animal exposure chambers and instruments. Pure ambient air is pumped into the clean chamber, and doped ambient air is pumped into the polluted chamber. The polluted and clean systems are independent of each other. The system flow rate is 55 LPM or 67 chamber turnovers per hour. The polluted chamber aerosols are sampled at a rate of 1 LPM by the DMA and CPC.

concentration less than $5 \mu\text{g m}^{-3}$. The average mass concentration from background measurements was $3.03 \mu\text{g m}^{-3}$ (Figure 35D). The animal facility is a strictly controlled macro- and micro-environments, where the air is filtered and the temperature, humidity, light cycles, space, food, water, and bedding are all monitored and maintained within established parameters appropriate for the species.

The outflow line, attached to the bottom of the chamber, has evenly distributed holes under each of the compartments to facilitate uniform removal of the chamber air. The system flow rate is 55 LPM or 67 chamber turnovers per hour. The transparent lid



Figure 34. The chambers constructed for the animal exposure experiments.

permits direct observation of the animals during the exposure experiments, and the suspended perforated cast acrylic removable floor maintains a clean environment for the animals. Two independent chambers were built for the polluted and clean systems as can be seen in Figure 34.

b) Producing and Maintaining High Aerosol Loading

In addition, the polluted system comprises an atomizer to produce a steady flow of aerosols, a multi-tube Nafion drier to remove excess water vapor, and an SMPS to constantly monitor the size distribution of particles (Figure 33). A continuous atomizer is positioned between the pump and the polluted chamber in order to raise the mass concentration in the ambient air to a near $150 \mu\text{g m}^{-3}$, a concentration is frequently observed in Beijing, as can be seen in Figure 35. The average mass concentration in Figure 35B is $152.96 \mu\text{g m}^{-3}$ and typically varies between 100 and $200 \mu\text{g m}^{-3}$. The red points indicate the times when daily animal care was performed, and the blue dots indicate the time when machine maintenance or calibration was typically conducted. During these times, the animals may have been weighed, the cages may have been cleaned, or the instruments was calibrate; therefore one or both of the pumps may have been turned off, resulting an over or underestimation of the PM concentration in the chamber. The aerosols are sampled at a rate of 1 LPM through a thermally insulated 3/8" stainless steel tubing and then passed through a series of Nafion driers to reduce the relative humidity of the aerosols to less than 10%. The sheath flow rate was maintained at 3 LPM. Then the polydispersed aerosols were brought to charge equilibrium and passed through the DMA and CPC to determine the particle size distribution between 3 and 400 nm in the ambient air. Particle size distributions are acquired approximately every five minutes, and the data is averaged and recorded every 15 minutes. The particle size distributions shown in Figure 35 demonstrate the relative stability of the mass concentration over an hour's time. The median particle size for different PM species can

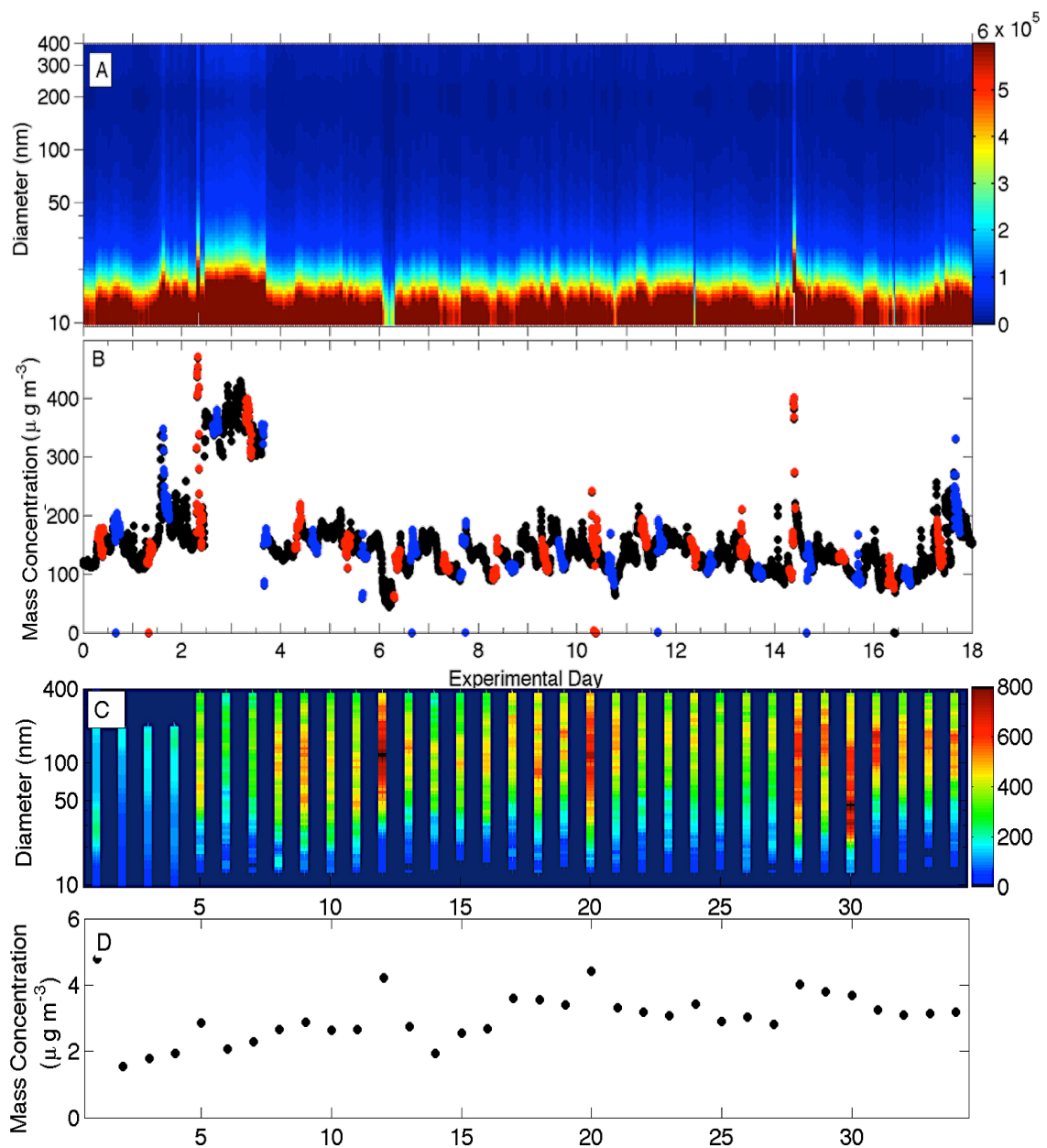


Figure 35. The number concentration distributions and the calculated total mass ($\mu\text{g m}^{-3}$) of ammonium sulfate measured by a Differential Mobility Analyzer A-B) in the chamber and C-D) in the ambient room air. The scans were measured on various days throughout the experiment. The red points indicate the times when daily animal care was performed, and the blue dots indicate the time when machine maintenance or calibration was typically conducted.

be varied in the range from a few nanometers to few hundred nanometers by adjusting

the particle formation conditions. Using the known effective densities of the pollutant aerosols, i.e. 1.77 g cm^{-3} for ammonium sulfate, and number size distributions, the mass concentration was determined by the following equation:

$$\text{Mass Concentration} = \int_{3 \text{ nm}}^{400 \text{ nm}} \frac{1}{6} \times dN \times \pi \times D^3 \times \rho_{eff} \times \Delta D$$

where dN is the total concentration, D is the particle diameter, and ρ_{eff} is the effective density.

Given that the atomizer may increase the number of charges on the particles introduced into the polluted chamber, the experimental system may result in enhanced deposition in the lungs of the rats compared to natural aerosol. However, it is difficult to estimate the significance of this enhancement. Experimental studies indicate an enhanced deposition of about 12% in the tracheobronchial region and 23% in the alveolar region for $0.3 \text{ }\mu\text{m}$ particles during normal breathing. However this deposition enhancement was dramatically different for light breathing, exercise breathing, and sitting breathing [Majid *et al.*, 2012]. For singly charged 20-nm particles deposition efficiency was found to about 3 times that for neutralized aerosols and 5 times the deposited for zero-charged particles, although, these values are not directly applicable to our scenario because ambient atmospheric particles are frequently charged [Cohen *et al.*, 1998].

c) Methodology for Animal Experiments

This project is intended to be the foundational experiment for a series of more complex combination of pollutants. In this base scenario, the animals were exposed to pure ammonium sulfate aerosols, which have a low toxicity [Schlesinger, 1984], in order to assess the influence of aerosols processing by the animals, without the confounding toxic effects that might occur due to exposure to the compounds themselves, such as by black carbons which contain polycyclic aromatic hydrocarbons (PAHs) that have been highly correlated with the development of cancer. In each experiment, pregnant Sprague-Dawley rats (4 control, 4 polluted per experiment) were individually housed and continuously exposed to ambient air with and without added ammonium sulfate aerosols. Sprague-Dawley rats are fast growing, docile, and easy to handle albino outbred rats that are ideal for general multipurpose model, safety and efficacy testing, aging, nutrition, diet-induced obesity, oncology, toxicology, and surgical models. The gestation length of healthy Sprague-Dawley rats is 21 days, and the average litter size is 11 pups.

On the first day of the experiment, 70 day old female rats, i.e. dams, were housed with age-matched males, i.e. bucks, until a vaginal plug was observed, which indicates that mating has transpired. Mating generally occurs within 24 hours of introducing a dam to a buck. Once the plug was observed, the dam was immediately placed into one of the chambers. The dams remained in the chambers from prenatal day 0 – 18, where day 0 indicates the day of mating. Throughout this period, the dams were weighed on prenatal day 0, 6, 12, and 18, and their water and food consumption was monitored. Between day 0 of pregnancy and weaning, dams had free access to food and drinking

water. On prenatal day 19, the dams were removed from the atmospheric chambers and housed individually in standard cages until parturition to ensure that none of the dams gave birth within the experimental chambers. At birth, i.e. postnatal day 0, the rat litters were reduced to eight rats, four males and four females. The other offspring were weighed, euthanized, and their tissues snap frozen in liquid nitrogen for further analysis. The remaining eight pups from each litter were reared on their dam until weaning. At postnatal day 21, the four rat pups (two males and two females) and dams were weighed, sacrificed, and their tissues were snap frozen in liquid nitrogen or fixed in paraformaldehyde for further analysis. The remaining 4 pups began either a low or a high fat diet for a 12-week period [Jobgen *et al.*, 2009]. At postnatal day 105, these pups were weighed, sacrificed, and their tissues snap frozen in liquid nitrogen or fixed with paraformaldehyde for further analysis. The tissues collected at euthanization for analysis from the offspring pups included: heart, skeletal muscle, kidney, spleen, small intestine, brain, lung, testis, liver, ovary, white adipose, uterus, brown adipose, and trachea. The tissues were stained with hematoxylin and eosin for initial analysis to determine abnormalities and variations in histology in the exposed versus control rats. Portions of all organs were snap frozen in liquid nitrogen and a portion preserved in 4% paraformaldehyde for future studies that are beyond the scope of the current project.

The gestation length, litter size, average and total pup size, and sex ratio were assessed throughout the animal exposure studies. Treatment, sex, and treatment by sex interactions were also analyzed. All organ weights were adjusted using pup weight as a covariate in the model. Throughout the experiments clean lab coats, shoe covers, and a

hair bonnet were worn in all hallways, housing rooms, and animal procedure rooms in order to keep the animals free from exposure to disease, bacteria, viruses, and other pathogens.

iii) Results and Discussion

While the bulk of the experimental data and conclusions will be included in the dissertations of the graduate science students in the Departments of Animal Science and Veterinary Integrative Biosciences, I will briefly highlight the conclusions to establish the validity of the methodology. Our analysis revealed that maternal exposure to pollutants does negatively affect the offspring. In total, 326 dissections (20 dams, 306 offspring) were completed. The results indicate that *in utero* exposure to ammonium sulfate aerosols during gestation altered the developmental trajectory of offspring, with perturbation that were still evident on postnatal day 105. At birth, differences in the gestation length, birth weight, and in the development of several major vital organs, including the brain, liver, kidney, and spleen, were discernible. Furthermore, the female offspring were more adversely affected by the high aerosol loading with further discernible differences in the stomach and in the distribution of body fat.

CHAPTER V

CAN WE UTILIZE GAS PHASE CHEMISTRY MODELS TO FURTHER OUR UNDERSTANDING OF ATMOSPHERIC AEROSOLS? ELUCIDATION OF THE GAS PHASE CHEMISTRY IN BEIJING, CHINA

i) Introduction

It has become evident that the mechanism of haze formation in Beijing is unique from other regions of the world; however, the gas phase chemistry in China, particularly the chemistry that leads to aerosol formation, has yet to be completely reproduced in chemical models. Several previous modeling endeavors in Beijing have concluded that the sources leading to aerosol formation must be underestimated or missing because models have frequently failed to reproduce the temporal trend and concentration of some gas phase species [Fu *et al.*, 2009; Lu *et al.*, 2013]. As we have shown, gaseous emissions are largely responsible for the elevated aerosol nucleation potential and the efficient and prolonged secondary aerosol formation that leads to the PM_{2.5} haze events. Laboratory studies have revealed that SOA formation is highly dependent on a wide range of experimental conditions, including NO_x concentration, particle acidity, the concentration of pre-existing aerosols, and oxidation rate [Kroll and Seinfeld, 2008]. Several laboratory and field studies have also shown that organic peroxy radicals (RO₂) and O₃ can govern the formation of aerosols [Finlayson-Pitts and Pitts, 2000; Zhang *et al.*, 2003; Li *et al.*, 2007; Kroll and Seinfeld, 2008; Orlando and Tyndall, 2012]. RO₂, formed by the oxidation of VOCs, can control the oxidative capacity of the atmosphere and is a dominant removal pathway of several pollutants. However, of foremost

importance is the hydroxyl radical (OH). OH is a highly reactive, short-lived species that is often labeled the ‘detergent’ or ‘vacuum cleaner’ of the atmosphere because it is frequently the first step in the removal process of atmospheric pollutants [Levy, 1974; Forster *et al.*, 2007]. OH is so efficient at removing atmospheric species that the lifetime of most molecules can easily be estimated by solely using its reaction rate with OH. However measurements of OH can be difficult because concentrations can be extremely variable over short spatial and time scales and are dependent on the time of day, elevation, season, and geographical location.

Radical chemistry, particularly through oxidation reactions with OH, greatly influences the concentration and distribution of many atmospheric species, including VOCs, NO_x, and SO₂, which all undergo gas-to-particle conversion processes; therefore, in order to accurately model the SOA formation, the radical chemistry must first be well characterized. With the ultimate goal of elucidating the chemistry that leads to the production of aerosols, an analysis of the fundamental radical chemistry and gas phase species has been conducted for the period between 26 and 28 September 2013. This period was selected in order to compare the concentration and trends of the gas phase species during the time prior to, during, and after the rapid production of PM_{2.5}. The analyses were conducted by employing The National Center for Atmospheric Research’s (NCAR) Master Mechanism box model.

ii) The NCAR Master Mechanism Model

The Master Mechanism version 2.4 (originally developed by *Madronich and Calvert* [1989] and updated in March 2015) is an explicit and detailed gas phase chemical mechanism combined with a box model solver and a coupled online photolysis rate calculator. The model can simulate approximately 2000 species and 5000 gas phase reactions. If available, direct kinetic or mechanistic measurements are utilized, but for reactions that have yet to be directly measured, similar and analogy processes are used to derive both the product identity and rate constants [*Madronich and Calvert*, 1989]. The photolysis coefficients were calculated using the Tropospheric Ultraviolet Visible Model (TUV, version 5.0 updated November 2010) [*Madronich et al.*, 2011]. TUV is a robust one dimensional radiative transfer model program that calculates the spectral irradiance, the spectral actinic flux, photo-dissociation coefficients, and biologically effective irradiance in the 280 - 420 nm wavelength range in 1 nm intervals. The radiation is calculated using a 2-stream delta-Eddington code, and values are the sum of the direct sun and diffuse radiation [*Madronich et al.*, 2011]. The Master Mechanism has been previously used to model and compare hydrogen peroxide (H₂O₂), O₃, carbon monoxide (CO), SO₂, NO, NO₂, benzene, toluene, ethylbenzene and xylene with observations from various field studies [*Acker et al.*, 2008; *Apel et al.*, 2010; *Pehnec et al.*, 2010; *Liang et al.*, 2013].

An atmospheric box model provides insight into the temporal behavior of atmospheric species in idealized and controlled conditions. Four main processes control the concentrations of chemical species at a given location: emissions, chemical reactions,

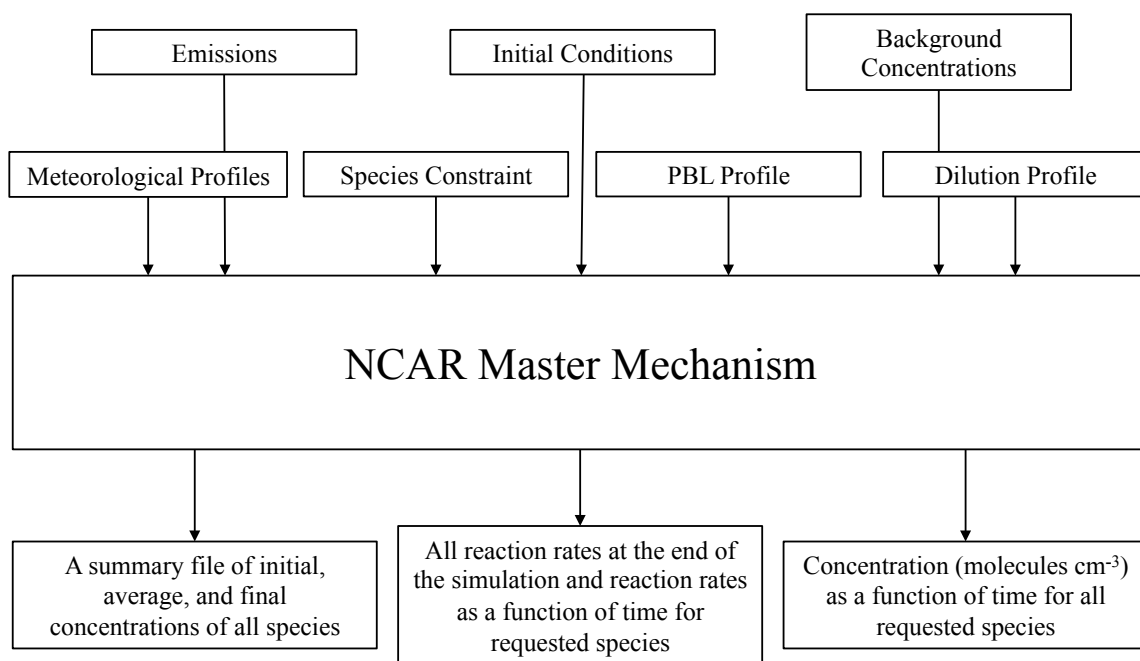


Figure 36. An overview of the NCAR Master Mechanism box model.

meteorological processes, and deposition (either by dry deposition or scavenging by atmospheric hydrometeors). Chemical species are emitted to the atmosphere by a variety of natural (the biosphere, volcanoes, soil, bacteria, etc.) and anthropogenic (vehicle exhaust, biomass burning, industrial processes, etc.) sources. Even though the sources tend to be similar in all urban environments, the emission profiles can differ dramatically between urban centers due to the differences in the vehicle fleet, industrial processes, and governmental regulations [Liu *et al.*, 2007; Levy *et al.*, 2013; Guo *et al.*, 2014; Levy *et al.*, 2014a; Zhang *et al.*, 2015b]. The Master Mechanism allows the user to modify the emission concentrations and diurnal profiles, set the temperature, pressure, dilution, cloud fraction, and boundary layer height as a function of time, incorporate deposition,

establish background and initial concentrations, and constrain any species of interest with respect to time (Figure 36).

iii) Adaptation of the Model to Beijing, China

a) Emission and Meteorological Profiles

In Figure 37A-E the input profiles of the meteorological parameters are displayed. The temperature profile was adapted from the in situ measurements at the meteorological station at PKU. The H₂O profile was incorporated to reproduce the increasing relative humidity throughout the haze cycle, which may be an important component due to the enhancement of multiphase chemistry and aerosol formation at high relative humidity [Jia and Xu, 2014; Zhang et al., 2015a]. Vertical and horizontal transports are somewhat crudely accounted for by variations in the PBL height that allows for time-varying exchange of PBL gases with those in the residual layer above, and horizontal ventilation, respectively. The ventilation rate is derived from the wind speed and size of the modeled location. The wind was also obtained from measurements at the PKU meteorological station, and Beijing was considered to be 50 km wide, i.e. the approximate distance between the east and west side of the 6th Ring Road. The height of the PBL is a critical parameter because it strongly influences the dispersion of air pollutants. A low PBL height can trap the pollutants in the surface layer, producing stagnant conditions that can lead to the accumulation of pollutants, whereas a high PBL will provide vertical ventilation and dilution of the mass concentration. The variation in the PBL height is driven by wind speed and the thermal elements (i.e. air temperature

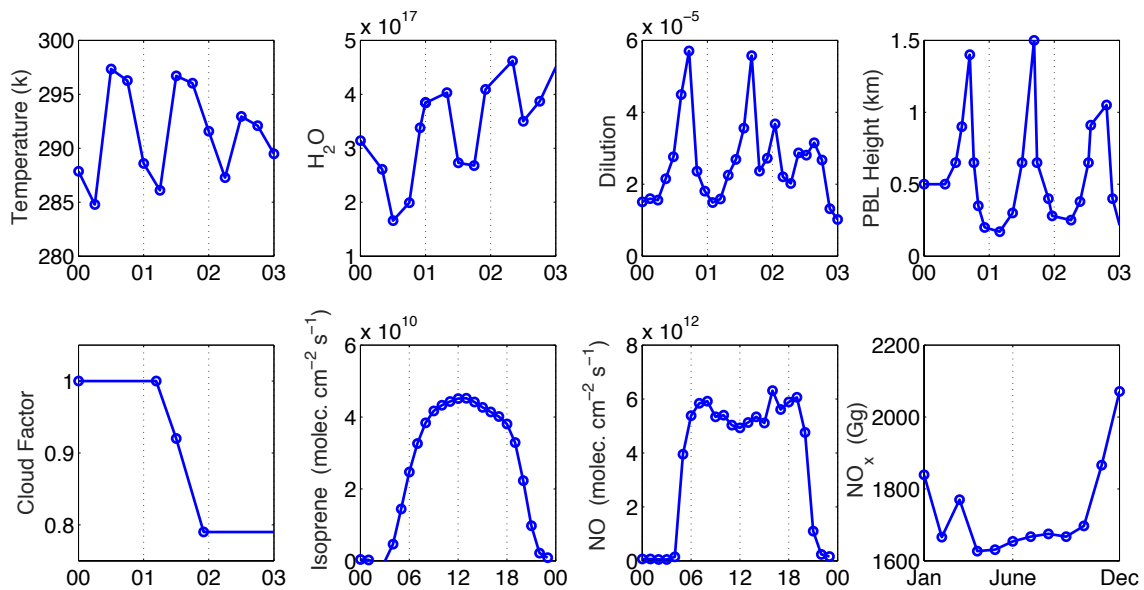


Figure 37. A-E) The temperature, H₂O (i.e. relative humidity), wind speed (used to estimate horizontal dilution), PBL height, and cloud factor profiles for the three days modeled. F-G). Concentration profiles of biogenic (i.e. isoprene) and anthropogenic (i.e. NO) sources. H) Seasonal emission profile for NO_x.

and solar intensity), which heat the surface and produce rising air and atmospheric instability. A low wind speed reduces entrainment and restricts the enhancement of the PBL. Previous studies in Beijing have demonstrated the variation of the PBL height as a function of the pollution cycle and time of day on the basis of satellite and LIDAR (light detection and ranging) observations [Liu *et al.*, 2013; Quan *et al.*, 2013]. The averaged PBL height was about 1 – 1.3 km during noon/afternoon-time, and 0.2 – 0.3 km during the nighttime. During the clean period, the PBL was higher during the afternoon hours (for example, 1.5 km on 23 September 2011), but as the pollution cycle progressed the PBL development became suppressed (0.75 km on 25 September 2011) [Liu *et al.*, 2013]. This PBL progression was also examined in a previous chapter (see Figures 28

and 31). The PBL suppression is due, in part, to a positive feedback cycle. The PBL development is dependent on the amount of solar radiation that reaches the surface, but as the aerosols mass begins to accumulate, the transmission of solar radiation decreases. As the PBL temperature decreases due to the declining solar radiation, the PBL height decreases, which further compresses and accumulates the aerosol mass. Measurements of the heat flux directly observed this process at the surface during heavy pollution [Quan *et al.*, 2013]. Furthermore, as the surface temperature cools, the relative humidity increases, which can enhance SOA formation [Zhang *et al.*, 2015a]. A strong external force such as high wind or a frontal system is needed to interrupt the further development of this extreme air pollution episode [Liu *et al.*, 2013; Quan *et al.*, 2013]. Using this information and PBL data from days with similar temperatures and mass concentrations, the profile shown in Figure 37D was constructed.

A cloud factor was incorporated in the model to mimic the weakened photochemical activity due to the dimming effect by the high aerosol loading during heavily polluted periods [Zheng *et al.*, 2014]. In the model, a cloud factor of zero indicates a night with no moon, and a value of unity indicates full sunlight. Ground based J_{NO_2} measurements obtained during the field campaign revealed that the photolysis rate decreased by 23 and 63% on the second and third day, respectively, compared to the clean day. Therefore, we assumed that photolysis was suppressed by 15 and 41% in the model (a 35% reduction from the ground based measurements) since the $\text{PM}_{2.5}$ mass concentration will be denser at the surface than in the middle of the PBL, i.e. the middle of the PBL experiences only about half of the reduction observed at the surface.

b) Emission Inventory

In Figure 37F-H an example of a daily biogenic, daily anthropogenic, and a seasonal anthropogenic emission profile is depicted. Biogenic emissions are closely associated with the solar cycle, with a peak near noon; whereas, anthropogenic emissions peak during the morning and evening rush hours due to increased traffic, but are generally elevated throughout the day. Establishing an appropriate emission inventory can be problematic since emissions are distinct for each urban center and it is not uncommon for specific sources to be underestimated which can create discrepancies when attempting to simulate the urban and regional chemistry [Liu *et al.*, 2007]. We employed a combination of the data from the Multi-resolution Emission Inventory for China (MEIC) and from preceding publications by Zhang *et al.* [2009], Zhou *et al.* [2010], and Wang *et al.* [2014c] to establish our base emission inventory. The black carbon, carbon monoxide, nitrogen oxides, organic carbon, PM₁₀, PM_{2.5}, and sulfur dioxide data (Table 4) were acquired through the MEIC website [MEIC, 2015]. Emission inventories are typically presented in Gg year⁻¹, so in order to convert to molec s⁻¹ cm⁻², Beijing was assumed to be 2360 km². The MEIC, developed by Tsinghua University, is a bottom-up air pollutant emission inventory with more than 700 emission sources and production categories. This inventory accounts for over 800 anthropogenic sources, which are aggregated to four sectors (power, industry, residential, and transportation). The speciated VOC data in Tables 4 and 5 were obtained from Wang *et al.* [2014c], in which online observations of VOCs in Beijing from July 2009 to January 2012 were presented. In order to appropriately model the chemistry during our selected

Species	MM Name	Emission Rate	
		Gg/yr	molec s ⁻¹ cm ⁻²
Black Carbon	BLKC	10.25	1.11E-11
Carbon Monoxide	CO	971.20	2.53E+13
Nitrogen Oxides	NOx	155.86	3.87E+12
Organic Carbon	ORGC	8.64	8.28E-12
PM ₁₀	PM10	72.53	9.11E-11
PM _{2.5}	PM25	51.26	6.25E-11
Sulfur Dioxide	SO2	160.96	1.89E+12
Ethane	C2H6	21.94	5.31E+11
Propane	C3H8	22.21	3.67E+11
i-Butane	c042	16.03	2.00E+11
n-Butane	c041	16.15	2.03E+11
i-Pentane	c053	15.89	1.61E+11
n-Pentane	c052	9.5	9.58E+10
2,3-Dimethylbutane	c062	41.43	3.50E+11
Ethylene	C2H4	23.86	6.19E+11
Propene	C3H6	10.39	1.79E+11
trans-2-Butene	u041	9.31	1.20E+11
1-Butene	u043	3.88	5.03E+10
Isoprene	uu51	2.24	2.40E+10
Benzene	C6H6	15	1.40E+11
Toluene	r071	27.93	2.21E+11
m,p-Xylene	r081	55.71	3.82E+11
Methanol	o011	58.3	1.32E+12
Formaldehyde	CH2O	14.52	3.52E+11
Acetaldehyde	d021	8.73	1.45E+11
Propanal	d031	0.96	1.20E+10
n-Butanal	d041	0.49	4.94E+09
n-Pentanal	d051	0.52	4.40E+09
n-Hexanal	d061	3.36	2.44E+10
Acetone	k031	19.07	2.40E+11
Methylethylketone	k041	5.97	6.03E+10
Acetylene	C2H2	15.06	4.21E+11

Table 4. Emission inventory used in the Master Mechanism. The black carbon, carbon monoxide, nitrogen oxides, organic carbon, PM₁₀, PM_{2.5}, and sulfur dioxide data were acquired through the MEIC website [MEIC, 2015], and the speciated VOC data were obtained from Wang *et al.* [2014c]. The second column indicates the naming system used by the Master Mechanism box model.

Species	MM Name	Gg/yr	Species	MM Name	Gg/yr
Alkanes			Alkenes Cont.		
ethane	C2H6	21.94	1,3-butadiene	uu51	1.67
propane	C3H8	22.21	1-pentene	u041	0.88
i-butane	c042	16.03	trans-2-pentene	u041	1.11
n-butane	c041	16.15	cis-2-pentene	u041	1.05
cyclopentane	c053	0.84	1-hexene	u041	1.14
i-pentane	c053	15.05	isoprene	uu51	0.57
n-pentane	c052	9.5	Aromatics		98.65
2,2-dimethylbutane	c062	0.37	benzene	C6H6	15
2,3-dimethylbutane	c062	1.58	toluene	r071	27.93
2-methylpentane	c062	6.23	ethylbenzene	r081	11.63
3-methylpentane	c062	4.95	m,p-xylene	r081	18.74
n-hexane	c062	6.78	o-xylene	r081	7.01
2,4-dimethylpentane	c062	0.38	styrene	r081	5.12
methylcyclopentane	c062	3.16	i-propylbenzene	r081	0.46
2-methylhexane	c062	1.81	n-propylbenzene	r081	0.77
cyclohexane	c062	1.52	m-ethyltoluene	r081	2.85
2,3-dimethylpentane	c062	1.01	p-ethyltoluene	r081	1.15
3-methylhexane	c062	2.64	1,3,5-trimethylbenzene	r081	1.31
2,2,4-trimethylpentane	c062	0.24	o-ethyltoluene	r081	1.1
n-heptane	c062	2.62	1,2,4-trimethylbenzene	r081	4.22
methylcyclohexane	c062	1.25	1,2,3-trimethylbenzene	r081	1.35
2,3,4-trimethylpentane	c062	0.11	OVOCs		111.92
2-methylheptane	c062	1	Methanol	o011	58.3
3-methylheptane	c062	0.73	Formaldehyde	CH2O	14.52
n-octane	c062	1.74	Acetaldehyde	d021	8.73
n-nonane	c062	1.97	Propanal	d031	0.96
n-decane	c062	1.34	n-Butanal	d041	0.49
Alkenes			n-Pentanal	d051	0.52
ethylene	C2H4	23.86	n-Hexanal	d061	3.36
Propene	C3H6	10.39	Acetone	k031	19.07
trans-2-butene	u041	2.81	Methylethylketone	k041	5.97
1-butene	u043	3.88	Others		15.06
cis-2-butene	u041	2.32	Acetylene	C2H2	15.06

Table 5. Detailed emission inventory of the non-methane hydrocarbons from Wang *et al.* [2014c]. The second column indicates the naming system used by the Master Mechanism. Similar compounds were aggregated (shown in red) to reduce the number of species.

period, the values were fitted to the seasonal (not shown) and diurnal profiles exhibited in Figure 37, which were obtained from *Zhang et al.* [2009] and *Zhou et al.* [2010], respectively. Since the box model does not have the capacity to simulate all known urban VOCs, some species were aggregated in the emission inventory as indicated by the red font.

The emission inventory is representative of the Beijing airshed, and therefore it does not characterize the emission at every location, but the region as a whole. In order to best reproduce the observations from the model period, a sensitivity study of the NO_x and VOC concentrations was conducted for ozone, NO_x, toluene, Ox, OH, and HO₂, as shown in Figure 38. The additional HONO chemistry discussed in the following section was included to generate these values. The model-generated peak values were determined as a function of NO_x and VOC emissions; where NO_x = 1 and VOCs = 1 are the suggested concentrations of 3.34×10^{17} and 5.38×10^{17} molecules day⁻¹ cm⁻², respectively, and NO_x = 0.5 and VOCs = 0.5 is half of the suggested values. The plus signs indicate where the model-generated peak values reasonably match the measured values (i.e. 92 ppb of NO_x, 5 ppb of toluene, 57 ppt of HO₂, 7.5×10^6 molecules cm⁻³ of OH, 31.7 ppb of Ox, and 100 ppb of Ozone). When we utilized the values as suggested, the simulated NO_x, VOC, and Ox concentrations were overestimated and OH and HO₂ concentrations were significantly underestimated. Therefore, we modified the emission inventory to attempt to reconcile these disparities. After several iterations, it was determined that the best combination was NO_x = 0.7 (i.e. 2.33×10^{17} molecules day⁻¹ cm⁻²) and VOC = 0.5 (i.e. 2.69×10^{17} molecules day⁻¹ cm⁻²), which indicates that the

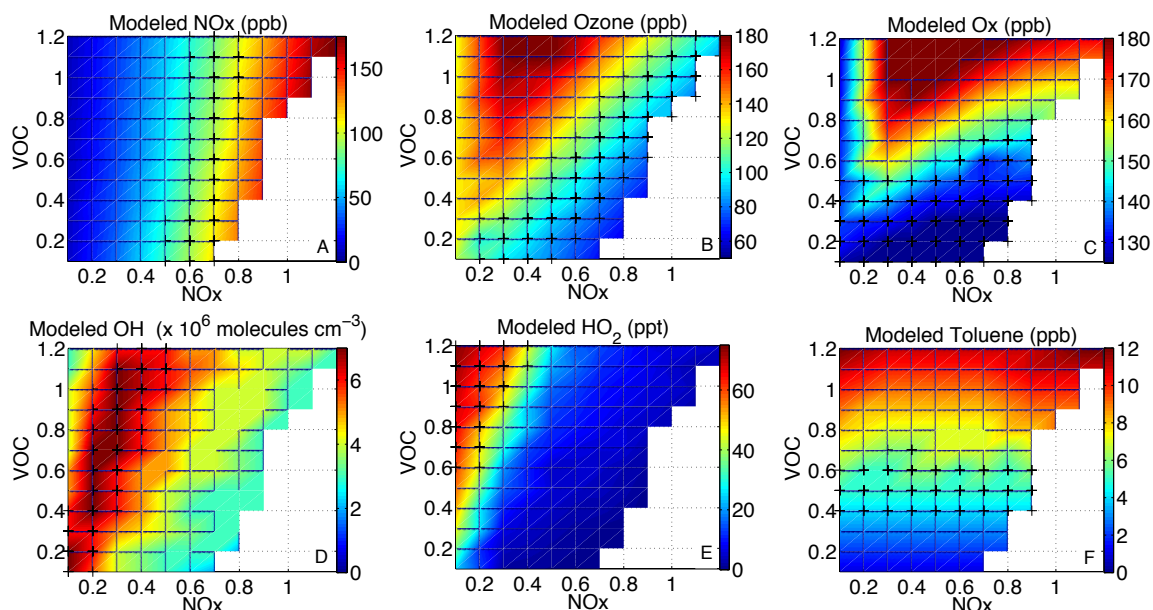


Figure 38. The model-generated peak values determined as a function of NO_x and VOC emissions for 27 September, where $\text{NO}_x = 1$ and $\text{VOCs} = 1$ is the concentrations suggested values by the *MEIC* [2015] (3.34×10^{17} molecules $\text{day}^{-1} \text{cm}^{-2}$) and *Wang et al.* [2014c] (5.38×10^{17} molecules $\text{day}^{-1} \text{cm}^{-2}$) emissions inventories, respectively, The plus signs indicate regions where the model-generated peak values reasonably matched the measured values.

emissions ratios of NO_x and VOCs are comparable at the PKU site to the Beijing airshed, but the overall concentration is lower. This may be due to the fact that the PKU site is located on the fourth ring in northwest Beijing, but still is chiefly influenced by local vehicle emissions.

c) *The Necessity of Nitrous Acid Chemistry in Beijing*

Initial model simulations revealed that the Master Mechanism was unable to satisfactorily reproduce the measurements, as many species that participate in radical chemistry were consistently underestimated (Figure 38). As the Master Mechanism has

been successfully used to simulate radical chemistry in other major urban centers such as Mexico City, Mexico; Zagreb, Croatia; and Shanghai, China [Acker *et al.*, 2008; Geng *et al.*, 2008; Apel *et al.*, 2010], there must exist a missing radical source or ancillary chemistry in Beijing that is not properly captured by the base reaction scheme. Recent studies have established that nitrous acid (HONO) may play a greater role in oxidation chemistry and ozone production than was previously thought, and potentially up to 30% of primary OH radical production can be attributed to the photolysis of HONO [Yang *et al.*, 2014]. The photolysis of HONO has been found to be a significant HO_x source in the early morning and midday, and increased overnight HONO concentrations have been shown to noticeably enhance the following daytime O₃ concentration [Finlayson-Pitts and Pitts, 2000; Ren *et al.*, 2010; 2013; Levy *et al.*, 2014b]. However, present knowledge of HONO sources remains incomplete, as the dominant gas-phase HONO source in traditional chemistry frequently fails to explain the high HONO concentrations observed in many cities [Liu *et al.*, 2014; Li *et al.*, 2015]. Furthermore, several measurements have revealed HONO trends that could not be attributed to traditional HONO chemistry. In Beijing, photolysis of HONO from an unknown heterogeneous source was found to be the predominant primary OH source at 2.2 ppb h⁻¹ [Liu *et al.*, 2012]. Measurements of ambient OH and HO₂ radicals by laser induced fluorescence during the Campaigns of Air Quality Research in Beijing and Surrounding Region (CAREBeijing 2006) field campaign also indicated a missing primary HO_x source (~ 3 ppb h⁻¹) during high NO_x conditions when a plume from Beijing was encountered [Lu *et al.*, 2013]. HONO measurements from CAREBeijing2006 determined that the average diurnal HONO

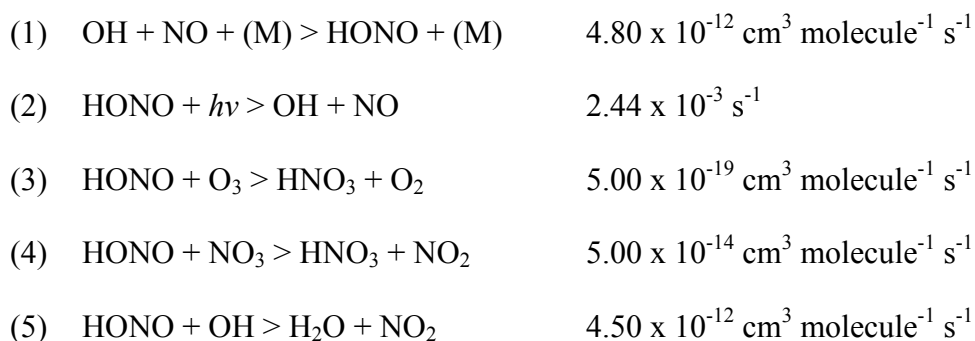
concentration varied from 0.33 to 1.2 ppb, and the net OH production rate from HONO was 7.1×10^6 molecule $\text{cm}^{-3} \text{s}^{-1}$, 2.7 times higher than from O_3 photolysis. Furthermore, an unknown HONO source, with an average rate of 7.3×10^6 molecule $\text{cm}^{-3} \text{s}^{-1}$ that peaked near noon, was identified, which produced four times more HONO than the reaction of NO with OH. An analysis of the correlations between the unknown source and other known HONO precursor mechanisms indicated that NO_2 was not likely the major precursor of the missing HONO source [Yang *et al.*, 2014]. Another set of HONO measurements were conducted in Beijing during the following year [Spataro *et al.*, 2013], which also identified an unknown daytime HONO signature that produced an average 2.58 ppb h^{-1} of HONO during the summer months. The daily average HONO concentrations were in the range of 0.03 – 2.91 ppb, and no temporal variation between the winter and summer seasons were observed. However, the trends in the HONO concentration were largely affected by meteorological conditions. Many proposed HONO formation pathways have been suggested to identify the mechanism of these unknown HONO concentrations, including the conversion of NO_2 through the heterogeneous reaction on wet surfaces in the absence of light, the photolysis of deposited HNO_3 , missing gas-phase chemistry reactions, direct emission by soils, and reactions occurring on aerosol surfaces [Ammann *et al.*, 1998; Finlayson-Pitts *et al.*, 2003; Kleffmann *et al.*, 2003; Zhou *et al.*, 2003; Stemmler *et al.*, 2006; Khalizov *et al.*, 2010; Su *et al.*, 2011; Oswald *et al.*, 2013; Liu *et al.*, 2014; Michoud *et al.*, 2014; Li *et al.*, 2015].

Until recently, NO_x was believed to be permanently removed from the atmosphere by HNO_3 formation and deposition; however, experimental and modeling results indicate that HNO_3 on ground surfaces can be photolyzed to HONO and NO_x . Furthermore, the HNO_3 photolysis rate constants on surfaces are 1 - 2 orders of magnitude higher than those in the gas and aqueous phases [Kleffmann *et al.*, 2003; Gao, 2011; Li *et al.*, 2015]. During the MEGAPOLI summer and winter field campaigns at SIRTA observatory in Paris, a major HONO source of unknown origin exhibited a bell-shaped diurnal profile with a maximum production around noon that produced up to 0.25 ppb h^{-1} , resulting in 1.7 ppb of unidentified HONO [Michoud *et al.*, 2014]. Concurrent measurements indicated that this missing source was likely photolytic and might be caused by heterogeneous surface reactions involving water content available on the ground.

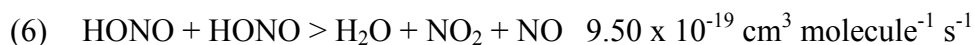
Given the high aerosol loading and abundance of NO_x , it is probable that heterogeneous reactions would be enhanced in this environment. Concurrent observations of HONO, NO_2 , and aerosols in Mexico City (Mexico), Houston (USA), and Xi'an (China) revealed that NO_2 heterogeneous reactions with semi-volatile organics from diesel vehicle emissions were essential for the nighttime accumulation of HONO (typically accounting for 75-90% of HONO formation); while NO_2 heterogeneous reaction on ground surfaces and with semi-volatile organics and the homogeneous reaction of NO reaction with OH chiefly contributed to the daytime HONO concentration [Li *et al.*, 2015]. In Kathmandu, high ratios of chemically formed secondary HONO to NO_2 were found, indicating unexpectedly efficient chemical

conversion of NO₂ to HONO. The authors proposed that this was due to high humidity, a strong and low inversion layer at night, and high aerosol loading, which is similar to meteorological conditions during haze events in Beijing [Yu *et al.*, 2009]. In Houston, observations have indicated that the heterogeneous conversion of HNO₃ on the surface of POAs is a significant HONO pathway, with an average of 0.97 ppb per event and a maximum increase of 2.2 ppb over 4 hours [Ziemba *et al.*, 2010]. Furthermore, on the basis of WRF–Chem modeling, heterogeneous reactions account for 59% of the simulated HONO concentrations in the Beijing, Tianjin, and Hebei Province [Li *et al.*, 2011]

Therefore, the HONO chemistry in the Master Mechanism was expanded to incorporate several of the proposed mechanisms to investigate the impact of HONO on radical chemistry in Beijing. The base HONO reactions set utilized in the Master Mechanism chemical scheme includes:



Five additional reaction proposed in the literature [Calvert *et al.*, 1994; Ziemba *et al.*, 2010; Yu *et al.*, 2009; Gao, 2011; Liu *et al.*, 2014; Michoud *et al.*, 2014; Li *et al.*, 2015] were then added to the added to the chemical scheme:



- (7) $\text{HO}_2 + \text{NO}_2 > \text{HONO} + \text{O}_2$ $8.00 \times 10^{-15} \text{ cm}^3 \text{ molecule}^{-1} \text{ s}^{-1}$
- (8) $\text{H}_2\text{O} + \text{NO} + \text{NO}_2 > \text{HONO} + \text{HONO}$ $6.30 \times 10^{-38} \text{ cm}^3 \text{ molecule}^{-1} \text{ s}^{-1}$
- (9) $\text{HNO}_3 + h\nu > \text{HONO} + \text{O}^3\text{P} + \text{HNO}_3$ $7.07 \times 10^{-5} \text{ s}^{-1}$
- (10) $\text{PM}_{2.5} + \text{NO}_2 > \text{HONO} + \text{PM}_{2.5}$ $3.00 \times 10^{-18} \text{ cm}^3 \text{ molecule}^{-1} \text{ s}^{-1}$

The photolysis rate constants shown are the peak daytime value, but will vary as function of sunlight. Reactions 6 - 8 are processes that have been observed to occur in the atmosphere in polluted urban environments [Calvert *et al.*, 1994]; whereas, Reactions 9 and 10 are essentially a proxy for reactions occurring on ground and aerosol surfaces, respectively. These are not gas phase reactions, but this model was designed to simulate gas phase species, so it cannot directly account for chemical reactions that occur on surfaces. In Reaction 9, HNO_3 is both created and destroyed because HONO is a byproduct of the photolysis of deposited HNO_3 . This HNO_3 has already been removed from the atmosphere so the reaction does not modify the existing HNO_3 concentration. However, HONO is added to the system as it is produced from the deposited HNO_3 . As the concentration of HNO_3 increases, both its deposition and the subsequent HONO concentration produced by this mechanism would be enhanced. Aerosols provide available surface areas for multi-phase reactions, and both laboratory and field measurements have demonstrated that as the aerosol mass load increases, the HONO concentration correspondingly increases [Ziemba *et al.*, 2008; Yu *et al.*, 2009; Liu *et al.*, 2014; Yang *et al.*, 2014]. The $\text{PM}_{2.5}$ mass concentration was manually constrained in the model to reproduce the field measurements during the measurement period (shown in a previous chapter); therefore, as the pollution cycle progresses, Reaction 10 would

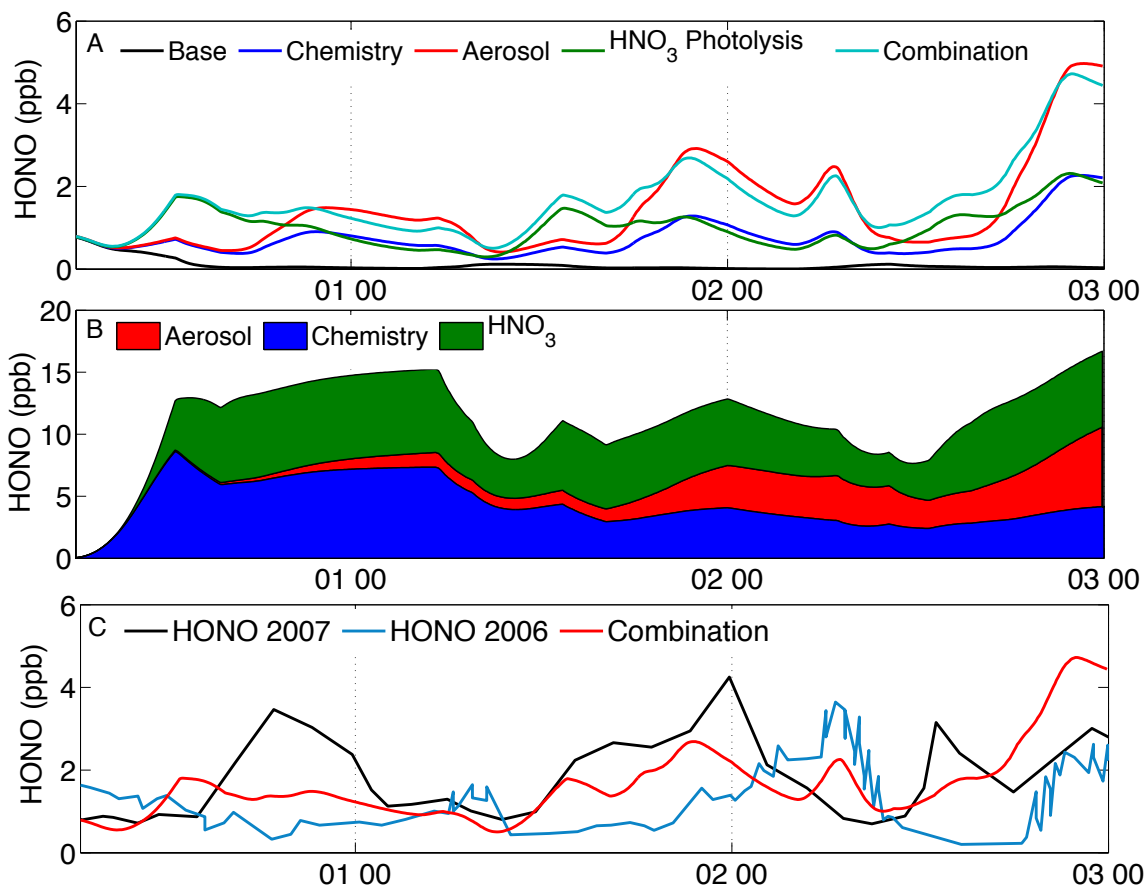


Figure 39. A) Source optimization of the various HONO sources in the MM Model. Days 0 - 2 correspond to 26 - 28 September 2013, respectively. The ‘base’ case utilized only the standard HONO chemistry provided in the model (1 - 5). The ‘chemistry’ case included only Reactions 1 - 8. The ‘aerosol’ run utilized the additional ‘chemistry’ reactions and HONO created by reactions on the surface of aerosols (1 - 8, 10). The ‘HNO₃ photolysis’ case included the additional ‘chemistry’ reactions and HONO produced through the photolysis of HNO₃ on surfaces (1 - 9). B) The total concentration produced through the three pathways. C) The simulation incorporating all reactions is compared to HONO measurements that were obtained in 2006 [Yang *et al.*, 2014] and 2007 [Spataro *et al.*, 2013] in the Beijing province.

become a more significant HONO source. The reaction rates for both (9) and (10) were created by reproducing the observed HONO concentration and temporal trends as shown in Figure 39. In Figure 39A, an analysis of the total concentration and temporal trends of the newly incorporated sources compared to the ‘base’ case, which only utilizes

Reactions 1 - 5, is shown. The ‘chemistry’ case includes the additional homogenous and heterogeneous chemical reactions (i.e. Reactions 1 - 8). The ‘aerosol’ case includes Reactions 1- 8 and HONO created by reactions on the surface of aerosols (i.e. Reaction 10). The ‘HNO₃ Photolysis’ case includes Reactions 1 - 8 and HONO produced through the photolysis of HNO₃ on surfaces (i.e. Reactions 9). All sources were incorporated for the ‘Combination’ case (i.e. Reactions 1 - 10). In Figure 39B, the total concentration produced through the three pathways is shown. These concentrations were determined by adding a tracer in the model so it only reflects the concentration of HONO produced through the various mechanisms and not the removal. This is why the peak concentration on day 1 is ~ 2 ppb in Figure 38A compared to ~ 15 ppb in Figure 38B. The total concentration in Figure 38B was influenced by other model parameter (i.e., dilution due to wind and variations in the PBL height); hence, the apparent decrease in the concentration during the afternoon of day 1 and 2. In Figure 39C, the ‘Combined’ case, which was used in the modeling experiments, is not compared to HONO measurements that were obtained in 2006 [Yang *et al.*, 2014] and 2007 [Spataro *et al.*, 2013]. It is important to note that these measurements were conducted during different months (August and early September) within the Beijing province; therefore, these values are only exhibited to suggest an order of magnitude and the basic diurnal trends and cannot be directly compared. It is evident that the model did not capture the diurnal HONO trend with the base reaction set, but adding the first three additional reactions significantly improved the model simulation (i.e. a reasonable temporal trend). However, the ‘chemistry’ case failed to capture the lesser afternoon peaks and the overall

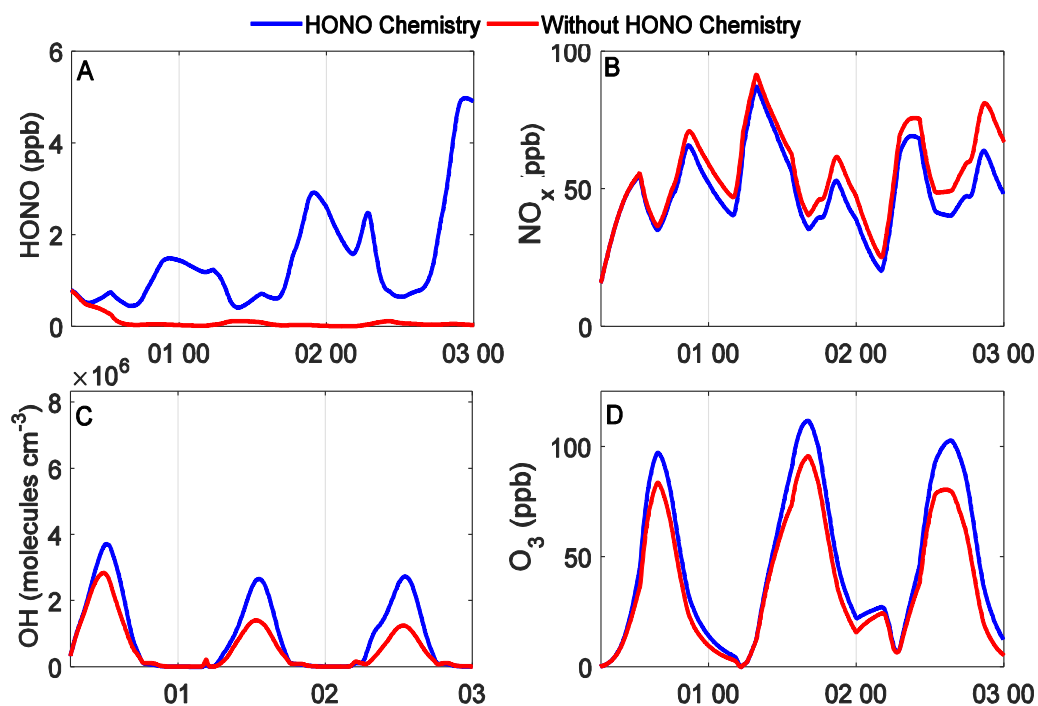


Figure 40. The temporal variations of various gas phase species when the expanded HONO chemistry is included (shown in blue) or excluded (shown in red) determined by the NCAR Master mechanism. Days 0-2 correspond to 26-28 September 2013, respectively.

concentration was too low, which was resolved by including the photolysis of HNO_3 . The HONO concentration did not increase as the pollution cycle progressed in the ‘Base’, ‘Chemistry’, or ‘ HNO_3 photolysis’ simulation, as has been observed. For example, during a moderately polluted period (day 1, $132 \mu\text{g m}^{-3}$) in 2006, the HONO concentration was 0.97 ppb at midnight, which increased to 2.75 ppb during the severely polluted period at midnight (day 2, $300 \mu\text{g m}^{-3}$). The pollution cycle was evident only after the heterogeneous conversion of NO_x to HONO on aerosol surfaces was included. The total production of HONO was similar between the clean and polluted periods, but the dominant mechanism changed as the pollution cycle progressed (Figure 38B).

A comparison of the concentration of HONO, NO_x, OH, and O₃ during the base case (Reactions 1 - 5) with the expanded HONO chemistry set (Reactions 1 - 10) is shown in Figure 40. The base and expanded NO_x were similar on day 0, but as the haze event began to intensify, a noticeable difference could be observed as NO_x was more efficiently converted into HONO. In the base case, the OH concentration decreased as the pollution cycle progressed; however, field studies have demonstrated that the OH concentration can remain fairly constant or slightly increase as the PM_{2.5} concentration increases [Lu *et al.*, 2013]. The OH concentration was enhanced in the expanded scheme by 27, 71, and 60% on days 0 – 2, respectively, which better represents measured OH values ($4 - 17 \times 10^6 \text{ cm}^{-3}$ in August 2006) [Lu *et al.*, 2013]. The peak ozone concentration was enhanced by 15, 18, and 29% on days 0-2, respectively, with the most noticeable enhancement occurring between 1 and 6 p.m.

iv) Results and Discussion

a) Sensitivity Study of the Relationship between NO_x and VOC

In order to understand the oxidation efficiency of the region, a sensitivity study of the NO_x and VOC ratio was conducted. In Figure 41, the model-generated ozone peak values determined as a function of NO_x and VOC emissions is exhibited. O₃ is photochemically formed through a complex set of nonlinear photochemical reactions involving free radicals (HO_x = OH + HO₂), VOCs, and NO_x. Depending on the ratio of these atmospheric, NO_x emissions can lead to the formation or destruction of ozone. The instantaneous ozone formation rate is dependent on the ratio of VOC to NO_x (VOC/

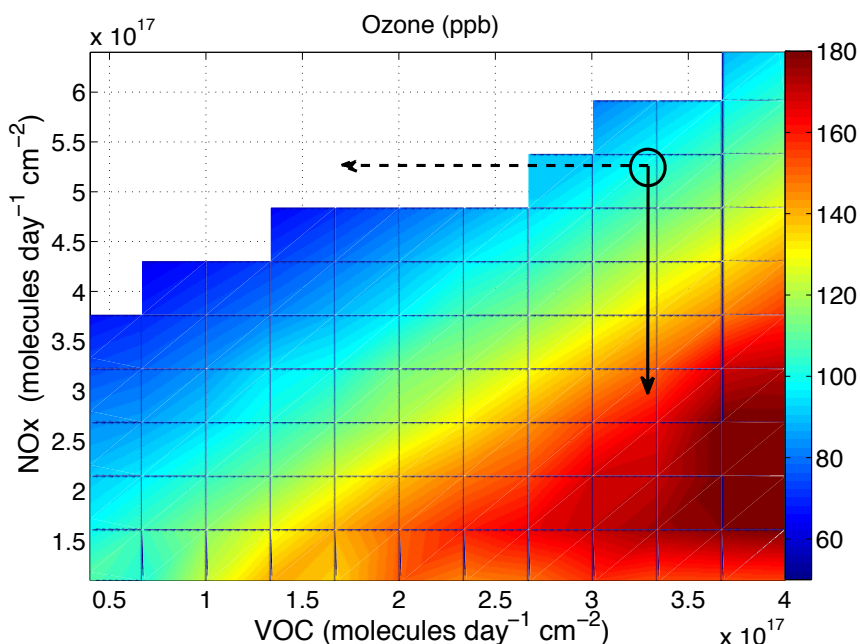


Figure 41. The model-generated peak values of ozone (ppb) determined as a function of NO_x and VOC emissions for 27 September. The circle indicates the base ratio of VOC and NO_x , and the dashed and solid lines indicate a 50% reduction of VOC and NO_x , respectively.

NO_x). At high VOC/ NO_x ratios, ozone formation is governed by the amount of NO_x available, known as a “ NO_x limited” or “VOC saturated” environment [Seinfeld and Pandis, 2012]. In this regime, the NO_x and ozone concentrations are positively related, while ozone is insensitive to variations in the VOC concentration. This occurs when the rate of ozone production is NO_x limited because the rate of OH production is greater than the rate of emission of NO_x . The reaction rate of OH with VOCs is faster than its reaction with NO. At low VOC/ NO_x ratios, known as “VOC limited” or “ NO_x saturated” environments, the O_3 concentration responds inversely to variations in the concentration of NO_x , but correspondingly with fluctuations in the VOC concentration. In this regime, the production of OH is less than the emission rate of NO_x , and ozone

	Emissions of NO _x	Emissions of VOCs	VOC/NO _x Ratio
This Study (Molecules day ⁻¹ cm ⁻²)	3.34 x 10 ¹⁷	5.38 x 10 ¹⁷	1.61
INTEX-B (Tonnes/year per 0.5 degree cell)	155.86	219.09	1.41
<i>Zhang et al.</i> [2009] (Gg/yr)	327.00	497.00	1.52
<i>Zhao et al.</i> , [2012] (x 10,000 T/yr)	30.90	34.60	1.12

Table 6. Comparison of the VOC/NO_x ratios

production is restricted by the availability of VOCs. Here, ozone is most effectively reduced by lowering the emissions of VOCs. Between the NO_x and VOC limited regimes, there exists a transitional region where ozone is nearly equally sensitive to each species and relatively insensitive to marginal changes in both NO_x and VOC in this situation environment [*Seinfeld and Pandis*, 2012]. Table 6, the emission rates of VOC and NO_x used in this study and from three other emission inventories are displayed. Even though the inventories span different geographical regions (i.e. Beijing proper versus the administrative borders of Beijing) and years, the inventories reveal that VOCs are emitted at a slightly elevated rate when compared to NO_x, with values of the VOC/NO_x ratio ranging between 1.1 and 1.7. Previous studies have generated conflicting conclusions on whether the region is NO_x or VOC limited [*Xu et al.*, 2008; *Wang et al.*, 2009; *Tang et al.*, 2010; *Liu et al.*, 2012; *Chen et al.*, 2013; *Wang et al.*, 2014d]. This discrepancy appears to be largely due to the spatial and temporal differences of ozone formation chemistry. Many studies have shown that that the

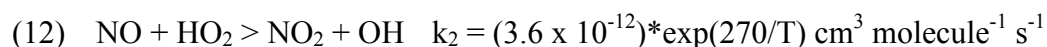
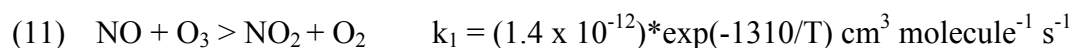
formation of O_3 is VOC limited in the urban areas of Beijing, while being more sensitive to NO_x levels in the suburban and downwind areas [Xu *et al.*, 2008; Wang *et al.*, 2009; Tang *et al.*, 2010; Wang *et al.*, 2014d]. However Liu *et al.* [2012] suggested that the region is neither NO_x nor VOC limited, but in a transition regime where the reduction of either NO_x or VOCs could result in reduced O_3 production. There were conflicted results for the specific region where our measurements were conducted: Wang *et al.* [2009] determined that the northern region of Beijing where PKU is located was NO_x limited; whereas, Shao *et al.* [2009] indicated that the PKU site was within the VOC limited regime. In addition, an ozone weekend effect, i.e. higher concentration of ozone on weekends, has been reported in the metropolitan area of Beijing–Tianjin–Hebei [Wang *et al.*, 2014d]. The authors suggested that this was due to a minor decrease in the VOC concentration and greater decrease in the NO_x concentrations on the weekends that lead to a higher VOC/ NO_x ratio. There was also found to be a vertical regime change with VOC-limited environment below 1 km and NO_x limited environment above [Chen *et al.*, 2013]. Our results indicate (Figure 38B) that the region is VOC limited, but the ozone formation responds more aggressively to perturbations of the NO_x concentration. For example, if the NO_x emission rate was held constant and the VOC emission rate was reduced by 50%, the peak ozone concentration would have been on the order of 70 ppb, a 29% reduction from the 98.7 ppb during the base case; whereas when the VOC emission rate was held constant and the NO_x emission rate was reduced by 50%, the peak ozone concentration increased to 165.0 ppb, a 67% enhancement from 98.7 ppb. If

both emission rates were reduced by 50%, the resultant ozone concentration was 111.3 ppb.

b) Model Results

The final model-generated values of the gas phase species determined by the NCAR Master Mechanism are shown alongside field measurements in Figure 42. O₃, O_x, CO, NO_x, and J_{NO₂} were measured during the model period (i.e. 26 - 28 September 2013) at the PKU site; whereas, the toluene and benzene concentrations were measured at the PKU site in October 2013. The OH [Lu *et al.*, 2013], HO₂ [Lu *et al.*, 2013], and HONO [Yang *et al.*, 2014] values were determined on the basis of measurements conducted in the Beijing region that were previously published; these values were used to recommend an order of magnitude. The peroxy radical (i.e. RO₂ + HO₂) values are compared to the peroxy radical concentration determined by the deviation from the photostationary state (PSS) [Cantrell *et al.*, 1997]:

$$\text{PSS} = \frac{k_{11}}{k_{12}} \left(\frac{J_{\text{NO}_2} [\text{NO}_2]}{k_{11} [\text{NO}]} - [\text{O}_3] \right)$$



Overall, the model was able to capture the temporal trends and concentrations of the species. The only exception was the peroxy radical concentration, which failed to reproduce both the magnitude and the timing of the peak. The previous measured HO₂ compare reasonably to the PSS calculation, providing validation for the observations.

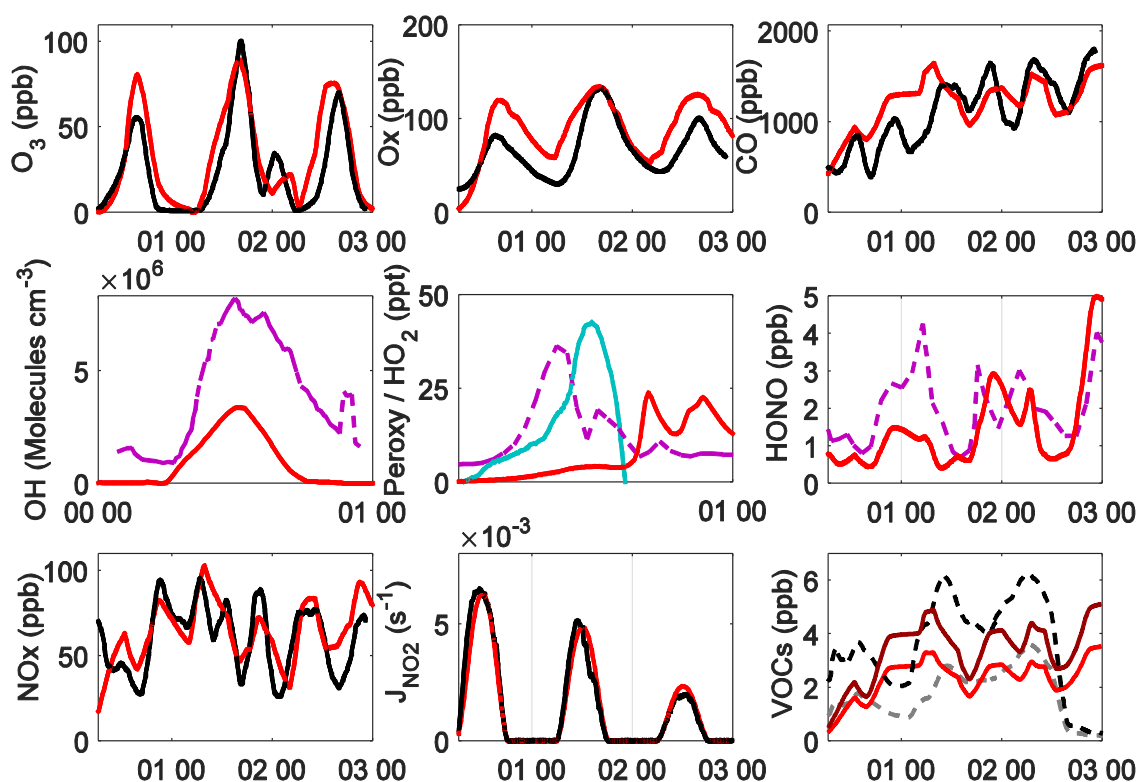


Figure 42. The temporal variations of various gas phase species (shown in red) determined by the NCAR Master mechanism compared to field measurements (black, purple, or aqua). A solid black line indicates that the measurements were collected at the PKU site. A purple line indicates that the values were reported from by previous publications [Lu *et al.*, 2013; Yang *et al.*, 2014]. A dashed line indicates that the measurements were not obtained during the model period. The aqua line is the peroxy radical concentration determined by the deviation from the photostationary state calculation. In the VOC panel, the darker lines indicate toluene and the lighter shades indicate benzene. Days 0 - 2 correspond to 26 - 28 September 2013, respectively.

The model was able to effectively capture the daily fluctuation in the CO, NOx, and O_3 concentration, and the cloud factor effectively reproduced the suppressed photolysis rate as the pollution cycle progressed. According to supplementary measurements, the model also predicted reasonable OH, HONO, and VOC concentrations. Measurements conducted between 18 August – 7 September 2006 observed daily concentration maxima

in the range of $4 - 17 \times 10^6 \text{ cm}^{-3}$ for OH [Lu *et al.*, 2013], therefore, even though the OH concentration appears to be underestimated, the predicted value is near the lower bounds of the observed OH concentrations in Beijing. Furthermore, there exist serious uncertainties in the measurements of OH [Mao *et al.*, 2012]. A comparison of the derived concentration of OH by laser-induced fluorescence in low-pressure detection chambers (called Fluorescence Assay with Gas Expansion (FAGE)) with a new chemical removal method revealed that the conventional FAGE method might be overestimating the OH concentration by 40 - 60%. This overestimation was hypothesized to be due to internally generated OH from the oxidation of biogenic VOCs. If the lower bound of the overestimation was used to correct the field measurements, then the daily concentration maxima would be in the range of $1.6 - 6.8 \times 10^6 \text{ cm}^{-3}$.

CHAPTER VI

CONCLUDING REMARKS AND FUTURE WORK

i) The Role of Volatile Organic Compounds in New Particle Formation

Our experiments revealed that the photooxidation of both biogenic and anthropogenic VOCs can produce homogenous nucleation; however, the formation rate is strongly dependent on the identity and initial concentration. The two biogenic VOCs utilized in the experiments exhibited the most efficient (α -pinene) and least efficient (isoprene) nucleation rate, underscoring the necessity of identification of VOCs, even in pristine environments, when trying to predict new particle formation in models.

Considering that the oxidation of α -pinene may proceed through several reaction channels leading to a variety of different chemical structures including monocarboxylic and dicarboxylic acids, each of the newly formed acidic species may contribute to hydrogen bonding to form stable critical clusters, which likely explains why α -pinene produces a higher concentration of particles. The selected anthropogenic VOCs (m-xylene and toluene) produce lower concentrations particles at atmospherically relevant concentrations compare to α -pinene. The mass spectrometry data suggests that the more efficient VOCs produced mainly low-volatility acidic products that can easily form stable critical clusters.

The dramatically different particle yields explain the observed distinct spatial patterns of NPF events globally. Isoprene-dominant regions, such as the Amazon Basin and the southeastern U.S., exhibit very few NPF events, whereas regions dominated by α -pinene, such as the boreal forests, may exhibit daily NPF events. This may also be

partially responsible for the lack of NPF events in locations dominated by anthropogenic VOCs such as Tijuana, Mexico. Increasing the initial VOC concentration resulted in a higher concentration of nucleated particles and a faster equilibrium time, which may explain why some cities exhibit much more efficient NPF events (i.e. a greater yield of particles) when compared to other regions that produce similar species and ratios of VOCs. Furthermore, it was found that mixing the VOC species altered the particle yield. The fluctuating combinations and concentrations of biogenic and anthropogenic VOCs in a complex urban environment may explain why NPF is only observed on select days within a given city.

It is clear from our chamber experiments that while α -pinene, m-xylene, and toluene produce NPF events, they did not contribute to particle growth. Future experiments should incorporate other atmospheric relevant gas phase species, such as SO_2 , NO_x , amines, or other VOCs, in order to determine the species that govern particle growth in the atmosphere.

ii) Beijing Haze Formation

We have decoupled the interplay between meteorology, local emissions, and aerosol processes that lead to severe haze events in Beijing by conducting comprehensive aerosol and gas phase measurements. The mechanism that produces haze formation in Beijing is comprised of two distinct processes of secondary aerosol formation, i.e., nucleation to initially produce high concentrations of nano-sized particles and the subsequent continuous growth from the nucleation mode particles. The results indicate

that the nucleation during the clean phase likely occurs on the regional scale (several hundred kilometers) and growth processes during the transition and polluted phases likely occur on the urban (about one hundred kilometers) scale. Our analysis of the aerosol chemical compositions suggests that organic aerosols are primarily responsible for producing the nucleation mode particles, while secondary organic aerosols and inorganic salts contribute jointly to the particle growth. New particle formation and growth occurs daily in many regions worldwide, but few other locations exhibit the sustained and efficient particle growth as was observed during the transition and polluted periods in Beijing. The combination of the high aerosol nucleation potential and efficient subsequent growth over several days uniquely differentiates the severe PM_{2.5} episodes in Beijing from those typically observed in other regions worldwide. We have shown that the periodic cycles of haze episodes during the fall and winter seasons in Beijing are closely linked to the large-scale meteorological conditions. During haze events, stagnation typically developed under calm or weak southerly wind from polluted industrial source regions, which trap local pollutants. Gaseous emissions of VOCs, NO_x, and SO₂ are jointly responsible for the large secondary formation of the PM_{2.5} events; while primary emissions and regional transport of PM_{2.5} are insignificant to the formation of severe haze events. Since the particle chemical composition in Beijing is comparable to many other large urban regions in the world, it must be the abundant condensable gases produced in the city that lead to the observed rapid and efficient particle formation and growth. Considering the relatively stagnant air mass during the pollution periods and the atmospheric lifetimes of aromatics (0.5-2.5 days), SO₂ (9.6

days), and NO_x, (1.0 days), the SO₂ level in Beijing likely includes a large regional contribution from the southern industrial areas, but the VOC and NO_x concentrations are dominated by local traffic emissions.

From the mediation perspective, it would be impractical to regulate new particle formation since it occurs on clean days and is naturally occurring, but it may be feasible to suppress the aerosol growth processes to reduce the PM_{2.5} levels in Beijing. Since primary particles contribute insignificantly to the severe haze events, an effort to solely control emissions of primary particles would result in only a minor reduction of the PM_{2.5} mass concentration. Our results imply that reductions in emissions of the aerosol precursor gases, i.e., VOCs and NO_x from local transportation and SO₂ from regional industrial sources, are critical for remediation of the haze pollution in Beijing. Observations from the 2008 Beijing Olympics and the 2014 APEC meeting provide validation for this conclusion. During the 2008 Beijing Olympics (8 – 24 August 2008), on-road vehicles were reduced by about 2 million, chemical plants in the city were closed, iron and steel mills reduced production, and construction was halted. The monthly average in August 2008 was 65.4 μg m⁻³, which is substantially lower than the monthly concentration observed during the next three years (107.3, 97.7, and 103.7 μg m⁻³, respectively) [*U.S. Department of State*, 2013]. Between 1 – 12 November 2014, numerous factories, such as steel mills, petroleum refineries, chemical manufactures, and power plants, stopped or reduced production and vehicles traffic was reduced by 50%. During this time period, the average PM_{2.5} mass concentration was 43 μg m⁻³, a 38% reduction from the projected ‘business as usual’ concentration of 69.5 μg m⁻³ [*Ministry*

of *Environmental Protection of China*, 2014]. The SO₂, NO_x, and VOC concentrations were reduced by 39.2, 49.6, and 33.6%, respectively.

iii) Development of an Animal Exposure System

We designed and built a chamber system that exposes pregnant rats to either pure or doped ambient air, with the focus of elucidating the transgenerational effects of maternal air pollutant exposure on *in utero* development and the physiological responses by the mothers. The custom-built compact whole-body stainless steel cage enables the uniform exposure of several animals simultaneously in individual compartments, while minimizing PM losses by deposition. In each experiment, pregnant Sprague-Dawley rats (4 control, 4 polluted per experiment) were continuously exposed to clean ($\sim 5 \mu\text{g m}^{-3}$) or doped ambient air ($\sim 150 \mu\text{g m}^{-3}$) for the first 18 days of gestation. In the base scenario, the animals were exposed to ammonium sulfate aerosols, which have a low toxicity, in order to assess the influence of aerosols processing by the animals. The results indicate that *in utero* development under maternal exposure to ammonium sulfate aerosols during gestation altered the developmental trajectory of the offspring, with perturbation that were still evident on postnatal day 105. At birth, differences in the gestation length, birth weight, and in the development of several major vital organs, including the brain, liver, kidney, and spleen, were discernible. Furthermore, the female offspring were more adversely affected by the high aerosol loading with further discernible differences in the stomach and in the distribution of body fat.

This work is intended to lay the foundation for future experiments involving more complex pollutant combinations. Several atmospheric compounds not yet explored by this project have previously been linked to health effects, including ozone, sulfuric acid, black carbon, NO_x, and organic aerosols. Unfortunately many of these studies have utilized a broad range of experimental methods, varying the method of exposure, concentrations, and exposure time; therefore, it is difficult to quantitatively compare the degradation of health between the various compounds. It would be beneficial to study these compounds in a systematic manner under the same experimental procedure. It is also imperative that we study the synergetic and additive nature of co-present pollutants since this is much more atmospherically realistic and is required to accurately evaluate health impacts of polluted air when elevated levels of several different gaseous and particle phase species are present simultaneously. A few studies have analyzed the co-presence of ozone with other pollutants and found that lung damage in rats due to inhaled ozone was exacerbated by the presence black carbon and sulfuric acid [*Jakab and Hemenway, 1994; Kimmel et al., 1997*]. It is likely that this synergism is true of other frequently co-present pollutants, but has not yet been identified or quantified.

iv) Gas Phase Chemistry Model of Beijing Radical Chemistry

The NCAR Master Mechanism Model was successfully utilized to model several radical species and photochemical oxidants in the Beijing atmosphere. Overall, the model was able to capture the temporal trends and concentrations of the species, with the exception of peroxy radicals. Sensitivity studies of the relationship between NO_x and

VOC indicate that the region is VOC limited. In order to simulate realistic concentrations, the base chemistry scheme was expanded to account for five new reactions; notably representations of HONO formed on aerosol and ground surfaces were incorporated. Despite the weakening of photochemical activity due to the dimming effect by the high aerosol loading during heavily the polluted period, OH and ozone did not exhibit reduced formation rates and the concentrations remained relatively stable. This may be due to the shifting of the dominant HONO formation mechanism as the pollution cycle progressed. Initially, HONO was chiefly formed by the non-particle phase reactions, but as the mass concentration increased, HONO formed on the surface of aerosols became a dominant source. It is likely that the combination of the persistent high concentrations of NO₂ in Beijing and the frequent periods of high aerosol loading leads to elevated HONO levels and sustained oxidizing capacity.

This work was completed with the ultimate goal of elucidating the chemistry that leads to the production of severe haze events in Beijing, China. Future work includes applying the knowledge gained from the simple box model experiments into the ‘Generator Of Explicit Chemistry and Kinetics of Organics in the Atmosphere’ (Gecko-A) model, which has been proven to effectively reproduce the SOA formation processes by resolving gas/particle partitioning in complex urban environments.

REFERENCES

- Acker, K., Kezele, N., Klasinc, L., Möller, D., Pehnec, G., Šorgo, G., ... & Žužul, S. (2008). Atmospheric H₂O₂ measurement and modeling campaign during summer 2004 in Zagreb, Croatia. *Atmospheric Environment*, 42(10), 2530-2542.
- Aerosol Robotic Network (AERONET). (2015). Beijing - AERONET Site Information Database. Retrieved September 16, 2015, from http://aeronet.gsfc.nasa.gov/new_web/photo_db/Beijing.html
- Aiken, A. C., Salcedo, D., Cubison, M. J., Huffman, J. A., DeCarlo, P. F., Ulbrich, I. M., ... & Jimenez, J. L. (2009). Mexico City aerosol analysis during MILAGRO using high resolution aerosol mass spectrometry at the urban supersite (T0)—Part 1: Fine particle composition and organic source apportionment. *Atmospheric Chemistry and Physics*, 9(17), 6633-6653.
- Albrecht, B. A. (1989). Aerosols, cloud microphysics, and fractional cloudiness. *Science*, 245(4923), 1227-1230. doi: 10.1126/science.245.4923.1227
- Ammann, M., Kalberer, M., Jost, D. T., Tobler, L., Rössler, E., Piguet, D., ... & Baltensperger, U. (1998). Heterogeneous production of nitrous acid on soot in polluted air masses. *Nature*, 395(6698), 157-160.
- Andreae, M. O. (2013). The aerosol nucleation puzzle. *science*, 339(6122), 911-912.
- Apel, E. C., Emmons, L. K., Karl, T., Flocke, F., Hills, A. J., Madronich, S., ... & Riemer, D. D. (2010). Chemical evolution of volatile organic compounds in the outflow of the Mexico City Metropolitan area. *Atmospheric Chemistry and Physics*, 10(5), 2353-2375.
- Araujo, J. A., Barajas, B., Kleinman, M., Wang, X., Bennett, B. J., Gong, K. W., ... & Nel, A. E. (2008). Ambient particulate pollutants in the ultrafine range promote early atherosclerosis and systemic oxidative stress. *Circulation research*, 102(5), 589-596.
- Aschmann, S. M., Reisseil, A., Atkinson, R., & Arey, J. (1998). Products of the gas phase reactions of the OH radical with α - and β -pinene in the presence of NO. *Journal of Geophysical Research: Atmospheres* (1984–2012), 103(D19), 25553-25561.

- Associated Press. (2013, October 22). Super smog hits north China city; flights canceled. Retrieved December 9, 2013.
- Ball, S. M., Hanson, D. R., Eisele, F. L., & McMurry, P. H. (1999). Laboratory studies of particle nucleation: Initial results for H₂SO₄, H₂O, and NH₃ vapors. *Journal of Geophysical Research: Atmospheres* (1984–2012), 104(D19), 23709-23718.
- Barker, D. J. (1995). Fetal origins of coronary heart disease. *BMJ: British Medical Journal*, 311(6998), 171.
- Bergmann, W. H. R. (1998). Predictions of particle deposition patterns in human and rat airways. *Inhalation toxicology*, 10(6), 557-583.
- Berndt, T., & Böge, O. (1997). Products and mechanism of the gas-phase reaction of NO₃ radicals with α -pinene. *Journal of the Chemical Society, Faraday Transactions*, 93(17), 3021-3027.
- Berndt, T., Stratmann, F., Sipilä, M., Vanhanen, J., Petäjä, T., Mikkilä, J., ... & Heintzenberg, J. (2010). Laboratory study on new particle formation from the reaction OH+ SO₂: influence of experimental conditions, H₂O vapour, NH₃ and the amine tert-butylamine on the overall process. *Atmospheric Chemistry and Physics*, 10(15), 7101-7116.
- Betha, R., Spracklen, D. V., & Balasubramanian, R. (2013). Observations of new aerosol particle formation in a tropical urban atmosphere. *Atmospheric Environment*, 71, 340-351.
- Boman, J., Lindén, J., Thorsson, S., Holmer, B., & Eliasson, I. (2009). A tentative study of urban and suburban fine particles (PM_{2.5}) collected in Ouagadougou, Burkina Faso. *X-Ray Spectrometry*, 38(4), 354-362.
- Bond, T. C. and R. W. Bergstrom (2006). Light absorption by carbonaceous particles: An investigative review. *Aerosol Science and Technology*, 40(1), 27-67. doi: 10.1080/02786820500421521
- Bond, T. C., Doherty, S. J., Fahey, D. W., Forster, P. M., Berntsen, T., DeAngelo, B. J., ... & Zender, C. S. (2013). Bounding the role of black carbon in the climate system: A scientific assessment. *Journal of Geophysical Research: Atmospheres*.

- Bonn, B., & Moorgat, G. K. (2002). New particle formation during a- and b-pinene oxidation by O₃, OH and NO₃, and the influence of water vapour: particle size distribution studies. *Atmospheric Chemistry and Physics*, 2(3), 183-196.
- Boy, M., Petäjä, T., Maso, M. D., Rannik, Ü., Rinne, J., Aalto, P., ... & Kulmala, M. (2004). Overview of the field measurement campaign in Hyytiälä, August 2001 in the framework of the EU project OSOA. *Atmospheric Chemistry and Physics*, 4(3), 657-678.
- Brodsky D. and P. G. Georgopoulos (2001). Growth and deposition of hygroscopic particulate matter in the human lungs. *Aerosol Science and Technology* 34: 144-159. doi: 10.1080/02786820118725
- Brown, J. S., Wilson, W. E., & Grant, L. D. (2005). Dosimetric comparisons of particle deposition and retention in rats and humans. *Inhalation toxicology*, 17(7-8), 355-385.
- Calvert, J. G., Yarwood, G., & Dunker, A. M. (1994). An evaluation of the mechanism of nitrous acid formation in the urban atmosphere. *Research on Chemical Intermediates*, 20(3-5), 463-502.
- Cantrell, C. A., Shetter, R. E., Calvert, J. G., Eisele, F. L., Williams, E., Baumann, K., ... & Mather, J. H. (1997). Peroxy radicals from photostationary state deviations and steady state calculations during the Tropospheric OH Photochemistry Experiment at Idaho Hill, Colorado, 1993. *Journal of Geophysical Research: Atmospheres* (1984–2012), 102(D5), 6369-6378.
- Chang, D., Song, Y., & Liu, B. (2009). Visibility trends in six megacities in China 1973–2007. *Atmospheric Research*, 94(2), 161-167.
- Chang, R. W., Slowik, J. G., Shantz, N. C., Vlasenko, A., Liggio, J., Sjostedt, S. J., ... & Abbatt, J. P. D. (2010). The hygroscopicity parameter (κ) of ambient organic aerosol at a field site subject to biogenic and anthropogenic influences: relationship to degree of aerosol oxidation. *Atmospheric Chemistry and Physics*, 10(11), 5047-5064.
- Chelani, A. B. (2013). Statistical Characteristics of Ambient PM_{2.5} Concentration at a Traffic Site in Delhi: Source Identification Using Persistence Analysis and Nonparametric Wind Regression. *Aerosol and Air Quality Research*, 13(6), 1768-1778.
- Chen, P., Quan, J., Zhang, Q., Tie, X., Gao, Y., Li, X., & Huang, M. (2013). Measurements of vertical and horizontal distributions of ozone over Beijing from 2007 to 2010. *Atmospheric Environment*, 74, 37-44.

- Chen, Y., Ebenstein, A., Greenstone, M., & Li, H. (2013). Evidence on the impact of sustained exposure to air pollution on life expectancy from China's Huai River policy. *Proceedings of the National Academy of Sciences*, 110(32), 12936-12941.
- Cheng, Y. F., Berghof, M., Garland, R. M., Wiedensohler, A., Wehner, B., Müller, T., ... & Zeng, L. M. (2009). Influence of soot mixing state on aerosol light absorption and single scattering albedo during air mass aging at a polluted regional site in northeastern China. *Journal of Geophysical Research: Atmospheres* (1984–2012), 114(D2).
- Cheung, J., Morawska, L., & Ristovski, Z. (2011). Observation of new particle formation in subtropical urban environment. *Atmospheric Chemistry and Physics (ACP) & Discussions (ACPD)*, 11, 3823-3833.
- Cohen, B. S., Xiong, J. Q., Fang, C. P., & Li, W. (1998). Deposition of charged particles on lung airways. *Health physics*, 74(5), 554.
- Committee on the Medical Effects of Air Pollutants (COMEAP) (2006). Cardiovascular disease and air pollution. Web PDF File retrieved September 2012.
<http://www.comeap.org.uk/images/stories/Documents/Reports/cvd%20report%202006.pdf>
- Dockery D. W., C. A. Pope, X. Xu, J. D. Spengler, J. H. Ware, M. E. Fay, B. G. Ferris, and F. E. Speizer. (1993). An association between air pollution and mortality in six U.S. cities. *N Engl J Med* 329:1753–1759. doi: 10.1056/NEJM199312093292401
- Dockery, D. W. and C. A. Pope (1994) Acute respiratory effects of particulate air-pollution, *Annu. Rev. Public Health*, 15, 107–132, 1994. doi: 0.1146/annurev.pu.15.050194.000543
- Dunn, M. J., Jiménez, J. L., Baumgardner, D., Castro, T., McMurry, P. H., & Smith, J. N. (2004). Measurements of Mexico City nanoparticle size distributions: Observations of new particle formation and growth. *Geophysical Research Letters*, 31(10).
- Earth System Research Laboratory, Global Monitoring Division. (2015). Surface Radiation Budget Network (SURFRAD) Aerosol Optical Depth. Retrieved September 16, 2015, from <http://www.esrl.noaa.gov/gmd/grad/surfrad/aod/comp2.html>

- Ehn, M., Petäjä, T., Birmili, W., Junninen, H., Aalto, P., & Kulmala, M. (2007). Non-volatile residuals of newly formed atmospheric particles in the boreal forest. *Atmospheric Chemistry and Physics*, 7(3), 677-684.
- Ewing, S. A., Christensen, J. N., Brown, S. T., Vancuren, R. A., Cliff, S. S., & Depaolo, D. J. (2010). Pb isotopes as an indicator of the Asian contribution to particulate air pollution in urban California. *Environmental science & technology*, 44(23), 8911-8916.
- Fan, J., R. Zhang, G. Li, and W. K. Tao (2007). Effects of aerosols and relative humidity on cumulus clouds. *Journal of Geophysical Research: Atmospheres (1984–2012)*, 112(D14). doi: 10.1029/2006JD008136
- Fan, J., R. Zhang, W. K. Tao, and K. I. Mohr (2008). Effects of aerosol optical properties on deep convective clouds and radiative forcing. *Journal of Geophysical Research: Atmospheres (1984–2012)*, 113(D8). doi: 10.1029/2007JD009257
- Finlayson-Pitts, B. J., & Pitts Jr, J. N. (2000). *Chemistry of the upper and lower atmosphere: theory, experiments, and applications*. Academic press.
- Finlayson-Pitts, B. J., Wingen, L. M., Sumner, A. L., Syomin, D., & Ramazan, K. A. (2003). The heterogeneous hydrolysis of NO₂ in laboratory systems and in outdoor and indoor atmospheres: An integrated mechanism. *Physical Chemistry Chemical Physics*, 5(2), 223-242.
- Forster, P., V. Ramaswamy, P. Artaxo, T. Berntsen, R. Betts, D. W. Fahey, J. Haywood, J. Lean, D. C. Lowe, G. Myhre, J. Nganga, R. Prinn, G. Raga, M. Schulz, and R. Van Dorland (2007), Changes in Atmospheric Constituents and in Radiative Forcing, in *Climate Change 2007: The Physical Science Basis. Contribution of Working Group I to the Fourth Assessment Report of the Intergovernmental Panel on Climate Change*, edited by S. Solomon, et al., *Cambridge University Press*, Cambridge, United Kingdom
- Forstner, H. J., Flagan, R. C., & Seinfeld, J. H. (1997). Secondary organic aerosol from the photooxidation of aromatic hydrocarbons: Molecular composition. *Environmental science & technology*, 31(5), 1345-1358.
- Fu, J. S., Streets, D. G., Jang, C. J., Kebin He, J. H., He, K., Wang, L., & Zhang, Q. (2009). Modeling regional/urban ozone and particulate matter in Beijing, China. *Journal of the Air & Waste Management Association*, 59(1), 37-44.

- Gao, H. (2011). Significance of HNO₃ Photolysis on Surfaces in Tropospheric Chemistry (Doctoral dissertation, STATE UNIVERSITY OF NEW YORK AT ALBANY).
- García, M. I., Rodríguez, S., González, Y., & García, R. D. (2014). Climatology of new particle formation at Izaña mountain GAW observatory in the subtropical North Atlantic. *Atmospheric Chemistry and Physics*, 14(8), 3865-3881.
- Gauderman, W. J., Avol, E., Gilliland, F., Vora, H., Thomas, D., Berhane, K., ... & Peters, J. (2004). The effect of air pollution on lung development from 10 to 18 years of age. *New England Journal of Medicine*, 351(11), 1057-1067.
- Geller, M., S. Biswas, and C. Sioutas (2006). Determination of particle effective density in urban environments with a differential mobility analyzer and aerosol particle mass analyzer. *Aerosol science and technology*, 40(9), 709-723. doi: 10.1080/02786820600803925
- Geng, F., Tie, X., Xu, J., Zhou, G., Peng, L., Gao, W., ... & Zhao, C. (2008). Characterizations of ozone, NO_x, and VOCs measured in Shanghai, China. *Atmospheric Environment*, 42(29), 6873-6883.
- Goldstein, A. H., & Galbally, I. E. (2007). Known and unexplored organic constituents in the earth's atmosphere. *Environmental Science & Technology*, 41(5), 1514-1521.
- Guillette Jr, L. J., & Iguchi, T. (2012). Life in a contaminated world. *Science*, 337(6102), 1614-1615.
- Guo, S., Hu, M., Guo, Q., Zhang, X., Schauer, J. J., & Zhang, R. (2013). Quantitative evaluation of emission controls on primary and secondary organic aerosol sources during Beijing 2008 Olympics. *Atmospheric Chemistry and Physics*, 13(16), 8303-8314.
- Guo, S., Hu, M., Guo, Q., Zhang, X., Zheng, M., Zheng, J., ... & Zhang, R. (2012). Primary sources and secondary formation of organic aerosols in Beijing, China. *Environmental science & technology*, 46(18), 9846-9853.
- Guo, S., Hu, M., Zamora, M. L., Peng, J., Shang, D., Zheng, J., ... & Zhang, R. (2014). Elucidating severe urban haze formation in China. *Proceedings of the National Academy of Sciences*, 111(49), 17373-17378.

- Guohui, L., Bei, N., Zhang, R., Cao, J., Wang, G., Ng, S., Tie, X., Wang, Y., Liu, S., Levy, M., & Molina, L. (submitted 2015). Elucidation of Atmospheric Formation Mechanism of Nitrous Acid (HONO) in Global Mega-Cities
- Hallar, A. G., Lowenthal, D. H., Chirokova, G., Borys, R. D., & Wiedinmyer, C. (2011). Persistent daily new particle formation at a mountain-top location. *Atmospheric Environment*, 45(24), 4111-4115.
- Hallquist, M., Wängberg, I., Ljungström, E., Barnes, I., & Becker, K. H. (1999). Aerosol and product yields from NO₃ radical-initiated oxidation of selected monoterpenes. *Environmental science & technology*, 33(4), 553-559.
- Hamilton, J. F., Webb, P. J., Lewis, A. C., & Reviejo, M. M. (2005). Quantifying small molecules in secondary organic aerosol formed during the photo-oxidation of toluene with hydroxyl radicals. *Atmospheric Environment*, 39(38), 7263-7275.
- Haywood, J. and O. Boucher (2000). Estimates of the direct and indirect radiative forcing due to tropospheric aerosols: A review. *Reviews of Geophysics*, 38(4), 513-543. doi: 10.1029/1999RG000078
- He, H., Wang, Y., Ma, Q., Ma, J., Chu, B., Ji, D., ... & Hao, J. (2014). Mineral dust and NO_x promote the conversion of SO₂ to sulfate in heavy pollution days. *Sci. Rep.* 4, 4172
- He, K. (2012, December). Multi-resolution Emission Inventory for China (MEIC): model framework and 1990-2010 anthropogenic emissions. In AGU Fall Meeting Abstracts (Vol. 1, p. 05).
- Hennigan, C. J., Sullivan, A. P., Fountoukis, C. I., Nenes, A., Hecobian, A., Vargas, O., ... & Weber, R. J. (2008). On the volatility and production mechanisms of newly formed nitrate and water soluble organic aerosol in Mexico City. *Atmospheric Chemistry and Physics*, 8(14), 3761-3768.
- Hildebrandt, L., Donahue, N. M., & Pandis, S. N. (2009). High formation of secondary organic aerosol from the photo-oxidation of toluene. *Atmospheric Chemistry and Physics*, 9(9), 2973-2986.
- Hoffmann, T., Bandur, R., Marggraf, U., & Linscheid, M. (1998). Molecular composition of organic aerosols formed in the α -pinene/O₃ reaction: Implications for

new particle formation processes. *Journal of Geophysical Research: Atmospheres* (1984–2012), 103(D19), 25569-25578.

Horvath, H. (1993). Atmospheric light absorption—A review. *Atmospheric Environment. Part A. General Topics*, 27(3), 293-317.

Huang, R. J., Zhang, Y., Bozzetti, C., Ho, K. F., Cao, J. J., Han, Y., ... & Prévôt, A. S. (2014). High secondary aerosol contribution to particulate pollution during haze events in China. *Nature*, 514(7521), 218-222.

Huang, X. F., He, L. Y., Hu, M., Canagaratna, M. R., Sun, Y., Zhang, Q., ... & Worsnop, D. R. (2010). Highly time-resolved chemical characterization of atmospheric submicron particles during 2008 Beijing Olympic Games using an Aerodyne High-Resolution Aerosol Mass Spectrometer. *Atmospheric Chemistry and Physics*, 10(18), 8933-8945.

Iinuma, Y., Böge, O., Gnauk, T., & Herrmann, H. (2004). Aerosol-chamber study of the α -pinene/O₃ reaction: influence of particle acidity on aerosol yields and products. *Atmospheric Environment*, 38(5), 761-773.

Intergovernmental Panel on Climate Change (IPCC). (2014). *Climate Change 2013: The physical science basis: Working group I contribution to the fifth assessment report of the Intergovernmental Panel on Climate Change*. Cambridge University Press, Cambridge, United Kingdom and New York, NY, USA., 1535 pp, doi:10.1017/CBO9781107415324.

INTEX-B Asia Emission Inventory Data Download Version 1.2. (2014). Modeling, inventory, and constraints on anthropogenic emissions. Retrieved March 22, 2015, from <http://mic.greenresource.cn/data/intex-b>

Jacobson, M. Z. (2000). A physically-based treatment of elemental carbon optics: Implications for global direct forcing of aerosols. *Geophysical Research Letters*, 27(2), 217-220. doi: 10.1029/1999GL010968

Jacobson, M. Z. (2001). Strong radiative heating due to the mixing state of black carbon in atmospheric aerosols. *Nature*, 409(6821), 695-697. doi: 10.1038/35055518

Jakab, G. J., & Hemenway, D. R. (1994). Concomitant exposure to carbon black particulates enhances ozone-induced lung inflammation and suppression of alveolar

macrophage phagocytosis. *Journal of Toxicology and Environmental Health, Part A Current Issues*, 41(2), 221-231.

Jia, L., & Xu, Y. (2014). Effects of relative humidity on ozone and secondary organic aerosol formation from the photooxidation of benzene and ethylbenzene. *Aerosol Science and Technology*, 48(1), 1-12.

Jimenez, J. L., Canagaratna, M. R., Donahue, N. M., Prevot, A. S. H., Zhang, Q., Kroll, J. H., ... & Shimono, A. (2009). Evolution of organic aerosols in the atmosphere. *Science*, 326(5959), 1525-1529.

Jobgen, W., Meininger, C. J., Jobgen, S. C., Li, P., Lee, M. J., Smith, S. B., ... & Wu, G. (2008). Dietary L-arginine supplementation reduces white fat gain and enhances skeletal muscle and brown fat masses in diet-induced obese rats. *The Journal of nutrition*, jn-108.

Jokinen, T., Berndt, T., Makkonen, R., Kerminen, V. M., Junninen, H., Paasonen, P., ... & Sipilä, M. (2015). Production of extremely low volatile organic compounds from biogenic emissions: Measured yields and atmospheric implications. *Proceedings of the National Academy of Sciences*, 201423977.

Jung, J., Miyazaki, Y., & Kawamura, K. (2013). Different characteristics of new particle formation between urban and deciduous forest sites in Northern Japan during the summers of 2010–2011. *Atmospheric Chemistry and Physics*, 13(1), 51-68.

Kanawade, V. P., Jobson, B. T., Guenther, A. B., Erupe, M. E., Pressley, S. N., Tripathi, S. N., & Lee, S. H. (2011). Isoprene suppression of new particle formation in a mixed deciduous forest. *Atmospheric Chemistry and Physics*, 11(12), 6013-6027.

Kavouras, I. G., Mihalopoulos, N., & Stephanou, E. G. (1998). Formation of atmospheric particles from organic acids produced by forests. *Nature*, 395(6703), 683-686.

Kavouras, I. G., Mihalopoulos, N., & Stephanou, E. G. (1999). Formation and gas/particle partitioning of monoterpenes photo-oxidation products over forests. *Geophysical Research Letters*, 26(1), 55-58.

Khalizov, A. F., Cruz-Quinones, M., & Zhang, R. (2010). Heterogeneous reaction of NO₂ on fresh and coated soot surfaces. *The Journal of Physical Chemistry A*, 114(28), 7516-7524.

- Khalizov, A. F., H. Xue, L. Wang, J. Zheng, and R. Zhang (2009a). Enhanced light absorption and scattering by carbon soot aerosol internally mixed with sulfuric acid. *The Journal of Physical Chemistry A*, 113(6), 1066-1074. doi: 10.1021/jp807531n
- Khalizov, A. F., R. Zhang, D. Zhang, H. Xue, J. Pagels, and P. H. McMurry (2009b). Formation of highly hygroscopic soot aerosols upon internal mixing with sulfuric acid vapor. *Journal of Geophysical Research: Atmospheres (1984–2012)*, 114(D5). doi: 10.1029/2008JD010595
- Khalizov, A. F., Y. Lin, C. Qiu, S. Guo, D. Collins, and R. Zhang (2013). The role of OH-initiated oxidation of isoprene in aging of combustion soot. *Environ. Sci. Technol.*, 2013, 47 (5), pp 2254–2263. doi: 10.1021/es3045339
- Kiendler-Scharr, A., Wildt, J., Dal Maso, M., Hohaus, T., Kleist, E., Mentel, T. F., ... & Wahner, A. (2009). New particle formation in forests inhibited by isoprene emissions. *Nature*, 461(7262), 381-384.
- Kim, T. O., Ishida, T., Adachi, M., Okuyama, K., & Seinfeld, J. H. (1998). Nanometer-sized particle formation from NH₃/SO₂/H₂O/air mixtures by ionizing irradiation. *Aerosol science and technology*, 29(2), 111-125.
- Kimmel, T. A., Chen, L. C., Bosland, M. C., & Nadziejko, C. (1997). Influence of acid aerosol droplet size on structural changes in the rat lung caused by acute exposure to sulfuric acid and ozone. *Toxicology and applied pharmacology*, 144(2), 348-355.
- Kirkby, J., Curtius, J., Almeida, J., Dunne, E., Duplissy, J., Ehrhart, S., ... & Stratmann, F. (2011). Role of sulphuric acid, ammonia and galactic cosmic rays in atmospheric aerosol nucleation. *Nature*, 476(7361), 429-433.
- Kleffmann, J., Kurtenbach, R., Lörzer, J., Wiesen, P., Kalthoff, N., Vogel, B., & Vogel, H. (2003). Measured and simulated vertical profiles of nitrous acid—Part I: Field measurements. *Atmospheric Environment*, 37(21), 2949-2955.
- Knox, A., G. J. Evans, J. R. Brook, X. Yao, C-H. Jeong, K. J. Godri, K. Sabaliauskas, and J. G. Slowik (2009). Mass absorption cross-section of ambient black carbon aerosol in relation to chemical age. *Aerosol Science and Technology*, 43(6), 522-532. doi: 10.1080/02786820902777207

- Korhonen, P., Kulmala, M., Laaksonen, A., Viisanen, Y., McGraw, R., & Seinfeld, J. H. (1999). Ternary nucleation of H₂SO₄, NH₃, and H₂O in the atmosphere. *Journal of Geophysical Research: Atmospheres* (1984–2012), 104(D21), 26349-26353.
- Kostenidou, E., R. K. Pathak, and S. Pandis (2007). An algorithm for the calculation of secondary organic aerosol density combining AMS and SMPS data. *Aerosol Science and Technology*, 41(11), 1002-1010. doi: 10.1080/02786820701666270
- Kothai, P., Saradhi, I. V., Pandit, G. G., Markwitz, A., & Puranik, V. D. (2011). Chemical characterization and source identification of particulate matter at an urban site of Navi Mumbai, India. *Aerosol and Air Quality Research*, 11(5), 560-569.
- Kreyling, W. G., Semmler, M., & Möller, W. (2004). Dosimetry and toxicology of ultrafine particles. *Journal of Aerosol Medicine*, 17(2), 140-152.
- Kroll, J. H., & Seinfeld, J. H. (2008). Chemistry of secondary organic aerosol: Formation and evolution of low-volatility organics in the atmosphere. *Atmospheric Environment*, 42(16), 3593-3624.
- Kulmala, M., Petäjä, T., Ehn, M., Thornton, J., Sipilä, M., Worsnop, D. R., & Kerminen, V. M. (2014). Chemistry of atmospheric nucleation: on the recent advances on precursor characterization and atmospheric cluster composition in connection with atmospheric new particle formation. *Annual review of physical chemistry*, 65, 21-37.
- Kulmala, M., Pirjola, L., & Mäkelä, J. M. (2000). Stable sulphate clusters as a source of new atmospheric particles. *Nature*, 404(6773), 66-69.
- Kulmala, M., Vehkamäki, H., Petäjä, T., Dal Maso, M., Lauri, A., Kerminen, V. M., ... & McMurry, P. H. (2004). Formation and growth rates of ultrafine atmospheric particles: a review of observations. *Journal of Aerosol Science*, 35(2), 143-176.
- Künzli, N., Jerrett, M., Mack, W. J., Beckerman, B., LaBree, L., Gilliland, F., ... & Hodis, H. N. (2005). Ambient air pollution and atherosclerosis in Los Angeles. *Environmental health perspectives*, 201-206.
- Kurtén, T., Loukonen, V., Vehkamäki, H., & Kulmala, M. (2008). Amines are likely to enhance neutral and ion-induced sulfuric acid-water nucleation in the atmosphere more effectively than ammonia. *Atmospheric Chemistry and Physics*, 8(14), 4095-4103.

- Lee, C. G., Yuan, C. S., Chang, J. C., & Yuan, C. (2005). Effects of aerosol species on atmospheric visibility in Kaohsiung city, Taiwan. *Journal of the Air & Waste Management Association*, 55(7), 1031-1041.
- Lelieveld, J., Evans, J. S., Fnais, M., Giannadaki, D., & Pozzer, A. (2015). The contribution of outdoor air pollution sources to premature mortality on a global scale. *Nature*, 525(7569), 367-371.
- Levin, Z. and W. R. Cotton (2009), *Aerosol Pollution Impact on Precipitation: A Scientific Review*, 386 pp., Springer, New York.
- Levy, H. (1974). Photochemistry of the troposphere. *Adv. Photochem.*, 9, 369-524.
- Levy, M. E., Zhang, R., Khalizov, A. F., Zheng, J., Collins, D. R., Glen, C. R., ... & Olaguer, E. (2013). Measurements of submicron aerosols in Houston, Texas during the 2009 SHARP field campaign. *Journal of Geophysical Research: Atmospheres*, 118(18), 10-518.
- Levy, M. E., Zhang, R., Zheng, J., Tan, H., Wang, Y., Molina, L. T., ... & Li, G. (2014a). Measurements of submicron aerosols at the California–Mexico border during the Cal–Mex 2010 field campaign. *Atmospheric Environment*, 88, 308-319.
- Levy, M., Zhang, R., Zheng, J., Zhang, A. L., Xu, W., Gomez-Hernandez, M., ... & Olaguer, E. (2014b). Measurements of nitrous acid (HONO) using ion drift-chemical ionization mass spectrometry during the 2009 SHARP field campaign. *Atmospheric Environment*, 94, 231-240.
- Li, G., Bei, N., Zhang, R., Cao, J., Wang, G., Ng, S., Tie, X., Wang, Y., Liu, S., Levy Zamora, M., & Molina, L. (submitted to Proceedings of the National Academy of Sciences 2014). Elucidation of Atmospheric Formation Mechanism of Nitrous Acid (HONO) in Global Mega-Cities
- Li, G., Zhang, R., Fan, J., & Tie, X. (2005). Impacts of black carbon aerosol on photolysis and ozone. *Journal of Geophysical Research: Atmospheres* (1984–2012), 110(D23).
- Li, G., Zhang, R., Fan, J., & Tie, X. (2007). Impacts of biogenic emissions on photochemical ozone production in Houston, Texas. *Journal of Geophysical Research: Atmospheres* (1984–2012), 112(D10).

- Li, Y., An, J., Min, M., Zhang, W., Wang, F., & Xie, P. (2011). Impacts of HONO sources on the air quality in Beijing, Tianjin and Hebei Province of China. *Atmospheric Environment*, 45(27), 4735-4744.
- Liang, H., Chen, Z. M., Huang, D., Zhao, Y., & Li, Z. Y. (2013). Impacts of aerosols on the chemistry of atmospheric trace gases: a case study of peroxides and HO₂ radicals. *Atmospheric Chemistry and Physics*, 13(22), 11259-11276.
- Lin, J., Pan, D., Davis, S. J., Zhang, Q., He, K., Wang, C., ... & Guan, D. (2014). China's international trade and air pollution in the United States. *Proceedings of the National Academy of Sciences*, 111(5), 1736-1741.
- Lin, Y. C., Hsu, S. C., Chou, C. C. K., Zhang, R., Wu, Y., Kao, S. J., ... & Huang, Y. T. (2015). Wintertime haze deterioration in Beijing by industrial pollution deduced from trace metal fingerprints and enhanced health risk by heavy metals. *Environmental Pollution*.
- Liu, H., He, K., Wang, Q., Huo, H., Lents, J., Davis, N., ... & He, C. (2007). Comparison of vehicle activity and emission inventory between Beijing and Shanghai. *Journal of the Air & Waste Management Association*, 57(10), 1172-1177.
- Liu, X. G., Li, J., Qu, Y., Han, T., Hou, L., Gu, J., ... & Hu, M. (2013). Formation and evolution mechanism of regional haze: a case study in the megacity Beijing, China. *Atmos. Chem. Phys*, 13(9), 4501-4514.
- Liu, Z., Wang, Y., Costabile, F., Amoroso, A., Zhao, C., Huey, L. G., ... & Zhu, T. (2014). Evidence of aerosols as a media for rapid daytime HONO production over China. *Environmental science & technology*, 48(24), 14386-14391.
- Liu, Z., Wang, Y., Gu, D., Zhao, C., Huey, L. G., Stickel, R., ... & Liu, S. C. (2012). Summertime photochemistry during CAREBeijing-2007: ROx budgets and O₃ formation. *Atmospheric Chemistry and Physics*, 12(16), 7737-7752.
- Lohmann, U. and J. Feichter (2005). Global indirect aerosol effects: a review. *Atmos. Chem. Phys*, 5(3), 715-737.
- Lu, K. D., Hofzumahaus, A., Holland, F., Bohn, B., Brauers, T., Fuchs, H., ... & Rohrer, F. (2013). Missing OH source in a suburban environment near Beijing: observed and modelled OH and HO₂ concentrations in summer 2006. *Atmospheric Chemistry and Physics*, 13(2), 1057-1080.

- Lung, Chiang, T. L., Lin, S. J., & Shu, B. C. (2013). Incinerator Pollution and Child Development in the Taiwan Birth Cohort Study. *International journal of environmental research and public health*, 10(6), 2241-2257.
- Madronich, S., & Calvert, J. G. (1989). The NCAR Master Mechanism of the gas phase chemistry: Version 2.0 (Vol. 333). Atmospheric Chemistry Division, National Center for Atmospheric Research.
- Madronich, S., Flocke, S., Zeng, J., Petropavlovskikh, I., & Lee-Taylor, J. (2011). Tropospheric ultraviolet-visible model (TUV).
- Majid, H., Madl, P., Hofmann, W., & Alam, K. (2012). Implementation of charged particles deposition in stochastic lung model and calculation of enhanced deposition. *Aerosol Science and Technology*, 46(5), 547-554.
- Mao, J., Ren, X., Zhang, L., Van Duin, D. M., Cohen, R. C., Park, J. H., ... & Brune, W. H. (2012). Insights into hydroxyl measurements and atmospheric oxidation in a California forest. *Atmospheric Chemistry and Physics*, 12(17), 8009-8020.
- Marti, J. J., Weber, R. J., McMurry, P. H., Eisele, F., Tanner, D., & Jefferson, A. (1997). New particle formation at a remote continental site: Assessing the contributions of SO₂ and organic precursors. *Journal of Geophysical Research: Atmospheres* (1984–2012), 102(D5), 6331-6339.
- Massoli, P., T. S. Bates, P. K. Quinn, D. A. Lack, T. Baynard, B. M Lerner, S. C. Tucker, J. Brioude, A. Stohl, E. J. Williams (2009). Aerosol optical and hygroscopic properties during TexAQS-GoMACCS 2006 and their impact on aerosol direct radiative forcing. *Journal of Geophysical Research: Atmospheres* (1984–2012), 114(D7). doi: 10.1029/2008JD011604
- Mauad, T., Rivero, D. H. R. F., de Oliveira, R. C., de Faria Coimbra Lichtenfels, A. J., Guimaraes, E. T., de Andre, P. A., ... & Saldiva, P. H. N. (2008). Chronic exposure to ambient levels of urban particles affects mouse lung development. *American journal of respiratory and critical care medicine*, 178(7), 721-728.
- Mauderly, J. L., & Samet, J. M. (2009). Is there evidence for synergy among air pollutants in causing health effects. *Environ Health Perspect*, 117(1), 1-6.
- McCormick, M. C. (1985). The contribution of low birth weight to infant mortality and childhood morbidity. *New England journal of medicine*, 312(2), 82-90.

- McCormick, M. C., Brooks-Gunn, J., Workman-Daniels, K., Turner, J., & Peckham, G. J. (1992). The Health and Developmental Status of Very Low—Birth-Weight Children at School Age. *Jama*, 267(16), 2204-2208.
- Meier, J., B. Wehner, A. Massling, W. Birmili, A. Nowak, T. Gnauk, E. Brüggemann, H. Herrmann, H. Min, and A. Wiedensohler (2009). Hygroscopic growth of urban aerosol particles in Beijing (China) during wintertime: a comparison of three experimental methods. *Atmos. Chem. Phys.*, 9(18), 6865-6880. doi: 10.5194/acp-9-6865-2009
- Merikanto J., Spracklen D. V., Mann G. W., Pickering S. J., Carslaw K. S. (2009). Impact of nucleation on global CCN, *Atmos. Chem. Phys.*, 9, 8601-8616
- Michoud, V., Colomb, A., Borbon, A., Miet, K., Beekmann, M., Camredon, M., ... & Doussin, J. F. (2014). Study of the unknown HONO daytime source at a European suburban site during the MEGAPOLI summer and winter field campaigns. *Atmospheric Chemistry and Physics*, 14(6), 2805-2822. Millman, A., D. Tang, and F. P. Perera (2008). Air pollution threatens the health of children in China. *Pediatrics*, 122(3), 620-628. doi: 10.1542/peds.2007-3143
- Moffet, R. C. and K. A. Prather (2009). In-situ measurements of the mixing state and optical properties of soot with implications for radiative forcing estimates. *Proceedings of the National Academy of Sciences*, 106(29), 11872-11877. doi: 10.1073/pnas.0900040106
- Moosmüller, H., R. K. Chakrabarty, and W. P. Arnott (2009). Aerosol light absorption and its measurement: A review. *Journal of Quantitative Spectroscopy and Radiative Transfer*, 110(11), 844-878. <http://dx.doi.org/10.1016/j.jqsrt.2009.02.035>
- Morgenstern, V., Zutavern, A., Cyrus, J., Brockow, I., Koletzko, S., Kramer, U., ... & Heinrich, J. (2008). Atopic diseases, allergic sensitization, and exposure to traffic-related air pollution in children. *American journal of respiratory and critical care medicine*, 177(12), 1331-1337.
- Morishita, M., Keeler, G. J., Wagner, J. G., Marsik, F. J., Timm, E. J., Dvonch, J. T., & Harkema, J. R. (2004). Pulmonary retention of particulate matter is associated with airway inflammation in allergic rats exposed to air pollution in urban Detroit. *Inhalation toxicology*, 16(10), 663-674.

- Multi-resolution Emission Inventory for China (MEIC). (1993). The MEIC model: National emission inventory. Retrieved April 10, 2015, from <http://www.meicmodel.org/>
- Norris, S. A., Osmond, C., Gigante, D., Kuzawa, C. W., Ramakrishnan, L., Lee, N. R., ... & Fall, C. H. (2012). Size at birth, weight gain in infancy and childhood, and adult diabetes risk in five low-or middle-income country birth cohorts. *Diabetes care*, 35(1), 72-79.
- O'Dowd, C. D., Aalto, P., Hmeri, K., Kulmala, M., & Hoffmann, T. (2002). Aerosol formation: Atmospheric particles from organic vapours. *Nature*, 416(6880), 497-498.
- Odum, J.R., Jungkamp, T.P.W., Griffin, R.J., Flagan, R.C. & Seinfeld, J.H. The atmospheric aerosol-forming potential of whole gasoline vapor. *Science* 276, 96-99 (1997).
- Odum, J. R., Hoffmann, T., Bowman, F., Collins, D., Flagan, R. C., & Seinfeld, J. H. (1996). Gas/particle partitioning and secondary organic aerosol yields. *Environmental Science & Technology*, 30(8), 2580-2585.
- Oldham, M. J., Phalen, R. F., Robinson, R. J., & Kleinman, M. T. (2004). Performance of a portable whole-body mouse exposure system. *Inhalation toxicology*, 16(9), 657-662.
- Organisation for Economic Co-operation and Development (OECD) (2015), OECD Urban Policy Reviews: China 2015, OECD Publishing, Paris.
DOI:<http://dx.doi.org/10.1787/9789264230040-en>
- Orlando, J. J., & Tyndall, G. S. (2012). Laboratory studies of organic peroxy radical chemistry: an overview with emphasis on recent issues of atmospheric significance. *Chemical Society Reviews*, 41(19), 6294-6317.
- Oswald, R., Behrendt, T., Ermel, M., Wu, D., Su, H., Cheng, Y., ... & Trebs, I. (2013). HONO emissions from soil bacteria as a major source of atmospheric reactive nitrogen. *science*, 341(6151), 1233-1235.
- Pagels, J., A. F. Khalizov, P. H. McMurry, and R. Y. Zhang (2009). Processing of soot by controlled sulphuric acid and water condensation—Mass and mobility relationship. *Aerosol Science and Technology*, 43(7), 629-640. doi: 10.1080/02786820902810685

- Peel, J. L., Haeuber, R., Garcia, V., Russell, A. G., & Neas, L. (2013). Impact of nitrogen and climate change interactions on ambient air pollution and human health. *Biogeochemistry*, 114(1-3), 121-134.
- Pehnc, G., Klasinc, L., Cvitaš, T., Vadić, V., & Šorgo, G. (2010). Modeling of ozone and hydrogen peroxide in air. *Croatica chemica acta*, 83(4), 433-438.
- Pereira, G., Cook, A. G., Haggard, F., Bower, C., & Nassar, N. (2012). Locally derived traffic-related air pollution and fetal growth restriction: a retrospective cohort study. *Occupational and environmental medicine*, oemed-2011.
- Pöhlker, C., Wiedemann, K. T., Sinha, B., Shiraiwa, M., Gunthe, S. S., Smith, M., ... & Andreae, M. O. (2012). Biogenic potassium salt particles as seeds for secondary organic aerosol in the Amazon. *Science*, 337(6098), 1075-1078.
- Qiu, C., A. F. Khalizov, and R. Zhang (2012). Soot aging from OH-initiated oxidation of toluene. *Environmental science and technology*, 46(17), 9464-9472. doi: 10.1021/es301883
- Quan, J., Gao, Y., Zhang, Q., Tie, X., Cao, J., Han, S., ... & Zhao, D. (2013). Evolution of planetary boundary layer under different weather conditions, and its impact on aerosol concentrations. *Particuology*, 11(1), 34-40.
- Ramana, M. V., V. Ramanathan, Y. Feng, S. C. Yoon, S. W. Kim, G. R. Carmichael, and J. J. Schauer (2010). Warming influenced by the ratio of black carbon to sulphate and the black-carbon source. *Nature Geoscience*, 3(8), 542-545. doi: 10.1038/ngeo918
- Ramanathan, V. and G. Carmichael (2008). Global and regional climate changes due to black carbon. *Nature geoscience*, 1(4), 221-227. doi: 10.1038/ngeo156
- Ramanathan, V., Li, F., Ramana, M. V., Praveen, P. S., Kim, D., Corrigan, C. E., ... & Yoon, S. C. (2007). Atmospheric brown clouds: Hemispherical and regional variations in long-range transport, absorption, and radiative forcing. *Journal of Geophysical Research: Atmospheres* (1984–2012), 112(D22).
- Ramanathan, V., P. J. Crutzen, J. T. Kiehl, and D. Rosenfeld (2001). Atmosphere, aerosols, climate, and the hydrological cycle, *Science*, 294(5549), 2119–2124, 2001. doi: 10.1126/science.1064034

- Ren, X., Duin, D., Cazorla, M., Chen, S., Mao, J., Zhang, L., ... & Kelley, P. (2013). Atmospheric oxidation chemistry and ozone production: Results from SHARP 2009 in Houston, Texas. *Journal of Geophysical Research: Atmospheres*, 118(11), 5770-5780.
- Ren, X., Gao, H., Zhou, X., Crouse, J. D., Wennberg, P. O., Browne, E. C., ... & Mao, J. (2010). Measurement of atmospheric nitrous acid at Bodgett Forest during BEARPEX2007. *Atmospheric Chemistry and Physics*, 10(13), 6283-6294.
- Reus, M., Ström, J., Kulmala, M., Pirjola, L., Lelieveld, J., Schiller, C., & Zöger, M. (1998). Airborne aerosol measurements in the tropopause region and the dependence of new particle formation on preexisting particle number concentration. *Journal of Geophysical Research: Atmospheres* (1984–2012), 103(D23), 31255-31263.
- Riccobono, F., Schobesberger, S., Scott, C. E., Dommen, J., Ortega, I. K., Rondo, L., ... & Curtius, J. (2014). Oxidation products of biogenic emissions contribute to nucleation of atmospheric particles. *Science*, 344(6185), 717-721.
- Rohde, R. A., & Muller, R. A. (2015). Air Pollution in China: Mapping of Concentrations and Sources. *PloS one*, 10(8), e0135749.
- Rosenfeld, D., Sherwood, S., Wood, R., and Donner, L. (2014). Climate effects of aerosol-cloud interactions. *Science*, 1247490(379), 343.
- Schlesinger, R. B. (1984). Comparative irritant potency of inhaled sulfate aerosols—effects on bronchial mucociliary clearance. *Environmental research*, 34(2), 268-279.
- Schlesinger, R. B., Kunzli, N., Hidy, G. M., Gotschi, T., & Jerrett, M. (2006). The health relevance of ambient particulate matter characteristics: coherence of toxicological and epidemiological inferences. *Inhalation toxicology*, 18(2), 95-125.
- Seifert, A., & Beheng, K. D. (2006). A two-moment cloud microphysics parameterization for mixed-phase clouds. Part 1: Model description. *Meteorology and atmospheric physics*, 92(1-2), 45-66.
- Seinfeld, J. H., & Pandis, S. N. (2012). *Atmospheric chemistry and physics: from air pollution to climate change*. John Wiley & Sons.
- Sellevåg, S. R., Georgievskii, Y., & Miller, J. A. (2009). Kinetics of the Gas-Phase Recombination Reaction of Hydroxyl Radicals to Form Hydrogen Peroxide†. *The Journal of Physical Chemistry A*, 113(16), 4457-4467.

- Shao, M., Lu, S., Liu, Y., Xie, X., Chang, C., Huang, S., & Chen, Z. (2009). Volatile organic compounds measured in summer in Beijing and their role in ground-level ozone formation. *Journal of Geophysical Research: Atmospheres* (1984–2012), 114(D2).
- Shen, X. J., Sun, J. Y., Zhang, Y. M., Wehner, B., Nowak, A., Tuch, T., ... & Wiedensohler, A. (2011). First long-term study of particle number size distributions and new particle formation events of regional aerosol in the North China Plain. *Atmospheric Chemistry and Physics*, 11(4), 1565-1580.
- Sipilä, M., Berndt, T., Petäjä, T., Brus, D., Vanhanen, J., Stratmann, F., ... & Kulmala, M. (2010). The role of sulfuric acid in atmospheric nucleation. *Science*, 327(5970), 1243-1246.
- Stanier, C. O., Khlystov, A. Y., & Pandis, S. N. (2004). Nucleation events during the Pittsburgh Air Quality Study: description and relation to key meteorological, gas phase, and aerosol parameters special issue of aerosol science and technology on findings from the fine particulate matter supersites program. *Aerosol Science and Technology*, 38(S1), 253-264.
- Stemmler, K., Ammann, M., Donders, C., Kleffmann, J., & George, C. (2006). Photosensitized reduction of nitrogen dioxide on humic acid as a source of nitrous acid. *Nature*, 440(7081), 195-198.
- Stern, J. E., Flagan, R. C., Grosjean, D., & Seinfeld, J. H. (1987). Aerosol formation and growth in atmospheric aromatic hydrocarbon photooxidation. *Environmental science & technology*, 21(12), 1224-1231.
- Su, H., Cheng, Y., Oswald, R., Behrendt, T., Trebs, I., Meixner, F. X., ... & Pöschl, U. (2011). Soil nitrite as a source of atmospheric HONO and OH radicals. *Science*, 333(6049), 1616-1618.
- Sun, Y. L., Zhang, Q., Schwab, J. J., Yang, T., Ng, N. L., & Demerjian, K. L. (2012). Factor analysis of combined organic and inorganic aerosol mass spectra from high resolution aerosol mass spectrometer measurements. *Atmospheric Chemistry and Physics*, 12(18), 8537-8551.
- Sun, Y., Jiang, Q., Wang, Z., Fu, P., Li, J., Yang, T., & Yin, Y. (2014). Investigation of the sources and evolution processes of severe haze pollution in Beijing in January 2013. *Journal of Geophysical Research: Atmospheres*, 119(7), 4380-4398.

- Swietlicki, E., H.-C. Hansson, K. Hämeri, B. Svenningsson, A. Massling, G. Mcfiggans, P. H. McMurry, T. Petäjä, P. Tunved, M. Gysel, D. Topping, E. Weingartner, U. Baltensperger, J. Rissler, A. Wiedensohler, and M. Kulmal (2008) Hygroscopic properties of submicrometer atmospheric aerosol particles measured with H-TDMA instruments in various environments—A review. *Tellus B*, 60(3), 432-469. doi: 10.1111/j.1600-0889.2008.00350.x
- Tang, X., Wang, Z., Zhu, J., Gbaguidi, A. E., Wu, Q., Li, J., & Zhu, T. (2010). Sensitivity of ozone to precursor emissions in urban Beijing with a Monte Carlo scheme. *Atmospheric Environment*, 44(31), 3833-3842.
- The Ministry of Environmental Protection of the People's Republic of China (MEP). (2013). The State Council Issues Action Plan on Prevention and Control of Air Pollution Introducing Ten Measures to Improve Air Quality. Retrieved December 15, 2014, from http://english.mep.gov.cn/News_service/infocus/201309/t20130924_260707.htm
- Toby, S., Van de Burgt, L. J., & Toby, F. S. (1985). Kinetics and chemiluminescence of ozone-aromatic reactions in the gas phase. *The Journal of Physical Chemistry*, 89(10), 1982-1986.
- Turpin, B. J. and H. J. Lim (2001). Species contributions to PM_{2.5} mass concentrations: Revisiting common assumptions for estimating organic mass. *Aerosol Science and Technology*, 35(1), 602-610. doi: 10.1080/02786820119445
- Twomey, S. (1977). *Atmospheric aerosols*. United States: Elsevier Scientific Publishing Co., New York, NY.
- U.S. Department of State. (2013). Mission China Beijing Air Quality Monitoring Program. Retrieved December 9, 2013, from <http://www.stateair.net/web/post/1/1.html>
- U.S. Environmental Protection Agency (EPA). (2012). National Ambient Air Quality Standards (NAAQS). Retrieved August 1, 2015, from <http://www.epa.gov/ttn/naaqs/>
- Uin, J., You, Y., Sierra-Hernández, M., Guenther, A. B., Brune, W. H., Misztal, P. K., ... & Lee, S. (2013, December). Absence of Biogenic New Particle Formation in the Southern US during the 2013 SOAS Field Campaign. In AGU Fall Meeting Abstracts (Vol. 1, p. 04).

- United Nations. (2014). World Urbanization Prospects: The 2014 Revision, Highlights. Department of Economic and Social Affairs. Population Division, United Nations.
- Veras, M. M., Damaceno-Rodrigues, N. R., Caldini, E. G., Ribeiro, A. A. M., Mayhew, T. M., Saldiva, P. H., & Dolhnikoff, M. (2008). Particulate urban air pollution affects the functional morphology of mouse placenta. *Biology of reproduction*, 79(3), 578-584.
- Veras, M. M., Damaceno-Rodrigues, N. R., Silva, R. M. G., Scoriza, J. N., Saldiva, P. H. N., Caldini, E. G., & Dolhnikoff, M. (2009). Chronic exposure to fine particulate matter emitted by traffic affects reproductive and fetal outcomes in mice. *Environmental research*, 109(5), 536-543.
- Wang, J., Da, L., Song, K., & Li, B. L. (2008). Temporal variations of surface water quality in urban, suburban and rural areas during rapid urbanization in Shanghai, China. *Environmental Pollution*, 152(2), 387-393.
- Wang, L., Khalizov, A. F., Zheng, J., Xu, W., Ma, Y., Lal, V., & Zhang, R. (2010). Atmospheric nanoparticles formed from heterogeneous reactions of organics. *Nature Geoscience*, 3(4), 238-242.
- Wang, M., Shao, M., Chen, W., Yuan, B., Lu, S., Zhang, Q., ... & Wang, Q. (2014c). A temporally and spatially resolved validation of emission inventories by measurements of ambient volatile organic compounds in Beijing, China. *Atmospheric Chemistry and Physics*, 14(12), 5871-5891.
- Wang, X., Li, J., Zhang, Y., Xie, S., & Tang, X. (2009). Ozone source attribution during a severe photochemical smog episode in Beijing, China. *Science in China Series B: Chemistry*, 52(8), 1270-1280.
- Wang, Y. H., Hu, B., Ji, D. S., Liu, Z. R., Tang, G. Q., Xin, J. Y., ... & Wang, Y. S. (2014d). Ozone weekend effects in the Beijing–Tianjin–Hebei metropolitan area, China. *Atmospheric Chemistry and Physics*, 14(5), 2419-2429.]
- Wang, Y., Wan, Q., Meng, W., Liao, F., Tan, H., & Zhang, R. (2011). Long-term impacts of aerosols on precipitation and lightning over the Pearl River Delta megacity area in China. *Atmospheric Chemistry and Physics*, 11(23), 12421-12436.
- Wang, Y., Wang, M., Zhang, R., Ghan, S. J., Lin, Y., Hu, J., ... & Molina, M. J. (2014a). Assessing the effects of anthropogenic aerosols on Pacific storm track using a

- multiscale global climate model. *Proceedings of the National Academy of Sciences*, 111(19), 6894-6899.
- Wang, Y., Zhang, R., & Saravanan, R. (2014b). Asian pollution climatically modulates mid-latitude cyclones following hierarchical modelling and observational analysis. *Nature communications*, 5.
- Wei, W., Cheng, S., Wang, L., Ji, D., Zhou, Y., Han, L., & Wang, L. (2015). Characterizing ozone pollution in a petrochemical industrial area in Beijing, China: a case study using a chemical reaction model. *Environmental monitoring and assessment*, 187(6), 1-10.
- Wildt, J., Mentel, T. F., Kiendler-Scharr, A., Hoffmann, T., Andres, S., Ehn, M., ... & Wahner, A. (2014). Suppression of new particle formation from monoterpene oxidation by NO_x. *Atmospheric chemistry and physics*, 14(6), 2789-2804.
- Wise, M. E., Surratt, J. D., Curtis, D. B., Shilling, J. E., & Tolbert, M. A. (2003). Hygroscopic growth of ammonium sulfate/dicarboxylic acids. *Journal of Geophysical Research: Atmospheres* (1984–2012), 108(D20).
- Woo, K. S., Chen, D. R., Pui, D. Y. H., & McMurry, P. H. (2001). Measurement of Atlanta aerosol size distributions: observations of ultrafine particle events. *Aerosol Science & Technology*, 34(1), 75-87.
- World Health Organization (2014). 7 million premature deaths annually linked to air pollution. Retrieved March 17, 2015, from <http://www.who.int/mediacentre/news/releases/2014/air-pollution/en/>
- Wu, R., Pan, S., Li, Y., & Wang, L. (2014). Atmospheric oxidation mechanism of toluene. *The Journal of Physical Chemistry A*, 118(25), 4533-4547.
- World Health Organization. Regional Office for Europe, & World Health Organization. (2006). Air quality guidelines: global update 2005: particulate matter, ozone, nitrogen dioxide, and sulfur dioxide. World Health Organization.
- Xu, J., Zhang, Y., Fu, J. S., Zheng, S., & Wang, W. (2008). Process analysis of typical summertime ozone episodes over the Beijing area. *Science of the Total Environment*, 399(1), 147-157.
- Xu, W. (2014). Nucleation and growth of atmospheric nanoparticles at molecular scale (Doctoral dissertation).

- Xue, H., A. F. Khalizov, L. Wang, J. Zheng, and R. Zhang (2009a). Effects of Coating of Dicarboxylic Acids on the Mass–Mobility Relationship of Soot Particles. *Enviro Sci. Technol*, 43 (8), 2787-2792. doi: 10.1021/es803287v
- Xue, H., A. F. Khalizov, L. Wang, J. Zheng, and R. Zhang (2009b). Effects of dicarboxylic acid coating on the optical properties of soot. *Physical Chemistry Chemical Physics*, 11(36), 7869-7875. doi: 10.1039/B904129J
- Yan, Y. H., Chou, C. C. K., Wang, J. S., Tung, C. L., Li, Y. R., Lo, K., & Cheng, T. J. (2014). Subchronic effects of inhaled ambient particulate matter on glucose homeostasis and target organ damage in a type 1 diabetic rat model. *Toxicology and applied pharmacology*, 281(2), 211-220.
- Yang, G., Wang, Y., Zeng, Y., Gao, G. F., Liang, X., Zhou, M., ... & Murray, C. J. (2013). Rapid health transition in China, 1990–2010: findings from the Global Burden of Disease Study 2010. *The lancet*, 381(9882), 1987-2015.
- Yang, Q., Su, H., Li, X., Cheng, Y., Lu, K., Cheng, P., ... & Zhang, Y. (2014). Daytime HONO formation in the suburban area of the megacity Beijing, China. *Science China Chemistry*, 57(7), 1032-1042.]
- Young, L. H., Lee, S. H., Kanawade, V. P., Hsiao, T. C., Lee, Y. L., Hwang, B. F., ... & Tsai, P. J. (2013). New particle growth and shrinkage observed in subtropical environments. *Atmospheric Chemistry and Physics*, 13(2), 547-564.
- Yu, C. P., & Xu, G. B. (1986). Predictive models for deposition of diesel exhaust particulates in human and rat lungs. *Aerosol science and technology*, 5(3), 337-347.
- Yu, F., & Turco, R. P. (2001). From molecular clusters to nanoparticles: Role of ambient ionization in tropospheric aerosol formation. *Journal of Geophysical Research: Atmospheres* (1984–2012), 106(D5), 4797-4814.
- Yu, H., McGraw, R., & Lee, S. H. (2012). Effects of amines on formation of sub-3 nm particles and their subsequent growth. *Geophysical Research Letters*, 39(2).
- Yu, J., & Jeffries, H. E. (1997). Atmospheric photooxidation of alkylbenzenes—II. Evidence of formation of epoxide intermediates. *Atmospheric Environment*, 31(15), 2281-2287.

- Yu, Y., Galle, B., Panday, A., Hodson, E., Prinn, R., & Wang, S. (2009). Observations of high rates of NO₂-HONO conversion in the nocturnal atmospheric boundary layer in Kathmandu, Nepal. *Atmospheric Chemistry and Physics*, 9(17), 6401-6415.
- Zhang, Q., Quan, J., Tie, X., Li, X., Liu, Q., Gao, Y., & Zhao, D. (2015a). Effects of meteorology and secondary particle formation on visibility during heavy haze events in Beijing, China. *Science of The Total Environment*, 502, 578-584.
- Zhang, Q., Streets, D. G., Carmichael, G. R., He, K. B., Huo, H., Kannari, A., ... & Yao, Z. L. (2009). Asian emissions in 2006 for the NASA INTEX-B mission. *Atmospheric Chemistry and Physics*, 9(14), 5131-5153.
- Zhang, R. (2010). Getting to the critical nucleus of aerosol formation. *Science*, 328(5984), 1366-1367.
- Zhang, R., A. F. Khalizov, L. Wang, M. Hu, and W. Xu (2012). Nucleation and growth of nanoparticles in the atmosphere. *Chemical Reviews-Columbus*, 112(3), 1957. doi: 10.1021/cr2001756
- Zhang, R., I. Suh, J. Zhao, D. Zhang, E. C. Fortner, X. Tie, L. T. Molina, and M. J. Molina (2004). Atmospheric new particle formation enhanced by organic acids. *Science*, 304(5676), 1487-1490. doi: 10.1126/science.1095139
- Zhang, R., Jing, J., Tao, J., Hsu, S. C., Wang, G., Cao, J., ... & Shen, Z. (2013). Chemical characterization and source apportionment of PM_{2.5} in Beijing: seasonal perspective. *Atmospheric Chemistry and Physics*, 13(14), 7053-7074.
- Zhang, R., Khalizov, A., Wang, L., Hu, M., & Xu, W. (2011). Nucleation and growth of nanoparticles in the atmosphere. *Chemical Reviews*, 112(3), 1957-2011.
- Zhang, R., L. Wang, A. F. Khalizov, J. Zhao, J. Zheng, R. L. McGraw, and L. T. Molina (2009). Formation of nanoparticles of blue haze enhanced by anthropogenic pollution. *Proceedings of the National Academy of Sciences*, 106(42), 17650-17654. doi: 10.1073/pnas.0910125106
- Zhang, R., Li, G., Fan, J., Wu, D. L., & Molina, M. J. (2007). Intensification of Pacific storm track linked to Asian pollution. *Proceedings of the National Academy of Sciences*, 104(13), 5295-5299.

- Zhang, R., Tie, X., & Bond, D. W. (2003). Impacts of anthropogenic and natural NO_x sources over the U.S. on tropospheric chemistry. *Proceedings of the National Academy of Sciences*, 100(4), 1505-1509.
- Zhang, R., Wang, G., Guo, S., Zamora, M. L., Ying, Q., Lin, Y., ... & Wang, Y. (2015b). Formation of Urban Fine Particulate Matter. *Chemical reviews*.
- Zhang, X. Y., Wang, Y. Q., Niu, T., Zhang, X. C., Gong, S. L., Zhang, Y. M., & Sun, J. Y. (2012). Atmospheric aerosol compositions in China: spatial/temporal variability, chemical signature, regional haze distribution and comparisons with global aerosols. *Atmospheric Chemistry and Physics*, 12(2), 779-799.
- Zhao, B., Wang, P., Ma, J. Z., Zhu, S., Pozzer, A., & Li, W. (2012). A high-resolution emission inventory of primary pollutants for the Huabei region, China. *Atmospheric Chemistry and Physics*, 12(1), 481-501.
- Zhao, J., A. F. Khalizov, R. Zhang, and R. McGraw (2009). Hydrogen-bonding interaction in molecular complexes and clusters of aerosol nucleation precursors. *The Journal of Physical Chemistry A*, 113(4), 680-689. doi: 10.1021/jp806693r
- Zhao, J., Levitt, N. P., & Zhang, R. (2005b). Heterogeneous chemistry of octanal and 2, 4-hexadienal with sulfuric acid. *Geophysical research letters*, 32(9).
- Zhao, J., Zhang, R., Misawa, K., & Shibuya, K. (2005a). Experimental product study of the OH-initiated oxidation of m-xylene. *Journal of Photochemistry and Photobiology A: Chemistry*, 176(1), 199-207.
- Zheng, G. J., Duan, F. K., Ma, Y. L., Cheng, Y., Zheng, B., Zhang, Q., ... & He, K. B. (2014). Exploring the severe winter haze in Beijing. *Atmos. Chem. Phys. Discuss*, 14(12), 17907-17942.
- Zhou, J., Swietlicki, E., Hansson, H. C., & Artaxo, P. (2002). Submicrometer aerosol particle size distribution and hygroscopic growth measured in the Amazon rain forest during the wet season. *Journal of Geophysical Research: Atmospheres* (1984–2012), 107(D20), LBA-22.
- Zhou, Y., Wu, Y., Yang, L., Fu, L., He, K., Wang, S., ... & Li, C. (2010). The impact of transportation control measures on emission reductions during the 2008 Olympic Games in Beijing, China. *Atmospheric Environment*, 44(3), 285-293.

Ziemba, L. D., Dibb, J. E., Griffin, R. J., Anderson, C. H., Whitlow, S. I., Lefer, B. L., ... & Flynn, J. (2010). Heterogeneous conversion of nitric acid to nitrous acid on the surface of primary organic aerosol in an urban atmosphere. *Atmospheric Environment*, 44(33), 4081-4089.